ANUL XLIX **2004**

S T U D I A

UNIVERSITATIS BABEŞ-BOLYAI

PHYSICA

1

EDITORIAL OFFICE: Republicii no. 24, 400015 Cluj-Napoca, Phone 0264-40.53.52

SUMAR - CONTENTS - SOMMAIRE - INHALT

STUDIA UNIVERSITATIS BABEŞ-BOLYAI, PHYSICA, XLIX, 1, 2004

PRODUCTION OF RADIOISOTOPES USING ISOTOPIC NEUTRON SOURCES

L. DARABAN, I. BOTIZ

Faculty of Physics, Babes-Bolyai University, 1. Kogalniceanu nr.1, 400084 Cluj-Napoca, Romania

ABSTRACT. We used isotopic neutron sources in order to produce the following radioisotopes: $^{124}Sb, ^{122}Sb, ^{152m}Eu, ^{187}W$. We also took their gamma spectra using a Ge(Li) detector, drawn their disintegration schemes in order to determine their half-lives, we identified the disintegration schemes and we also calculated the activity of some of these radioisotopes.

Introduction

Producing radioisotopes can be performed through different nuclear reactions which can take place in nuclear reactors or in accelerators.

The method of obtaining radioisotopes through a mechanism of irradiation with neutrons consists of bombarding some elements with different energy neutrons, the latter being obtained in different ways [1, 2, 3].

Generally, neutrons are used because, having a neutral electrical charge, they can generate nuclear reactions with most of the elements at relatively low energies. Therefore, in the technique of obtaining radioisotopes, the irradiation neutron systems are frequently used.

We used neutrons that we obtained from isotopic neutron sources of type (α, n). The neutron fascicules provided by these sources were obtained from nuclear reactions initiated by the constituent radioisotopes. The neutrons' spectrum has a continuous energetic distribution with two main peaks at the energies of 3.2 and 5.1 MeV. The reactions produced were of (n, γ) type.

Experimental

The irradiation block we used has two isotopic neutron sources an $^{241}Am-^{9}Be$ and a $^{239}Pu-^{9}Be$ source with the debit of $1.1\cdot 10^{7}\ neutrons/s$ (5 Ci ^{124}Am) and $5.5\cdot 10^{7}\ neutrons/s$ (25 Ci ^{239}Pu). These two sources are introduced in a close-ended tube which is placed inside another paraffin tube. The two sources can be lifted from the stocking boron position up to the irradiation position. The role of the paraffin block is to slow down the neutrons through multiple collisions with the hydrogen atoms. The so slowed neutrons end up in the lateral channels in which we had place our samples.

The gamma spectra of the obtained radioisotopes were acquired using a Ge(Li) detector coupled to a multichannel analyzer. In order to raise the disintegration curves we employed the NaI(Tl) scintillator crystal coupled to a monochannel analyzer as it has a better efficiency.

The calibration of our devices has been made using a ^{226}Ra source (a punctual source with 3.33 KBq activity) which made possible the exact determination of the radioisotopes' energies and, therefore, the identification of their disintegration schemes.

The form used for the calculus of the radioisotope's activity is:

$$\Lambda = \frac{A}{1800 \cdot \varepsilon \cdot P} \tag{1}$$

where Λ represents the activity in μ Ci, A is the area of the peaks, ε is the efficiency, P is the probability of transition at that energy as resulting from the disintegration scheme, whereas the factor 1800 comes from the acquisition time of the spectrum (30 minutes).

We successively irradiated different elements, obtaining radioisotopes whose gamma spectra are showed in Fig. 1, Fig. 2 and Fig. 3.

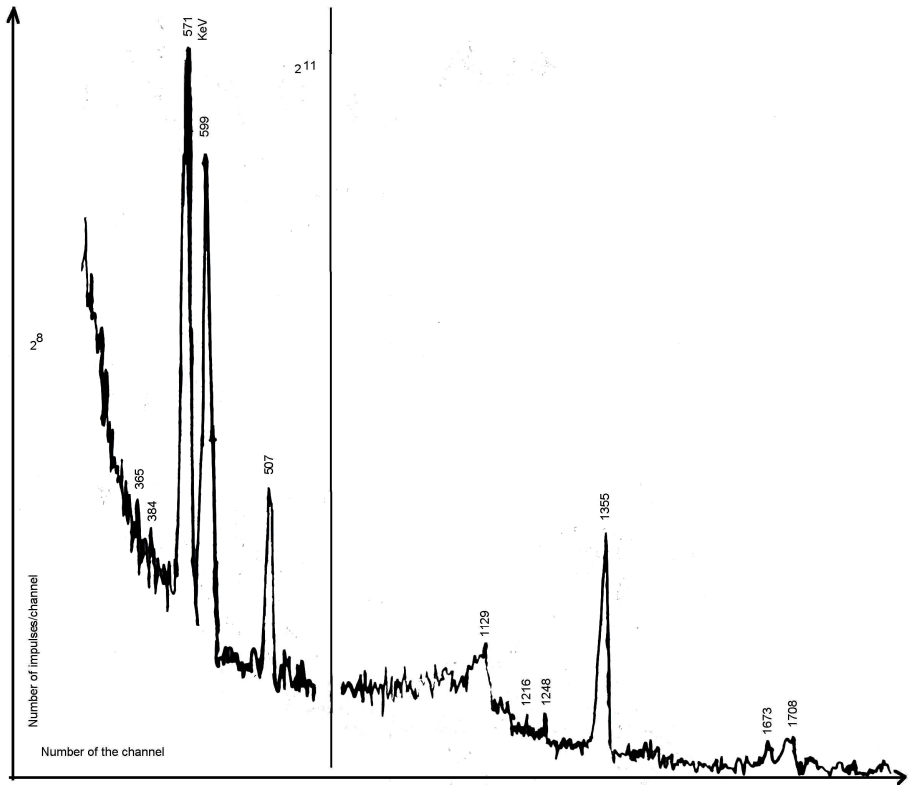

Fig. 1. Gamma spectrum of Sb obtained by irradiation with neutron isotopic sources

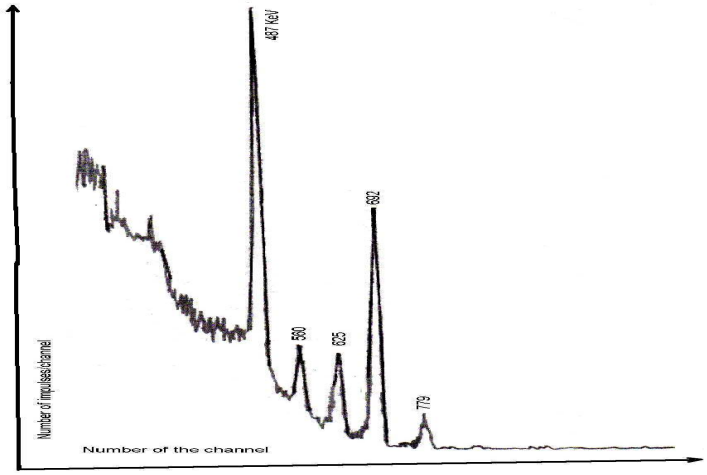

Fig. 2.Gamma spectrum for ^{187}W obtained by irradiation with neutron isotopic sources and the values of the energies for each peack.

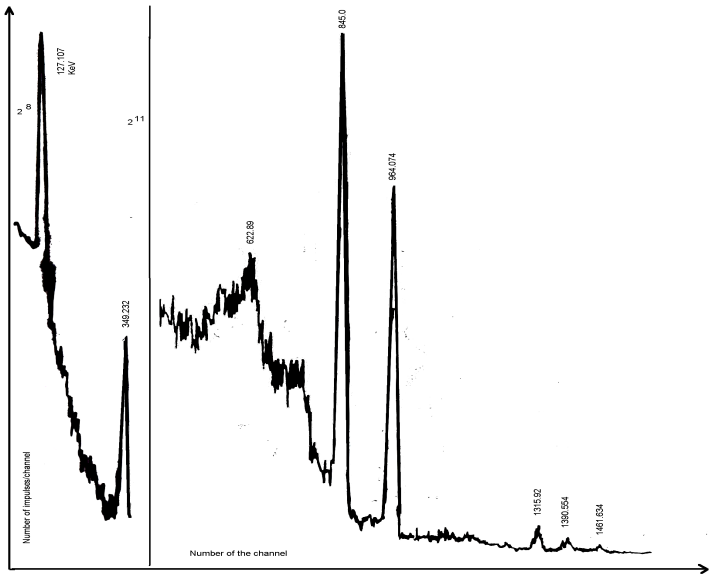

Fig.3. Gamma spectrum for Europium obtained by irradiation with isotopic neutron sources

The ^{226}Ra source was used to determine the global efficiency of the NaI(Tl) scintillator crystal (11.7 %) as well as the Ge(Li) detector's efficiency, as shown in Fig. 4. We also established a polynomial equation for efficiency as a function of the Gamma radiation's energy.

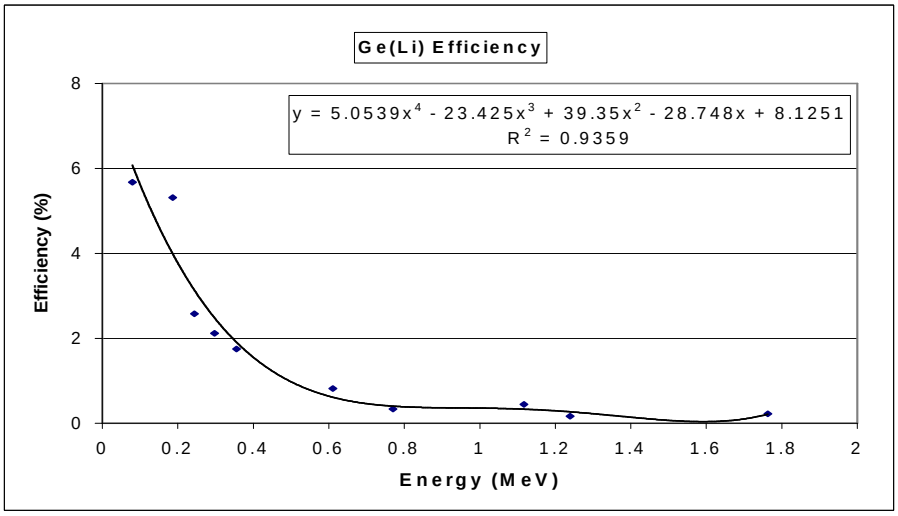

Fig. 4. The efficiency curve of Ge(Li) detector with an approximately 93 % precision

The disintegration curves for Sb and W obtained with the NaI(Tl) scintillator crystal are shown in Fig.5 and Fig.6, respectively. From these curves we determined the half-lives of the produced radioisotopes as being: 3 days for ^{122}Sb , 60 days for ^{124}Sb , 25.1 hours for ^{187}W and 9.3 hours for ^{152m}Eu . These radioisotopes were also studied in other papers as are the ones listed in [4-10].

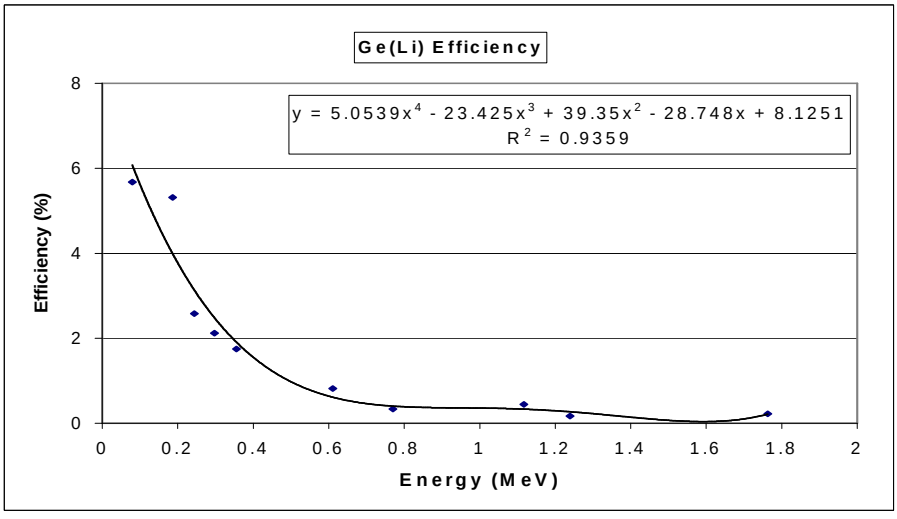

Fig. 5. The disintegration of ^{124}Sb and ^{122}Sb radioisotopes obtained with the NaI(Tl) scintillator crystal

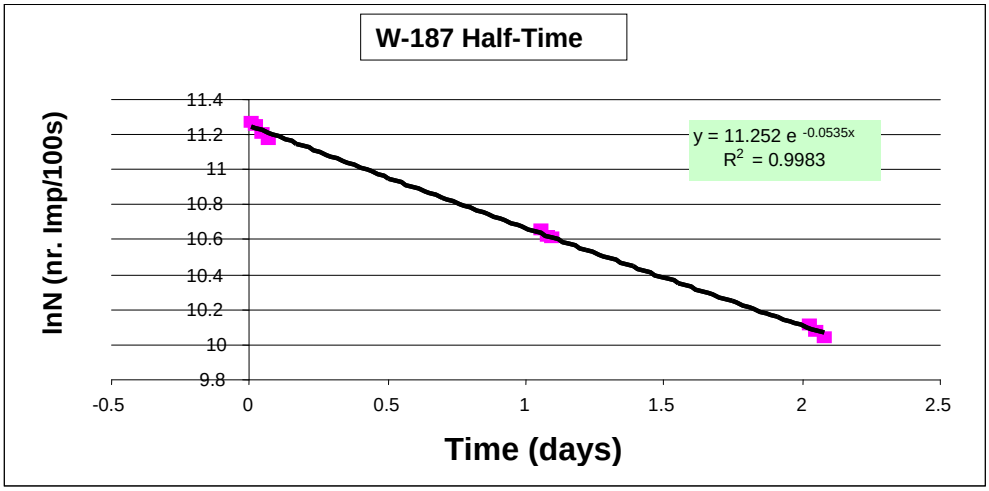

Fig.6. The disintegration curve of ^{187}W obtained with the NaI(Tl) scintillator crystal

Based on the energies obtained in the spectra as well as on the disintegration schemes we were able to identify the following radioisotopes: $^{124}Sb, ^{122}Sb, ^{152m}Eu, ^{187}W$.

For Sb we found the peaks of energy (KeV): 365.225, 384.772, 571.357, 507.385, 599.789, 1129.335, 1248.394, 1355.014, 1673.097, 1708.637. We concluded that these energies belong to ^{124}Sb (365.225, 384.772, 599.789, 1355.014, 1708.637) as well as to ^{122}Sb (571.357, 1129.335, 1248.394).

For W we found the following energies (KeV): 487.61, 560.18, 625.67, 692.93, 779.66, which we considered as belonging to ^{187}W and whose disintegration scheme is illustrated in Fig.7.

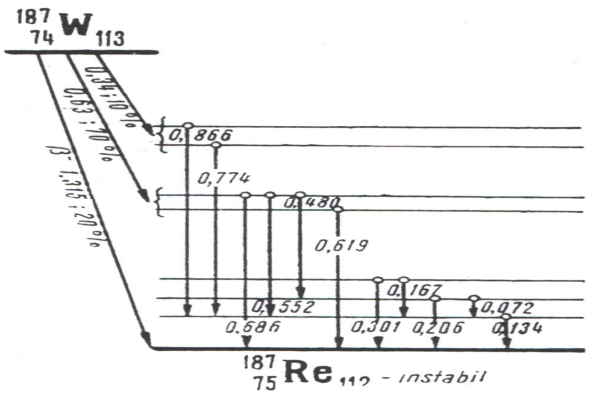

Fig.7. Disintegration scheme for ^{187}W .

For Eu we found the follwing peaks situated at the energies (KeV): 127.107, 349.232, 845.0, 964.074, 1315.92, 1390.554 corresponding to ^{152m}Eu [11]. We emphasize the fact that we did not identify the long-life radioisotope ^{152}Eu ($T_{1/2} = 13$ years).

We have calculated the activity for Europium using equation (1).

We obtained: $0.17 \pm 0.02\ \mu$ Ci.

Conclusions

From Sb disintegration curve we observe that by neutron irradiation of isotopic sources we were able to activate two radioisotopes: ^{122}Sb and ^{124}Sb. We produced these radioisotopes at a large scale, each sample having an activity of 0,2 μCi. They can be used as gamma laboratory sources for students' use as well as for other applications where different energies are required, other than the classical laboratory sources.

These radioisotopes are also used with excellent results in the neutron activated analysis of Sb and W from ores.

REFERENCES

1. De Soete D, Gijbels R, Hoste J - *Neutron Activation Analysis*, Wiley-Interscience, London, New York, Sydney, Toronto, 1972.
2. I.E. Teodorescu - *Generatoare de neutroni.Principii si utilizari*, Ed. Academiei Romane, Bucuresti, 1969.
3. D.Kiss, P. Quittner - *Neutronfizika*, Ed. Akademia, Budapest, 1971.
4. P. Sandru, Aurelia Topa - *Radionuclizii*, Ed. Academiei Romane, 1968.
5. V.L. Alexeev, H.G. Borner - *The level structure of 124-Sb and rezidual p-n interactions*, Nucl. Phys. **A345**, 93-133, 1980.
6. V.L. Alexeev, B.A. Emilianov, D.M. Kaminker, Yu.L. Khazov, I.A. Kondurov, Yu.E. Loginov, V.L. Rumiantsev, S.L. Sakharov and A.I. Smirnov, Nucl. Phys. **A262**, 19, 1976.
7. V.L. Alexeev, D.M. Kaminker, Yu.L. Khazov B.A. Emelianov, L.P. Kabina, I.A. Kondurov,YU.E. Loginov, V.L. Rumiantsev, S.L. Sakharov,E.K. Leushkin, A.I. Smirnov and P.A. Sushkov, Nucl.Phys. **A248**, 249, 1975.
8. V.L. Alexeev, D.M. kaminker, Yu.L. Khazov B.A. Emelianov, L.P. Kabina, I.A. Kondurov,YU.E. Loginov, E.K. Leushkin, A.I. Egorov, V.V. Martinov, V.L. Rumianstev, S.L. Sakharov, P.A. Sushkov, H.G.Borner, W.F. Davidson, J.A. Pinston and K. Schreckenbach, Nucl. Phys. **A297**, 373, 1978.
9. H. Ing, A. Kudoc, J.D. King and H.W. Taylor - Nucl. Phys. **A137**, 561, 1969.
10. M.R. Bhat, R.E. Chrien, D.I. Garber and O.A. Wasson, Phys.Rev. **C2**,1115, 1970.
11. R. H. Martin, K. I. W. Burns and J. G. V. Taylor, Nucl.Instr.&Meth., **390**, *1-2*, 267-273, 1997

STUDIA UNIVERSITATIS BABEŞ-BOLYAI, PHYSICA, XLIX, 1, 2004

PH DEPENDENCE OF THE FREE AND ADSORBED PAPAVERINE MOLECULAR SPECIES. VIBRATIONAL APPROACH

N. LEOPOLD[1,2*], S. CÎNTĂ-PÎNZARU[1], M. BAIA[1], C. LEHENE[1], O. COZAR[1], W. KIEFER[1]

[1] Faculty of Physics, Babeş-Bolyai University, Kogălniceanu 1, 400084 Cluj-Napoca, Romania; Corresponding author: e-mail: mleopold@phys.ubbcluj.ro; tel: +40-264-405300; fax: +40264591906

[2] Institut für Physikalische Chemie, Universität Würzburg, Am Hubland, 97074 Würzburg, Germany

ABSTRACT. The Raman spectra of papaverine aqueous solutions at acid pH values, as well as SERS spectra of papaverine adsorbed to colloidal silver surfaces at different acid and basic pH values were recorded and the assignments of papaverine vibrational modes were accomplished on the basis of density functional theory (DFT) calculations. The pH dependence Raman study is possible in the pH range under 6.5, for upper values the solubility being dramatically diminished. The pH dependence SERS spectra of papaverine reveals the chemisorption of the protonated and the neutral papaverine molecules to colloidal silver particles, as well as the coexistence of both molecular species adsorbed to the silver surface. The orientations to the silver surface of the two molecular species were discussed.

Introduction

Papaverine (Figure 1) is a natural heterocyclic nitrogen alkaloid used as pharmacological compound, which acts as a vasodilator to cause blood vessels to expand, increasing blood flow. The drug also serves as a muscle relaxer and acts directly on the heart muscle to depress conduction and prolong the refractory period. Therefore, the physiological and physical properties of the molecule and the interaction of papaverine with other biomolecules were extensively studied.[1,2,3,4,5]

Papaverine is also an alkaloid found in opium (*Papaver somniferum*). Therefore, the interest in forensic science for this compound is major. Several studies concerning the employment of spectroscopic methods for the detection of papaverine as a marker for heroine were performed in the last years.[6,7,8,9] Methods for rapid detection of papaverine at low concentrations are under continuous improvement. [10,11]

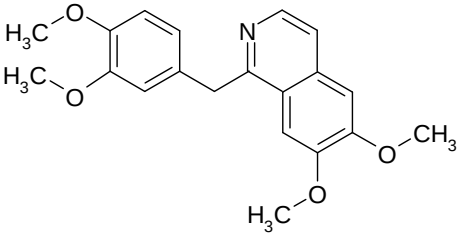

Figure 1. Chemical structure of papaverine.

Raman scattering contains useful structural information making it a powerful molecular investigation tool. Normal Raman scattering is a weak process, characterized by cross sections of ~ 10^{-29} cm^2. When the molecules are adsorbed to metal surfaces the Raman cross section is enhanced of at least 14 orders of magnitude and analytes in the micromole concentration can be investigated.[12,13,14,15,16]

The potential to combine high sensitivity with the structural information content of Raman spectroscopy makes SERS spectroscopy a powerful tool in a variety of fields,[17,18] including biospectroscopy.[19]

Raman spectra of papaverine at acid pH values as well as SERS spectra of papaverine at different acid and basic pH values were recorded and the assignments of papaverine vibrational modes were accomplished on the basis of density functional theory (DFT) calculations. To the best of our knowledge a SERS investigation or a complete vibrational approach of papaverine is missing in the literature.

Experimental

*Apparatus.*The FT-IR measurement of papaverine hydrochloride solid powder was performed using a Bruker Equinox 55 spectrometer. The Raman spectra of papaverine hydrochloride solid powder, the aqueous solutions at different pH values and SERS spectra on Ag colloid were recorded with a Dilor-Jobin Yvon Spex Groupe Horiba spectrometer equipped with 1800 grooves/mm holographic gratings.

The 514.5 nm output of a Spectra Physics argon ion laser was used as excitation line. The back-scattering geometry was adopted to collect the Raman and SERS spectra. A Peltier cooled charge coupled device (CCD) camera detection system and analysing software package LabSpec3.01 were employed for the acquisition of the data. The spectral resolution was set to 4 cm^{-1}.

Chemicals. All starting materials involved in substrate and solutions preparation were purchased from commercial sources as analytical pure reagents.

For the pH dependence Raman study, papaverine saturated aqueous solutions at different acid or basic pH values were prepared adding 10^{-1} mol l^{-1} HCl or NaOH solutions.

A sodium-citrate-reduced Ag colloid was employed as SERS substrate.[20] Small amounts of pH adjusted aqueous solution of papaverine were added to 2.5 ml of colloid, previously adjusted to the corresponding pH. Small amounts (1:10) of sodium chloride solution (10^{-2} mol l^{-1}) were added to produce aggregation of the colloidal silver particles for a considerable enhancement of the SERS signal.[21] The final concentration of papaverine in the SERS samples was 3.62 x 10^{-5} mol l^{-1}.

Calculations. Density functional theory (DFT) calculations of the structure and vibrational modes of the free papaverine molecule as well as Ag-papaverine complex were performed using the Gaussian 98 program package.[22] The theoretical calculations were carried out with Becke's 1988 exchange functional[23] and the Perdew-Wang 91 gradient corrected correlation functional (abbreviated as BPW91).[24] The Los Alamos effective core potential plus double zeta (LanL2DZ)[25,26,27] was employed for the silver atom, whereas the 6-31+G* Pople split-valence polarization basis set was used in the geometry optimisation and normal modes calculations for the other atoms. At the optimised structure of the examined species no imaginary frequency modes were obtained, proving that a local minimum on the potential energy surface was found.

The optimized geometries of the free papaverine and papaverine-Ag model complex are shown in Figure 2.

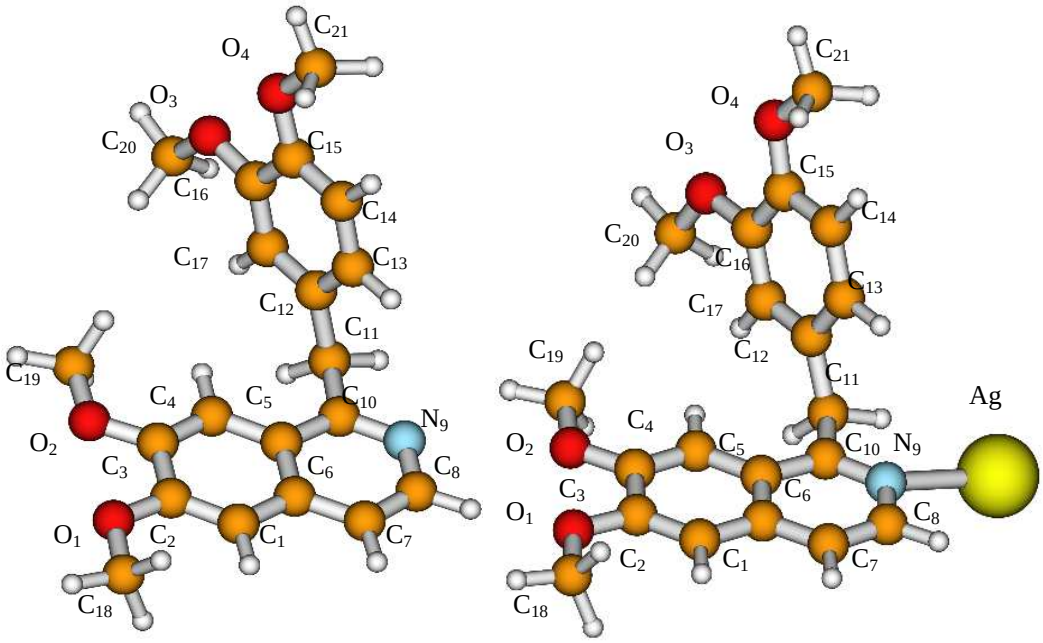

Figure 2. Optimised geometries of the free papaverine molecule and papaverine-Ag complex.

Results and discussion

Vibrational characterisation of papaverine

FT-IR and Raman spectra of papaverine hydrochloride in solid state are displayed in Figure 3. The Raman spectrum is the result of one accumulation of 100 s exposure time employing the 514.5 nm laser line. Taking in consideration that papaverine is available as hydrochloride, the papaverine molecules crystallized in the protonated molecular form. Consequently, the FT-IR and the Raman spectra presented in Figure 3 are due to the protonated molecular species of papaverine.

The vibrational fundamentals from the IR and Raman spectrum (Figure 3) were assigned by means of theoretical calculations. Table 1 contains the main wavenumbers of the experimentally obtained IR and Raman spectra of solid papaverine and the correspondent calculated wavenumbers (unscaled values) as well as the assignments of the vibrational modes of the papaverine molecule.

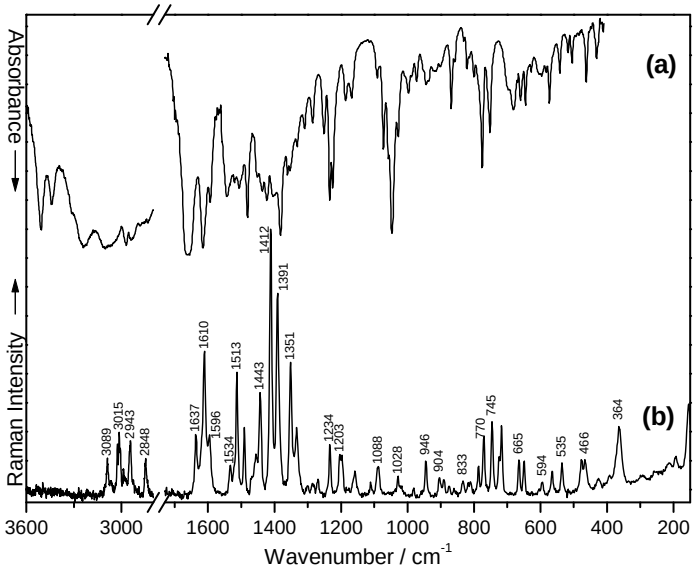

Figure 3. FT-IR (a) and Raman (b) spectra of solid papaverine hydrochloride.

A strict comparison between the experimental and calculated wavenumbers is not possible in this case, because the experimental data were obtained for the protonated molecular form of papaverine in solid state, whereas the theoretical results correspond to the unprotonated molecular form of papaverine in gaseous phase. It is well known that the calculated wavenumbers are obtained using the harmonic approximation, whereas the experimental wavenumbers are anharmonic by nature. Nevertheless, the quality of the quantum chemical results at the presented theoretical levels is sufficient to be useful for the assignment of the experimental data.

Table 1.

The experimental IR, Raman, SERS and the calculated wavenumbers (cm^{-1}) of the free papaverine molecule and the Ag-papaverine complex.

IR	Raman solid	Raman liquid pH 6.5	SERS pH 10	Calc.[a]	Calc.[b]	Assignment
	152 m			151	156	C2O1, C3O2, C16O3, C15O4 twist
	190 w			198	197	CH3 + CH2 def
	211 w			207	212	CH3 + CH2 def
			212 s			Ag-N str
	249 w			244	245	CH3 + CH2 def
	294 w			296	298	ring1 out of plane def + CH3 (C18, C19) def
	364 m	371 s	362 s	360	357	ring2 out of plane def + CH2 def
411 w	390 w			406	411	CH2 def

IR	Raman solid	Raman liquid pH 6.5	SERS pH 10	Calc.[a]	Calc.[b]	Assignment
424 sh	422 w			449	453	C1C2O1, C4C3O2 wag
430 m				452	457	C1C2O1, C4C3O2 wag
461 m	466 m	467 w	466 w	459	461	C17C16O3, C14C15O4 wag
	475 m	485 w	481 w	476	478	C1C6C7, C4C5C10 wag
516 m		536 w	528 w	519	519	ring1 + ring2 out of plane def
540 m	535 m			554	552	ring1 + ring2 out of plane def
573 m	564 m	576 w	573 w	566	563	ring1 + ring2 out of plane def
595 m	594 w			598	595	ring1 + ring2 out of plane def
604 m	602 w			617	619	C1C2O1, C4C3O2 bend
626 m	627 w			632	639	ring1 + ring2 in plane def
644 m	647 m	654 w	647 w	649	653	ring1 + ring2 in plane def
659 m		671 w	661 w	678	689	C1C2O1, C4C3O2, C17C16O3, C14C15O4 twist
668 sh	665 m			688	694	C1C2O1, C4C3O2, C17C16O3, C14C15O4 twist
	716 m	722 m	714 m	721	715	ring1 + ring2 out of plane def+ C10C11C12 def
	722 sh	735 m	725 m	725	727	ring1 + ring2 out of plane def+ C10C11C12 def
752 s	745 m	740 m	737 sh	761	761	ring1 in plane def
776 s	770 m	776 m	765 m	769	766	CH wag
	784 m	794 w	781 w	787	782	CH wag
800 m	809 w			790	790	CH twist
813 sh	815 w			814	819	CH twist
831 sh	833 w			830	836	CH twist
868 m	873 w			876	866	ring1 in plane def
	889 w			884	882	CH twist (ring2) + CH2 def
901 m	904 m	900 w	892 w	906	912	CH twist (ring2) + CH2 def
917 m	923 w	923 w	928 w	925	921	CH twist (ring2) + CH2 def
943 m	946 m	953w	947 w	939	947	C10C11C12 def + CH2 def
987 sh	980 w			992	994	C10C11C12 def + CH2 def
1027 m	1028 m	1031 w	1024 w	1034	1033	trigonal str (ring1, ring2)
1047 s	1044 w			1041	1040	trigonal str (ring1, ring2)
1073 s	1078 sh			1052	1052	C18O1, C19O2, C20O3, C21O4 str
	1088 m	1098 m	1079 m	1082	1086	C18O1, C19O2, C20O3, C21O4 str
1091 m	1109 w			1111	1116	CH bend (ring2)
	1147 sh		1126 m	1146	1145	CH bend (ring2)
1168 m	1156 m	1155 w	1168 w	1161	1160	C11C12 str + CH bend (ring2)
	1195 m	1201 sh	1188 w	1199	1200	C2O1, C3O2 str + CH rock (ring1)
	1203 m	1209 w	1204 w	1216	1218	CH bend (ring1) + C10C11 str
1225 s	1224 sh			1237	1238	CH bend (ring2) + C15O4, C16O3 str
1234 s	1234 m	1242 w	1233 w	1242	1246	CH rock (ring1, ring2) + CH2 def
1251 s	1267 w	1275 w	1271 w	1266	1269	CH rock (ring1, ring2) + CH2 def
1284 m	1284 w			1282	1282	CH rock (ring1, ring2) + C2O1, C3O2, C16O3, C15O4 str
1308 m	1299 w			1302	1306	CH rock (ring1, ring2) + CH2 def

IR	Raman solid	Raman liquid pH 6.5	SERS pH 10	Calc.[a]	Calc.[b]	Assignment
1330 m	1331 m			1323	1325	CH2 def + CC str (ring1, ring2)
1352 m	1351 m			1353	1358	ring2 str
1361 m		1364 s	1358 s	1370	1376	ring2 str
1381 s	1391 s			1379	1386	ring2 str
1403 s	1412 s	1411 s	1392 s	1391	1394	ring1 str
1423 s	1423 sh	1423 s	1423 s	1424	1421	ring1 str
1436 m	1443m	1446 m	1448 w	1443	1443	CH3, CH2 def
1451 m	1451 sh			1452	1449	CH3, CH2 def
	1463 sh	1463 w	1463 w	1462	1464	CH3, CH2 def
1480 s	1487 m	1489 w	1481 m	1487	1484	CH3, CH2 def
1506 m	1513 m	1498 m	1509 m	1516	1518	ring1 + ring2 str
1520 m	1534 m	1518 m	1518 sh	1523	1523	ring1 + ring2 str
1544 m		1558 w	1543 w	1564	1562	ring1 + ring2 str
1592 m	1596 m	1576 w	1564 w	1589	1591	ring1 + ring2 str
	1610 m	1600 sh	1591 sh	1593	1595	ring1 + ring2 str
1614 s	1615 sh	1619 sh	1604 m	1612	1612	ring1 + ring2 str
1645 s	1637 m		1648 s	1623	1622	ring1 + ring2 str
2835 m	2848 m	2855 m	2841 m	2877	2878	CH str (CH2, CH3)
2857 m				2898	2900	CH str (CH2, CH3)
2881 m	2894 w		2917 sh	2904	2907	CH str (CH2, CH3)
2928 sh	2921 sh	2959 m	2940 m	2946	2946	CH str (CH2, CH3)
2941 m	2943 m			2971	2974	CH str (CH2, CH3)
2969 w	2973 w			3001	3008	CH str (CH2, CH3)
	3015 m		3020 m	3058	3054	CH str (ring1, ring2)
	3022 m		3077 m	3065	3063	CH str (ring1, ring2)
	3065 m			3089	3090	CH str (ring1, ring2)
3088 sh	3089 m			3110	3111	CH str (ring1, ring2)

Abbreviations: [a] calculations for the free molecule at the BPW91/6-31+G* level of theory, [b] calculations for the Ag-papaverine complex at the BPW91/Gen 5d Pseudo=LanL2, N, C, O, H 6-31+G*, Ag LanL2DZ level of theory, w-weak, m-medium, s-strong, sh-shoulder, ring1-isoquinoline ring, ring2-benzene ring, def-deformation, str-stretching, bend-bending, rock-rocking, wag-waging, twist-twisting.

pH dependence Raman spectra

Papaverine is available as papaverine hydrochloride, therefore for pH values over 2 sodium hydroxide solution was added to increase the pH of the papaverine solution. The Raman spectra of papaverine aqueous solution in the pH range from 1 to 6 were unchanged (Figure 4). The highest obtained pH value was 6.5, a further addition of sodium hydroxide leading to the desolvation of papaverine from the solution and the Raman signal was too weak for recording any spectra. This fact is supposed to be due to the deprotonation process of the papaverine

molecules at this pH, whereas the unprotonated molecular species are weak water soluble. Therefore, the pK_a value for the protonation of the N atom of the papaverine molecule has to be at about 6.5. At pH values over 6, nearing to the pK_a value of papaverine, according to the Handerson-Hasselbach equation[28] the number of neutral papaverine molecules increases considerably. Notable differences in band positions and relative intensities appear between the Raman spectra at pH 6 and 6.5, the bands at 1364 and 1423 cm^{-1} become very intense in the aqueous solution Raman spectrum at pH 6.5. These bands are due to the presence of also neutral papaverine molecular species in the aqueous solution.

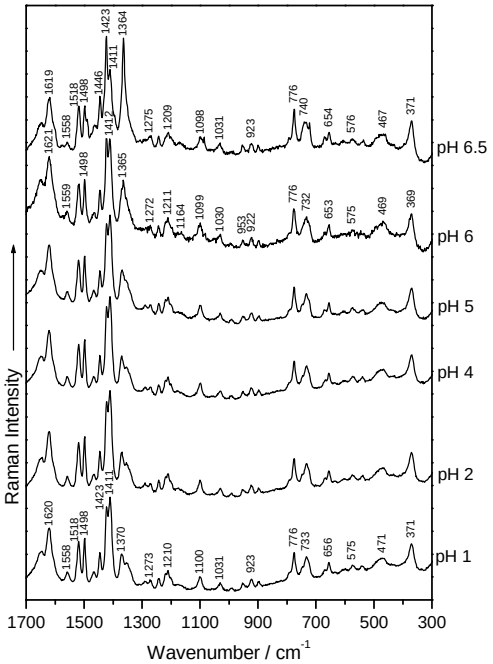

Figure 4. Raman spectra of papaverine aqueous saturated solution at different pH values, as indicated. (Excitation 514.5 nm, laser power 250 mW)

pH dependence SERS spectra

A versatile tool to study the vibrational behavior in the pH domain with low solubility is SERS spectroscopy, due its sensitivity – the potential of detection under the micromole level.

SERS spectra in the pH range from 1 to 10 were obtained and discussed (Figure 5).

The SERS spectral features can be divided in three parts. Firstly, in the 2 – 4.5 pH range only protonated papaverine molecules are adsorbed to the silver surface, secondly in the 5 – 6.5 pH range on the silver surface coexist both molecular species, protonated and neutral and thirdly in the 7 – 10 pH range only neutral molecules are adsorbed to the silver surface.

The characteristic band for the adsorbed protonated molecular species in the SERS spectra in the 2 – 4.5 pH range is the most intense band at 1396 cm^{-1}. On passing from pH 4.5 to pH 5 the characteristic SERS band due to the adsorbed protonated papaverine species decreases in intensity and new intense bands at 1355, 1423, 1482 and 1506 cm^{-1} appear in the spectrum. These new bands are attributed as characteristic bands of the neutral papaverine molecular species adsorbed to the silver surface. The assignments of these bands are shown in Table 1.

The coexistence of neutral molecular species with the protonated ones adsorbed to the silver surface already at pH 5 is not surprisingly, so far as several SERS studies[29,30,31] reported the adsorption of the unprotonated molecular form at pH values lower with two or more units than the pK_a value of the analyte.

At pH 6 and 6.5 the coexistence of the neutral molecular species with the protonated ones adsorbed to the silver surface is more evident. The peak at 1396 cm^{-1}, due to the protonated papaverine molecules, further decreases in intensity, whereas the peaks at 1355, 1423, 1482 and 1506 cm^{-1} attributed to the neutral papaverine molecular species increase in intensity, revealing that the number of neutral molecules adsorbed to the silver surface is increasing.

At pH values over 6.5, the lack of the characteristic band of the protonated papaverine molecular species and the presence of the strong bands at 1358, 1423, 1481 and 1509 cm^{-1}, evidence the exclusive adsorption of the neutral papaverine molecules to the silver surface.

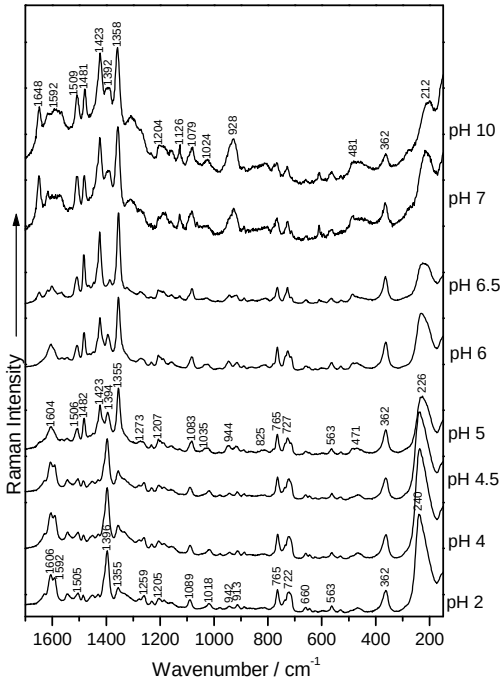

Figure 5. SERS spectra of papaverine adsorbed to colloidal silver particles at different pH values, as indicated. (Excitation 514.5 nm, laser power 200 mW)

Adsorbates orientation

By comparing the Raman spectra (Figure 4) to the SERS spectra (Figure 5) one can see that most of the bands are shifted to lower wavenumbers evidencing a chemisorption of the papaverine molecule to the silver surface.

In the SERS spectra at acid pH values the papaverine-Ag stretching vibration is overlapped by the strong Ag-Cl^- stretching band at around 240 cm^{-1}. With the increasing of the pH, the concentration of the Cl^- ions decreases and consequently the band profile is dramatically changed, the papaverine-Ag stretching band at about 226 cm^{-1} becomes evident.

Theoretically, the interaction of papaverine with the silver surface can be established through the lone pairs of the one N or of the O atoms or through the π electrons of the rings.

Insignificant enhancement of any vibrational mode involving O atoms was noticed, reflecting the absence of the interaction with the surface through one or more O atoms.

Moreover, when protonated papaverine molecular species are adsorbed to the silver surface, the N atom is protonated, therefore, the adsorption through this atom is less probably. Consequently, we conclude that the protonated papaverine molecules adsorb to the silver surface through the π electrons of the rings. Most of the Raman bands of the protonated papaverine molecules (Figure 4) can be retrieved in the SERS spectra. According to the electromagnetic field enhancement theory of SERS, the field enhancement rapidly decreases with increasing distance from the metal surface.[11,12] Vibrations belonging to the isoquinoline ring at 1396 cm^{-1} and benzene ring at 362 cm^{-1} (Table 1) are present in the SERS spectra (Figure 5). Consequently, it can be concluded that both rings lay in the vicinity of the silver surface.

At pH values over 5 the neutral papaverine molecule adsorbs most probably through the lone pair electrons of the N atom from the isoquinoline ring, so that the isoquinoline and the benzene ring are more probably tilted oriented to the silver surface. The Ag-N vibration is evidenced by the strong band at about 226 cm^{-1}. Table 1 also contains the main wavenumbers of the SERS spectrum at the pH value 10 and the calculated wavenumbers (unscaled values) of the papaverine molecule when a silver atom is attached to the nitrogen atom from the isoquinoline ring. Also, in this case a strict comparison between the theoretical wavenumbers and experimental ones is not possible because a simple attachment of an Ag atom can not reproduce the complexity of the SERS effect. However, the calculations performed on this papaverine-Ag model SERS complex could be regarded as a first step that contributes to a better understanding of the chemisorption effect on the vibrational behavior of the adsorbed molecule.

Conclusions

A detailed experimental and theoretical vibrational structural characterization of the protonated and neutral molecular species of papaverine was performed.

The pH dependence Raman study is possible in the pH range under 6.5, for upper values the solubility being dramatically diminished. However, the Raman study allows to evidence the two papaverine species, protonated and neutral, respectively.

SERS spectroscopy can evidence the protonated or neutral papaverine species at the 10^{-5} mol l^{-1} level. The pH dependence SERS spectra of papaverine reveal the chemisorption of the protonated and the neutral papaverine molecules to the silver surface, as well as the coexistence of both molecular species adsorbed to the silver surface. The protonated molecular species adsorb to the silver surface through the π electrons of the rings, whereas the neutral molecules through the N atom of the papaverine molecule. Either in acid or in basic media, the oxygen adsorption of papaverine species was excluded.

REFERENCES

1. C. A. Ventura, G. Puglisia, M. Zappalab, G. Mazzonea, *Int. J. Pharm.* 160 (1998), 163.
2. V. E. Yushmanov, J. R. Perussi, H. Imasato, M. Tabak, *Biochim. Biophys. Acta* 1189 (1994), 74.
3. C. A. Ventura, M. Fresta, D. Paolino, S. Pedotti, A. Corsaro, G. Puglisi, *J. Drug. Target* 9 (2001), 379.
4. S. Cîntă Pînzaru, I. Pavel, N. Leopold, W. Kiefer, accepted paper, *Spectrochim. Acta A.*
5. N. Leopold, J. R. Baena, M. Bolboacă, O. Cozar, W. Kiefer, B. Lendl, *Raman, IR and surface enhanced Raman spectroscopy of papaverine. An automatized setup for in situ synthesize of the silver substrate and recording of the SER spectra*, submitted for publication.
6. R. Brenneisen, F. Hasler, *J. Forensic Sci*. 47 (2002), 885.
7. M. J. Bogusz, R. D. Maier, M. Erkens, U. Kohls, *J. Anal. Toxicol*. 25 (2001), 431.
8. B. D. Paul, C. Dreka, E. S. Knight, M. L. Smith, *Planta Med*. 62 (1996), 544.
9. V. C. Trenerry, R. J. Wells, J. Robertson, *J. Chromatogr*. A 718 (1995), 217.
10. N. T. Abdel-Ghani, A. F. Shoukry, Y. M. Issa, O. A. Wahdan, *J. Pharm. Biomed. Anal. 28* (2002), 373.
11. M. Eisman, M. Gallego, M. Varcarcel, *J. Pharm. Biomed. Ana*l. 12 (1994), 179.
12. M. Moskovits, *Rev. Mod. Phys. 57* (1985), 783.
13. A. Otto, J. Billmann, J. Eickmans, U. Ertuerk, C. Pettenkofer, *Surf. Sci.* 138 (1984), 319.
14. A. Otto, I. Mrozek, H. Grabhorn, W. Akemann, *J. Phys.: Condens. Matter* 4 (1992), 1143.
15. J. A. Creighton, In *Spectroscopy of Surfaces*, R. J. H. Clark, R. E. Hester, Eds., Wiley: New York (1988), p 37.
16. A Campion, P. Kambhampati, *Chem. Soc. Rev.*, 27 (1998), 241.
17. K. Kneipp, H. Kneipp, I. Itzkan, R. R. Dasari, M. S. Feld, *Chem. Rev.* 99 (1999), 2957.
18. S. Nie, S. R. Emeroy, *Science* 275 (1997), 1102.
19. T. M. Cotton, In *Spectroscopy of Surfaces*, R. J. H. Clark, R. E. Hester, Eds., Wiley: New York (1988), p.91.
20. P. Lee, D. Meisel, *J. Phys. Chem.* 86 (1982), 3391.

21. S. E. Brandt, T. M. Cotton, *Physical Methods of Chem. Series,* 2nd ed.; Vol. IXB; Wiley (1993); p. 670.
22. Gaussian 98, Revision A7, *Gaussian Inc. Pittsburgh PA* (1998).
23. A. D. Becke, *Phys. Rev. A* 38 (1988), 3098.
24. J. P. Perdew, Y. Wang, *Phys. Rev. B* 45 **(**1992), 13244.
25. P. J. Hay, W. R. Wadt, *J. Chem. Phys*. 82 (1985), 270.
26. W. R. Wadt, P. J. hay, *J. Chem. Phys*. 82 (1985), 284.
27. P. J. Hay, W. R. Wadt, *J. Chem. Phys*. 82 (1985), 299.
28. P. W. Atkins, *Physikalische Chemie*, VCH, Weinheim (1987), p. 288.
29. B. Giese, D. Mc Naughton, *J. Phys. Chem. B* 106 (2002), 1461.
30. N. Leopold, V. Chiş, S. Cîntă-Pînzaru, O. Cozar, W. Kiefer, "*Raman and surface-enhanced Raman study of metoclopramide at different pH values*", manuscript in preparation.
31. N. Leopold, S. Cîntă-Pînzaru, M. Bolboacă, O. Cozar, W. Kiefer, J. Popp, *"The pH influence on the adsorption of thiamine to colloidal gold surfaces monitored by surface-enhanced Raman spectroscopy*", submitted for publication.

1. C. A. Ventura, G. Puglisia, M. Zappalab, G. Mazzonea, *Int. J. Pharm.* 160, (1998), 163.
2. V. E. Yushmanov, J. R. Perussi, H. Imasato, M. Tabak, *Biochim. Biophys. Acta* 1189, (1994), 74.
3. C. A. Ventura, M. Fresta, D. Paolino, S. Pedotti, A. Corsaro, G. Puglisi, *J. Drug. Target* 9, (2001), 379.
4. S. Cîntă Pînzaru, I. Pavel, N. Leopold, W. Kiefer, accepted paper, *Spectrochim. Acta A.*
5. N. Leopold, J. R. Baena, M. Bolboacă, O. Cozar, W. Kiefer, B. Lendl, *Raman, IR and surface enhanced Raman spectroscopy of papaverine. An automatized setup for in situ synthesize of the silver substrate and recording of the SER spectra*, submitted for publication.
6. R. Brenneisen, F. Hasler, *J. Forensic Sci*. 47, (2002), 885.
7. M. J. Bogusz, R. D. Maier, M. Erkens, U. Kohls, *J. Anal. Toxicol*. 25, (2001), 431.
8. B. D. Paul, C. Dreka, E. S. Knight, M. L. Smith, *Planta Med*. 62, (1996), 544.
9. V. C. Trenerry, R. J. Wells, J. Robertson, *J. Chromatogr*. A 718, (1995), 217.
10. N. T. Abdel-Ghani, A. F. Shoukry, Y. M. Issa, O. A. Wahdan, *J. Pharm. Biomed. Anal. 28*, (2002), 373.
11. M. Eisman, M. Gallego, M. Varcarcel, *J. Pharm. Biomed. Ana*l. 12, (1994), 179.
12. M. Moskovits, *Rev. Mod. Phys. 57*, (1985), 783.
13. A. Otto, J. Billmann, J. Eickmans, U. Ertuerk, C. Pettenkofer, *Surf. Sci.* 138, (1984), 319.
14. A. Otto, I. Mrozek, H. Grabhorn, W. Akemann, *J. Phys.: Condens. Matter* 4, (1992), 1143.
15. J. A. Creighton, In *Spectroscopy of Surfaces*, R. J. H. Clark, R. E. Hester, Eds., Wiley: New York, (1988), p 37.
16. A Campion, P. Kambhampati, *Chem. Soc. Rev.*, 27, (1998), 241.
17. K. Kneipp, H. Kneipp, I. Itzkan, R. R. Dasari, M. S. Feld, *Chem. Rev.* 99, (1999), 2957.
18. S. Nie, S. R. Emeroy, *Science* 275, (1997), 1102.
19. T. M. Cotton, In *Spectroscopy of Surfaces*, R. J. H. Clark, R. E. Hester, Eds., Wiley: New York, (1988) p.91.
20. P. Lee, D. Meisel, *J. Phys. Chem.* 86, (1982), 3391.
21. S. E. Brandt, T. M. Cotton, *Physical Methods of Chem. Series,* 2nd ed.; Vol. IXB; Wiley, (1993); p. 670.
22. Gaussian 98, Revision A7, *Gaussian Inc. Pittsburgh PA* (1998).
23. A. D. Becke, *Phys. Rev. A* 38, (1988), 3098.
24. J. P. Perdew, Y. Wang, *Phys. Rev. B* 45**,** (1992), 13244.
25. P. J. Hay, W. R. Wadt, *J. Chem. Phys*. 82, (1985), 270.
26. W. R. Wadt, P. J. hay, *J. Chem. Phys*. 82, (1985), 284.
27. P. J. Hay, W. R. Wadt, *J. Chem. Phys*. 82, (1985), 299.
28. P. W. Atkins, *Physikalische Chemie*, VCH, Weinheim, (1987), p. 288.
29. B. Giese, D. Mc Naughton, *J. Phys. Chem. B* 106, (2002), 1461.
30. N. Leopold, V. Chiş, S. Cîntă-Pînzaru, O. Cozar, W. Kiefer, "*Raman and surface-enhanced Raman study of metoclopramide at different pH values*", manuscript in preparation.
31. N. Leopold, S. Cîntă-Pînzaru, M. Bolboacă, O. Cozar, W. Kiefer, J. Popp, *"The pH influence on the adsorption of thiamine to colloidal gold surfaces monitored by surface-enhanced Raman spectroscopy*", submitted for publication.

STUDIA UNIVERSITATIS BABEŞ-BOLYAI, PHYSICA, XLIX, 1, 2004

COMPUTER SIMULATION OF A CZERNY – TURNER MOUNT MONOCHROMATOR

ALPAR SIMON[1]*, SORIN DAN ANGHEL[1], TIBERIU FRENȚIU[2], EUGEN DARVASI[2] and ZSOLT VISKI[2]

[1] Babes-Bolyai University, Faculty of Physics, Department of Electricity, Magnetism and Electronics, 400084 Cluj-Napoca, Kogalniceanu 1, Romania
[2] Babes-Bolyai University, Faculty of Chemistry and Chemical Engineering, Department of Analytical Chemistry, 400028 Cluj-Napoca, Kogalniceanu 1, ROMANIA
** corresponding author*

ABSTRACT. A FORTRAN 77 based computer simulation program is presented, The software allows the simulation and computation of the parameters of a Czerny-Turner mount monochromator. The program was succesfully used to compute some working characteristics of the monochromator: incidence– and diffration angles, disperions and boradenings. The main goal was to present a basic method to compute those parameters, thus the optimization of the computation code was fully neglected. The program may be transformed in the near future, to provide a user-friendly graphical interface. The program could be a very useful tool in taking decisions about the properties of a future monochromator which could be purchesed by the users Lab or it could be a useful educational tool. It was shown that it is also very useful in computing some instrumental parameters necessary to obtain synthetic spectra.

1. Introduction

Spectroscopy is the study of electromagnetic spectra (wavelength composition of light) due to atomic and/or molecular interactions. Since 18th century, spectroscopy has been very important in the study of physics and it was a very important investigation tool in astronomy. Nowadays it is equally important, under it's multiple aspects in biological, chemical, metallurgical and other analytical investigations.

The study of the electromagnetic spectra is enabled by an optical system called spectrometer. This device allows the isolation of a narrow band of radiation from a light source in order to analyze it. A typical spectrometer design consists of a dispersing (separating) element, entrance and exit slits, collimating and transmitting mirrors and a detector. The most important parameters of this device are:

i) the bandpass (transmitted wavelength range)
ii) dispersion (separation of light, function of wavelength)
iii) resolution (minimum bandpass)

The challenge to build good spectrometers has attracted the attention of many scientific laboratories. This task proved to be a very difficult one needing a good harmony between theory and technology.

Computer simulation of the optical functioning of a spectrometer could provide very useful information for the design of such devices.

The present paper will present a generic code allowing the simulation and computation of the parameters of a Czerny-Turner mount monochromator. The computational program is given in FORTRAN 77 [1].

2. Physics of diffraction grating based monochromators

The physics of diffraction grating based monochromators is described extensively in many references [2, 3]. A diffraction grating is a collection of reflecting (or transmitting) elements separated by a distance comparable to the wavelength of the studied electromagnetic radiation. A reflection grating consists of a grating superposed on a reflective surface. The electromagnetic radiation incident on the grating will, upon diffraction, have its electric amplitude or phase, or both, modified in a predictable manner. A plane grating is one whose surface is flat. They are normally used in collimated incident light, which is dispersed by wavelength but do not focused. These mounts require auxiliary optics (lenses and mirrors) to collect and focus the energy.

A monochromator is a spectrometer that images a simple wavelength or a wavelength-band at a time onto an exit slit, the spectrum being scanned by the relative motion of the entrance (and/or exit) optics (usually slits) with respect to the grating. One of the most popular mounting is the Czerny-Turner mount (Fig.1).

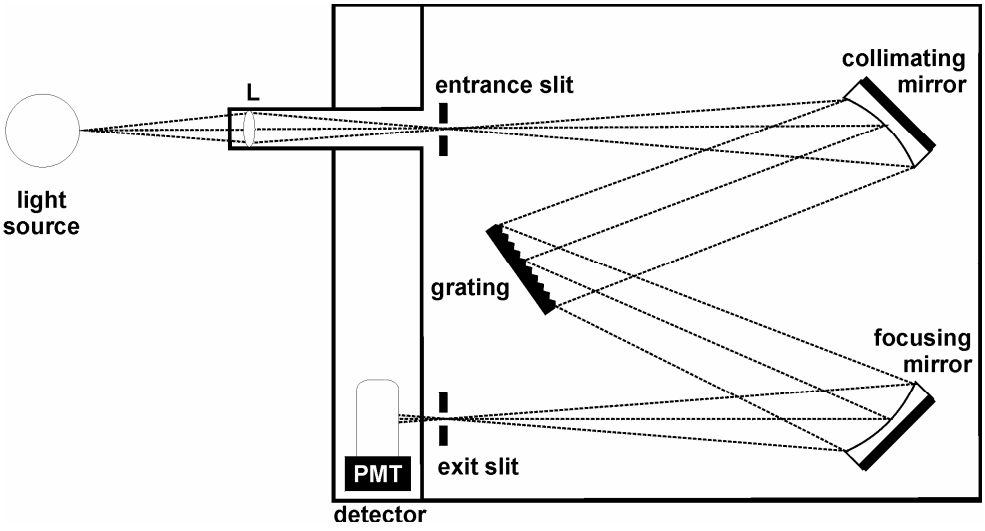

Fig.1 – The Czerny-Turner mount

This design involves a classical plane grating illuminated by light. The incident light is diverging from the entrance slit and it is collimated by a concave mirror (collimator) and than transmitted to the diffraction grating. The diffracted light will be focused by a second concave mirror (camera). The wavelengths are imaged individually. The spectrum is scanned by the rotation of the grating.

2.1 The grating equation

When lights is incident on a grating, it is diffracted into discrete directions. The geometrical path difference between light coming from adjacent grooves is $d(\sin\hat{i} + \sin\hat{r})$. Due to the basic principles of interference, only when this difference equals the wavelength of the light (λ) or some integral multiple thereof, will the light from adjacent grooves be in phase and leading to interference. The relationships are expressed in one relation, known as grating equation:

$$\begin{aligned} m\lambda &= d\left(\sin\hat{i} + \sin\hat{r}\right) \\ Gm\lambda &= \sin\hat{i} + \sin\hat{r} \end{aligned} \tag{1}$$

where G = 1/d is the groove frequency, groove density or pitch, and m is a postive integer, called diffraction order.

As one could tell from Eq(1) there are several wavelengths and diffraction orders at a given incidence angle (*i*) and diffraction angle (*r*) which are satisfying the grating equation (Fig.2).

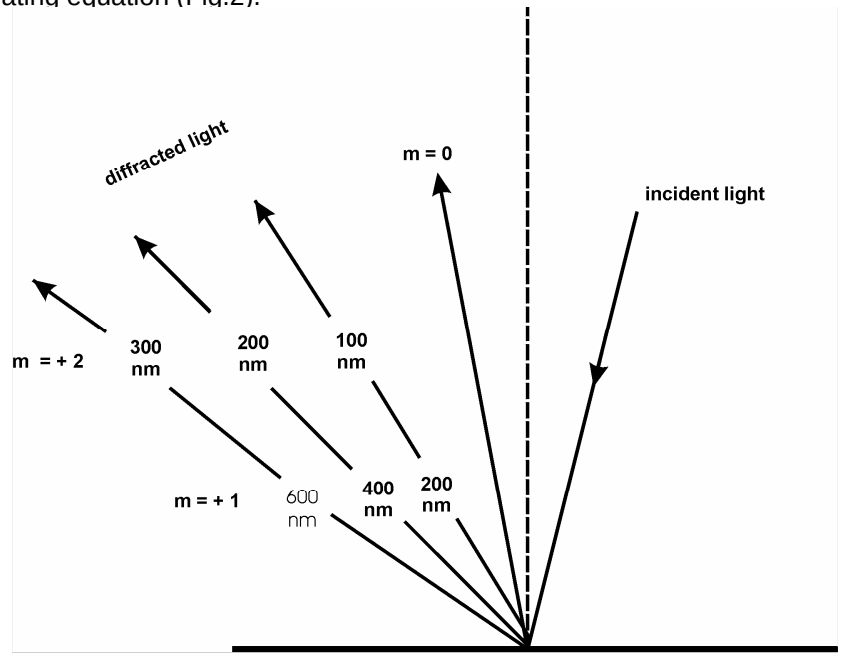

Fig. 2 – Wavelengths and diffraction orders

2.2 Dispersion

Dispersion is a measure of the separation (either angular, spatial or reciprocal) between diffracted light of different wavelengths. The primary purpose of a diffraction grating in a monochromator is to disperse light by wavelength. A beam of white light incident on a grating will be separated into its component colors upon diffraction from the grating, with each color diffracted along a different direction.

2.2.1 Angular dispersion (AD)

Angular dispersion expresses the spectral range per unit angle:

$$AD = \frac{\partial \hat{r}}{\partial \lambda} = \frac{m}{d \cos \hat{r}}$$
$$AD = \frac{\sin \hat{i} + \sin \hat{r}}{\lambda \cos \hat{r}} \quad (2)$$

2.2.2 Linear dispersion (LD)

Linear dispersion expresses the spectral range per unit length:

$$LD = \frac{\partial x}{\partial \lambda} \quad (3)$$

It could be expressed as the product between the angular dispersion and the effective focal length of the spectrometer.

$$LD = F \cdot AD = F \cdot \frac{m}{d \cos \hat{r}} = F \cdot \frac{\sin \hat{i} + \sin \hat{r}}{d \cos \hat{r}} \quad (4)$$

$$x = F \cdot \hat{r} \;\Rightarrow\; dx = F \cdot d\hat{r}\,,\; \frac{dx}{d\lambda} = F \cdot \frac{d\hat{r}}{d\lambda} = F \cdot AD \quad (5)$$

2.2.3 Reciprocal linear dispersion (RLD)

One of the most important monochromator parameter is the reciprocal linear dispersion or plate factor. It is a measure of the change in wavelength corresponding to a change in location along the spectrum. It is simply expressed as the reciprocal of the linear dispersion:

$$RLD = \frac{1}{LD} = \frac{d \cos \hat{r}}{F \cdot m} = \frac{d \cos \hat{r}}{F \cdot \left(\sin \hat{i} + \sin \hat{r}\right)} \quad (6)$$

2.3 Resolving power (R)

The resolving power(R) of a grating is a measure of its ability to separate adjacent spectral lines of average wavelength (λ). It is usually expressed as the dimensionless quantity.

$$R = \frac{\lambda}{\Delta \lambda} \quad (7)$$

where $\Delta\lambda$ is the limit of resolution (the difference in wavelength between two lines of equal intensity that can be distinguished separately). The theoretical resolving power of a planar diffraction grating is given in elementary optics textbooks as:

$$TR = m \cdot N \quad (8)$$

where N is the total number of grooves illuminated on the surface of the grating (= illuminated width multiplied by 1/d).

$$TR = N \cdot \frac{d\left(\sin\hat{i} + \sin\hat{r}\right)}{\lambda} \tag{9}$$

since $\left|\sin\hat{i} + \sin\hat{r}\right| \leq 2$ the maxim resolving power is:

$$R_{MAX} = \frac{2Nd}{\lambda} \tag{10}$$

2.4 Spectral resolution

The resolving power can be considered an exclusive characteristic of the grating and depends on the angles at which it is used.

The ability to separate two wavelengths λ_1 and $\lambda_2 = \lambda_1 + \Delta\lambda$ generally depends not only on the grating but on the location and dimensions of the entrance and exit slits, the aberrations and magnifications. The minim wavelength difference $\Delta\lambda$ between two wavelengths that can be resolved unambiguously can be determined by convoluting the image of the entrance slit with the exit slit.

2.5 Bandpass

In the most fundamental sense both bandpass and resolution are used as measure of an instrument's ability to separate adjacent spectral lines.

Assuming a continuum light source, the bandpass of an instrument is the spectral interval that may be isolated. This depends on many factors including the width of the grating, system aberrations, spatial resolution of the detector, and entrance and exit slit widths. If a light source emits a spectrum which consists of a single monochromatic wavelength lambda λ_o and is analyzed by a perfect spectrometer, the output should be identical to the spectrum of the emission which is a perfect line at precisely lambda λ_o. In reality spectrometers are not perfect and produce an apparent spectral broadening of the purely monochromatic wavelength. The line profile now has finite width and is known as the "instrumental line profile" (instrumental bandpass).

The instrumental profile may be determined in a fixed grating spectrograph configuration with the use of a reasonably monochromatic light source such as a single mode dye laser: for a given set of entrance and exit slit parameters, the grating is fixed at the proper orientation for the central wavelength of interest and the laser light source is scanned in wavelength; the output of the detector is recorded and displayed. For a monochromator the same result would be achieved if a monochromatic light source is introduced into the system and the grating rotated.

The bandpass is then defined as the Full–Width–at–Half–Maximum (FWHM) of the trace assuming monochromatic light. Any spectral structure may be considered to be the sum of an infinity of single monochromatic lines at different wavelengths.

The shape of the instrumental line profile is a function of various parameters:

i) the width of the entrance slit

ii) the width of the exit slit or of one pixel in the case of a multichannel detector

iii) diffraction and aberrations

In practice the FWHM of the spectral line is determined by the convolution of the various causes of line broadening including resolution (aberration and diffraction), influence of slits and the natural line width.

Assuming a gaussian profile for the line, FWHM is given by the following relationship:

$$FWHM = \sqrt{\Delta\lambda_{slits}^2 + \Delta\lambda_{resolution}^2 + \Delta\lambda_{line}^2} \tag{11}$$

In general, most spectrometers are not routinely used at the limit of their resolution so the influence of the slits may dominate the line profile.

3. Simulation program

3.1 The listing of CT.f

```
*     ****************************************************
*     *****    OPTICAL and SPECTROSCOPIC PARAMETERS    *****
*     *****        for a GRATING MONOCHROMATOR         *****
*     *****         in CZERNY-TURNER MOUNTING          *****
*     ****************************************************
*     *****                     by                     *****
*     *****               ALPAR SIMON (1)              *****
*     *****     EUGEN DARVASI (2) and ZSOLT VISKI (2)  *****
*     *****                                            *****
*     *****        BABES – BOLYAI UNIVERSITY           *****
*     *****        CLUJ – NAPOCA, ROMANIA              *****
*     *****        1) FACULTY OF PHYSICS               *****
*     *****           str. M. Kogalniceanu 1           *****
*     *****        2) FACULTY OF CHEMISTRY             *****
*     *****           str. Arany J. 11                 *****
*     ****************************************************
*
      PROGRAM Czerny_Turner
*
      DOUBLE PRECISION FOCAL, HEIGHT, PI, RADIAN, Y
      INTEGER G, WIDTH, ORDER, X
      REAL ALPHA, I, R, LD, AD, RLD, WS, CB, SLIT
      REAL ABER, GRES, DRES, IRES, FW, LAMBDA, RADIUS
      PI=DBLE(ACOS(-1.))
      RADIAN=PI/180.
*
      OPEN(1,FILE='Czerny_Turner.dat')
*
      WRITE(*, *)'Please input for your diffraction grating:'
      WRITE(*, *)'Groove density [grooves/mm]='
      READ(*, *) G
      WRITE(*, *)'Width [in mm]='
```

```
      READ(*, *) WIDTH
      WRITE(*, *)'Please input for your monochromator:'
      WRITE(*, *)'The working order'
      READ(*, *) ORDER
      WRITE(*, *)'Focal length [in m]='
      READ(*, *) FOCAL
      WRITE(*, *)'Slit height [in mm]='
      READ(*, *) HEIGHT
      WRITE(*, *) 'Is your slit curved? YES=1 and ENTER. NO=2
and ENTER'
      READ(*, *) X
      IF(X .EQ. 1) GOTO 1
      WRITE(*, *) 'Slit width [in microns]='
      READ(*, *) SLIT
      GO TO 2
*
 1    WRITE(*, *) 'Slit radius [in m]='
      READ(*, *) RADIUS
      CB=SQRT(1-HEIGHT*1E-03/(2*RADIUS)*HEIGHT*1E-03/(2*RADIUS))
      SLIT=(RADIUS*(1-CB)*1E+06)
 2    WRITE(*, *)'Input the starting wavelength'
      WRITE(*, *)'SW ='
      READ(*, *) LAMBDA
      WRITE(*, *)'Input the final wavelength '
      WRITE(*, *)'FW ='
      READ(*, *) FW
      WRITE(*, *)'Input wavelength step'
      WRITE(*, *)'WS ='
      READ(*, *) WS
*
      ALPHA=4
      ALPHA=ALPHA*RADIAN
*
      WRITE(1,*)'THE SLIT WIDTH IS [microns] =', SLIT
      WRITE(*,*)'THE SLIT WIDTH IS [microns] =', SLIT
*
     WRITE(1,*)LAMBDA, I, R, AD, LD, RLD, TR, DRES, GRES, SBW, IRES
 30   LAMBDA=LAMBDA+WS
      D=1./G
      S=(LAMBDA*G*1E-06)/(2*COS(ALPHA))
*
      I=(ATAN(S/SQRT(1-S*S))-ALPHA)/RADIAN
      R=I+(ALPHA+ALPHA)/RADIAN
*
      TR=ORDER*WIDTH*G
*
      AD=ORDER*G*1E-06/(COS(R*RADIAN))
```

```
      LD=ORDER*G*FOCAL*1E-03/(COS(R*RADIAN))
      RLD=1./LD
*
      DRES=(LAMBDA/TR)*1000
      ABER=LAMBDA*(1-FOCAL/SQRT(FOCAL*FOCAL+(HEIGHT*HEIGHT*1E-06)/4))
      ABER=ABER*1000
      GRES=(RLD*SLIT)
      SBW=ABER+GRES
      IRES=SQRT(GRES*GRES+DRES*DRES+ABER*ABER)
      WRITE(1,*)LAMBDA, I, R, AD, LD, RLD, TR, DRES, GRES, SBW, IRES
      WRITE(*,*)LAMBDA, I, R, AD, LD, RLD, TR, DRES, GRES, SBW, IRES
      IF(LAMBDA .LT. FW) GOTO 30
      END
```

3.2 Description of the simulation software

The program presented in this paper (CT.f) can be used to compute the optical and spectroscopic parameters of a plane grating based Czerny-Turner type monochromator. It is written in FORTRAN 77 and has been compiled with the G77 compiler (Free Software Foundation) on a compatible personal computer. For Win32 (Windows98/NT) the compiling package is available from Internet site http://www.geocities.com/Athens/Olympus/5564.

All the data computed by this program will be saved on disc, in a file named Czerny_Turner.dat.

In the first step, the program reads the basic data corresponding to the monochromator or some of its components: groove density (G, expressed in grooves/mm); width of the diffraction grating (WIDTH, in mm); takeoff angle of the grating (ALPHA, in degrees); the monochromator's focal length (FOCAL, in m); slit height (HEIGHT, in mm) and the working order (integer, unitless). Then, the user is questioned about the exit slit: if the slit is a normal one (paralell, not curved) the program reads the slit width (SLIT, in microns). If the slit is curved, it reads the curving radius (RADIUS, in m) and computes the real slit width.

Second step consist in the reading of the working wavelength interval, from the starting wavelength (SW) to the final wavelength (FW) with wavelength steps (WS) introduced by the user.

These step are depicted in Fig.3.

The incidance and diffraction angles are computed using the following formulas:

$$\hat{i} = arctg\left(\frac{\sin\hat{i}}{\cos\hat{i}}\right), \text{ where } \sin\hat{i} = \frac{\lambda}{2d\cos\hat{\alpha}} \text{ and } \hat{r} = \hat{i} + 2\hat{\alpha}$$

Using (Eq.8) the theoretical resolution is computed, than the dispersions: the angular (Eq.2), the linear (Eq.4) and the reciprocal linear one (Eq.5).

In the third part of the program the different contributions to the spectral line broadening are computed: DRES (diffraction limited resolution, in pm) using (Eq.12); ABER (broadening due to aberrations, in pm) using (Eq.13) and GRES (geometrical resolution or broadenind due to the slit, in pm) using (Eq.14).

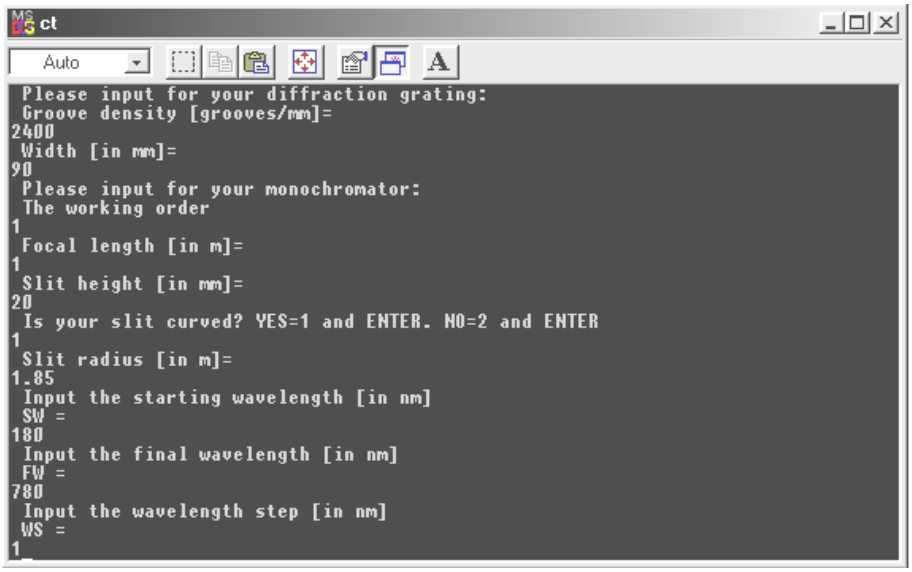

Fig.3 – The user / software dialog – box

$$DRES = \frac{\lambda}{TR} \tag{12}$$

$$ABER = \lambda\left[1 - \frac{F}{\sqrt{F^2 - h^2/4}}\right] \tag{13}$$

where F is the focal length of the monochromator and h is the height of the slit.

$$GRES = RLD \cdot SLIT \tag{14}$$

The instrumental resolution is computed using the well known relation:

$$IRES = \sqrt{GRES^2 + ABER^2 + DRES^2} \tag{15}$$

Finally, the computed data, which will be written in the saving file (Czerny_Turner.dat) are chosen. This part of the program may be easily adapted and modified to meet and resolve the needs of the user.

The results of the simulation are presented in Fig.4a–c. The name of the file was modified to depict the type of the results, namely: "angles.dat" (Fig.4a) will contain data about the incidence– and diffraction angles, "dispersions.dat" (Fig.4b) data about angular–, linear– and reciprocal linear dispersions and finally, "broadening.dat" (Fig.4c) the spectral line broadenings.

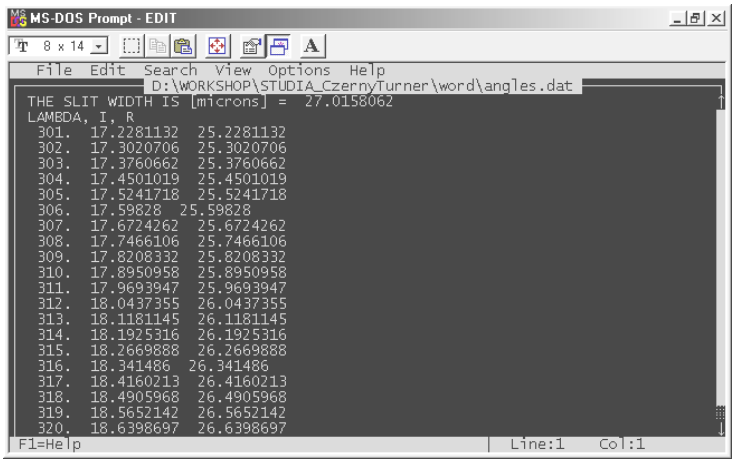

(a)

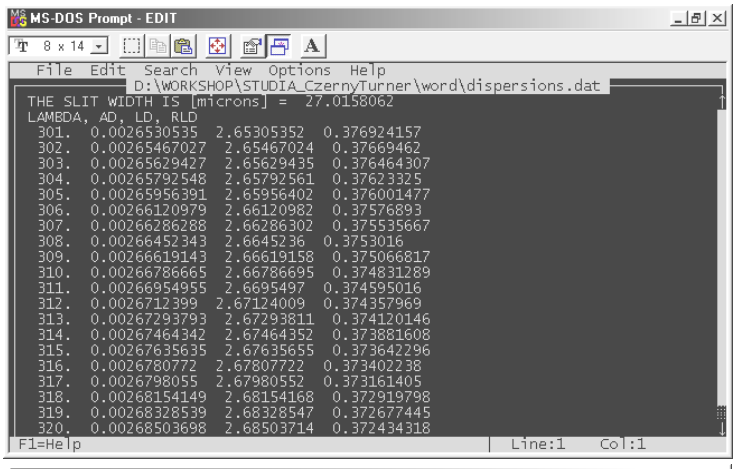

(b)

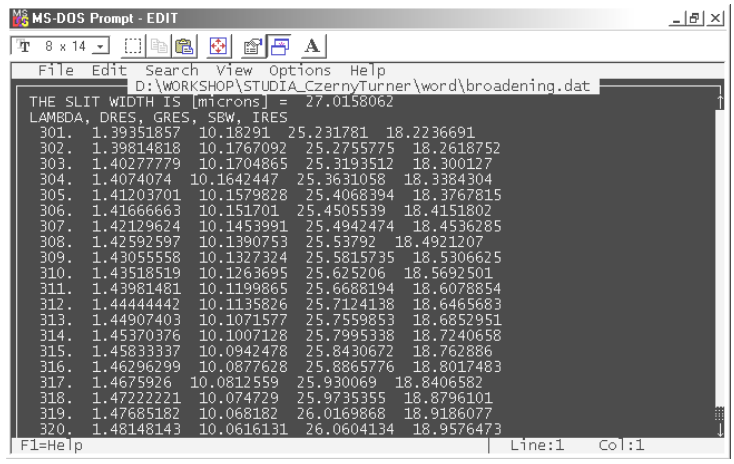

(c)

Fig.4 – The results of the computer simulation

4. Experimental

In this part of the paper some of the results of the computer simulation of the functioning of a Czerny-Turner mount monochromator will be presented. The experimental conditions of computer simulation are listed in Table 1. The influence of slit curving radius on the slit width, geometrical– and instrumental resolutions are presented in Fig.5 and Fig6.

Table 1.

Experimental condition of computer simulation

	Monochromator's focal length, F = 1 m		
	Slit height = 20 mm		
	Diffraction grating width = 90 mm		
	Working order: 1		
*	Wavelength region: 180 – 780 nm	**	Wavelength region: 399 – 401 nm
	Wavelength step: 1 nm		Wavelength step: 1 nm
	Groove density, G = 300, 600, 1200, 1800 and 2400 grooves/mm		
	Slit curving radius, R = 0.5, 1.0, 1.5, 1.85, 2.0, 2.5 and 3.0 m		

* when simulation is performed as funtion of wavelength
** when simulation is performed as function of other parameters, at a constant wavelength

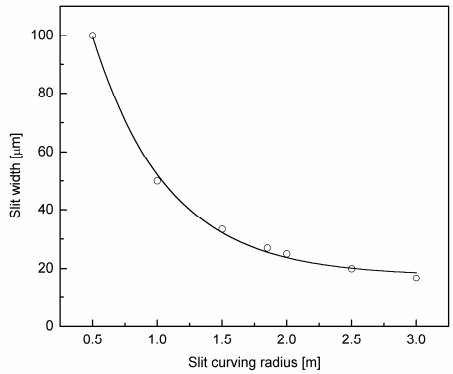

Fig.5 – Influence of slit curving radius on the slit width

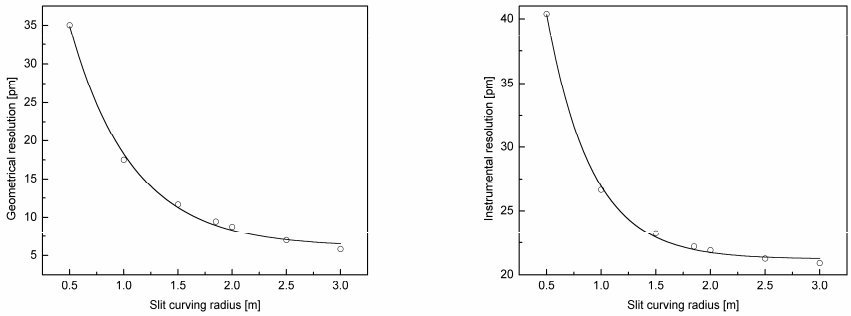

(a) (b)

Fig.6 – Influence of slit curving radius on the geometrical– (a) and instrumental resolutions (b)

The effect of changes in groove density on angles and resolutions is presented in Fig.7a – d.

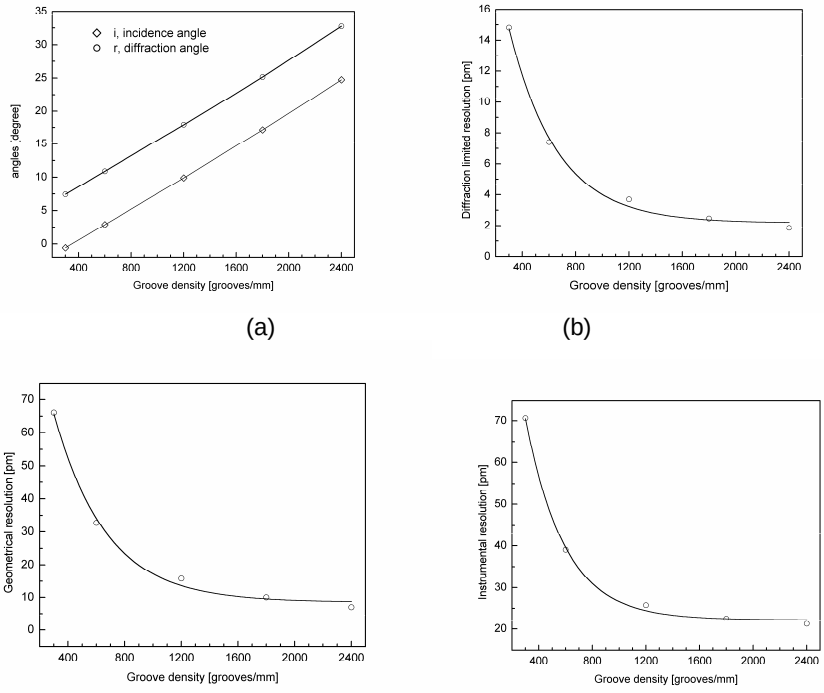

Fig.7 – Influence of groove density on incidence– and diffraction angles (a) and resolutions: diffraction limited (b), geometrical (c) and instrumental (d).

The broadening due to abberations as function of wavelength is presented in Fig.8.

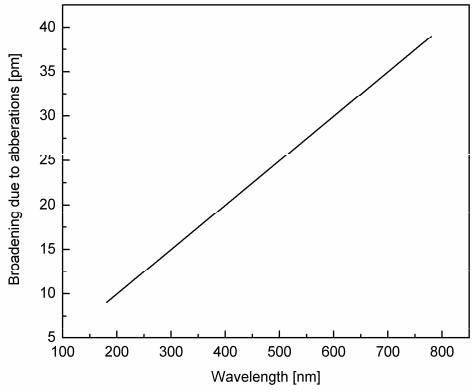

Fig.8 – Broadening due to abberations as function of wavelength

The same simulation program was used to perform the computation of spectral bandwith of a Czerny – Turner mount monochromator used to record the OH emission spectra in the UV region. This bandwith was necessary to obtain a synthetic OH spectra via simOH.f [4].

The characteristics of these monochromator (property of Research Institute for Analytical Instrumentation, Cluj, ROMANIA) are presented in Table 2. The experimental– and the computer simulated spectra were presented elsewhere [5].

5. Conclusions

This paper has presented a way to compute the optical and spectroscopic parameters of a Czerny-Turner type monochromator. The aim of this work was to present a basic method to compute those parameters, the optimization of the computation code was fully neglected. The program may be transformed in the near future, to produce visual result directly on the computer screen of the user.

In our opinion, this program could be a very useful tool in taking decisions about the properties of a future monochromator which could be purchesed by the users Lab or it could be a useful educational tool. It was shown that it is also very useful in computing some instrumental parameters necessary to obtain synthetic spectra.

REFERENCES

1. Clive C. Page: Professional Programmer's Guide to FORTRAN77, Pitman 1988
2. Ch. Palmer: Diffration Grating Handbook, Richardson Grating Laboratory 2000
3. E. G. Loewen and E. Popov: Diffraction Gratings and Applications, Marcel Dekker 1997
4. Ch. de Izarra, *Int. J. of Modern Phys. C* **11**, no.5, 987, 2000
5. Simon, S. D. Anghel, S. Simon, T. Frentiu, E. Czirjak and E. A. Cordos: Studia PHYSICA, 1 / 2002 – accepted for publication

STUDIA UNIVERSITATIS BABEŞ-BOLYAI, PHYSICA, XLIX, 1, 2004

ISOTOPIC COMPOSITION OF PLANT CARBON CORRELATES WITH WATER-USE EFFICIENCY

STELA CUNA[1], GABRIELA BALAS[1], ONUC COZAR[2]

[1] National Institute of Research and Development for Isotopic and Molecular Technology, Cluj-Napoca
[2] Babes-Bolyai University, Dept. of Physics, Cluj-Napoca

ABSTRACT. Agricultural productivity is limited by water availability. One solution to this problem is to select and breed plants requiring less water for growth, i.e. to increase water-use efficiency (WUE). We study the use of carbon isotope analysis from plant material as a tool for investigating WUE. For that purpose we have used the theoretical models relating stable carbon isotope discrimination (Δ) from leaf of the plant and WUE. The correlation between WUE and Δ was assessed in five plants: Malus domestica, Zea mays, Robinia pseudacacia, Juglans regia and Castanea nativa. Δ was determined by the analyze of carbon isotopic composition from leaves. Carbon from plant material was converted to CO_2 by dry combustion in an excess of oxygen and then was analyzed for stable isotope ratio measurements by mass spectrometry. A negative correlation between WUE and Δ was established for these plants. It is suggested that carbon isotope analysis may be a useful tool in selection for improved water-use efficiency of some plant obtained "in vitro" by biotechnological processes.

Introduction

During photosynthetic CO_2 fixation, plants discriminate against the naturally occurring stable isotope ^{13}C. In C_3 species, fractionation of carbon in plant materials is caused by the carboxylase enzyme, RUBISCO, which discriminates against ^{13}C and by diffusion from the atmosphere to the sites of CO_2.

Carbon isotope discrimination (Δ) is defined as difference between isotopic composition of CO_2 in atmosphere and in plant [1]:

$$\Delta = \delta^{13}C_{atm} - \delta^{13}C_{plant} \qquad (1)$$

where $\delta^{13}C_{atm}$ and $\delta^{13}C_{plant}$ are the isotope composition of air and plant material respectively. Also, carbon isotope discrimination by the plant can be described by the equation [2]:

$$\Delta = a + (b - a) \cdot p_i / p_a \qquad (2)$$

where a is the fractionation occuring during diffusion in air (a=4.4‰); b is the net fractionation caused by carboxylation (b=30‰); p_a and p_i are the ambient and intercellular partial pressures of CO_2.

WUE is defined as the ratio of dry matter production to water use. WUE is a relevant parameter that can determine the crop yield especially when water resources are limited [4] because according to Passioura [7] crop yield (Y) is given by:

$$Y=WUE \times Ex\ HI \tag{3}$$

where E is the water transpired, and HI is the harvest index (the ratio of economical production to total biomass produced).

Water-use efficiency of a plant (WUE) is expressed by the equation [3]:

$$WUE = \frac{p_a\left(1-\frac{p_i}{p_a}\right)}{1.6\cdot\Delta l} \tag{4}$$

In this relation Δl is the gradient that appear between intercellular and atmospheric vapor pressures and can vary between Δl=10mbar in winter and Δl=20mbar in spring. The factor 1.6 is the ratio of the diffusivities of water vapor of CO_2 in air.We can observe that Δ is correlated with WUE by intermediating of p_i/p_a.

Materials and methods

For WUE determination we have used the leaves of four plant species: *Malus domestica, Robinia pseudoacacia, Julans regia,* and *Castanea sativa.*

The steps for WUE measurements were: sample collection and preparation, sample combustion, isotopic analysis of ^{13}C from CO_2 resulted from combustion, and data interpretation.

Leaves have collected at the same time of the day because the diurnal changes in starch and sugar contents can affect carbon isotope ratio. To further minimize sample variation in population-level studies, samples were collected from the same canopy position. There can be $\delta^{13}C_{air}$ gradients that could potentially confound interpretation of plant isotopic values, especially in dense canopies. After harvesting, the leaves were dried immediately at a 70^0C to avoid loss of organic materials. Samples were stored at room temperature after drying for later determination of their isotopic composition.

The technique utilized to measure the isotopic composition of the leaves was isotope ratio mass spectrometry. The instrument was a mass spectrometer equipped with a double inlet system and double collector, type Atlas 86 designed by Varian MAT. The isotopic analysis by mass spectrometry are made on CO_2, so the carbon from organic samples must be extracted as CO_2.

Carbon extraction as CO_2 has made by dry combustion of th leaves in an excess of oxygen in sealed quartz tubes. The oxygen source is CuO. The sample and CuO are placed in quartz tubes, than the quartz tubes are attached at a

vacuum line, evacuated and sealed. For combustion, we have used a furnace with programmable temperature. The temperature for combustion was 850^0C. After combustion CO_2 from the leaves was separated from the other combustion products (N_2, H_2O, O_2) by cryogenic distillation. CO_2 purified was introduced in mass spectrometer and the $\delta^{13}C$ values was measured.

For a better precision of measurements, we have used the method of double collectors [5], that means that both ions beams $^{12}CO_2^+$, $^{13}CO_2^+$ are collected simultaneously by the collector. The stable isotope abundance is expressed relative to a standard:

$$\delta = \left[\frac{R_{sample} - R_{s\tan dard}}{R_{s\tan dard}} \right] \cdot 10^3 ‰ , \qquad (5)$$

where *R* is the molar ratio of the heavy to light isotopes of the sample and standard gas ($R=^{13}C/^{12}C$). By international convention $\delta^{13}C$ values are always expressed relative to a calcium carbonate standard known as PDB. This standard is a limestone fossil of *Belemnitella americana* from Cretaceous Pee Dee formation in South Carolina.The precision of measurements was ±0.5‰.

Results and discussion

The results of the measurements are presented in Table 1.

Table 1

The WUE values for the studied plants

No	Sample	$\delta^{13}C_{plant\ vs\ PDB}$ [‰]	Δ [‰]	p_i / p_a	WUE [mmolC/molH_2O]	Photo-synthetic pathway
1.	Malus domestica	-26.86	18.99	0.57	4.43	C_3
2.	Castanea sativa	-27.06	19.25	0.58	4.46	C_3
3.	Robinia pseudoacacia	-26.01	17.97	0.53	4.99	C_3
4.	Julans regia	-26.01	17.97	0.53	4.99	C_3

The p_i/p_a ratio was estimated from equation (2) by measuring the carbon isotope composition of plant material and using the values a=4.4, b=30, $\delta^{13}C_{atm}$=-7.8‰, and p_a=340 ppm from literature [4], [5].

We have determinate the water-use efficiency from equation (4) knowing p_i/p_a for each plant. All plants have the $\delta^{13}C$ values in the range of the C_3 plants where fractionation of carbon is caused by the carboxylase enzyme RUBISCO.

The carbon isotope discrimination, Δ, is approximately the same for all plant leaves that means that the four studied plants had the same source of CO_2 because photosynthetic rate is linearly related to ambient CO_2 concentration. These values reflect the fact that we have collected the samples at the same time of the day. There is a little difference in Δ values between *Juglans regia* (nut tree) and *Castanea sativa* (chestnut tree). The lower Δ values in *Juglans regia* than in *Castanea sativa* indicate a lower overall intercellular CO_2 concentration, and a lower stomatal opening.

The relationship between isotopic discrimination Δ, and water use-efficiency (WUE) is presented in Fig. 1.

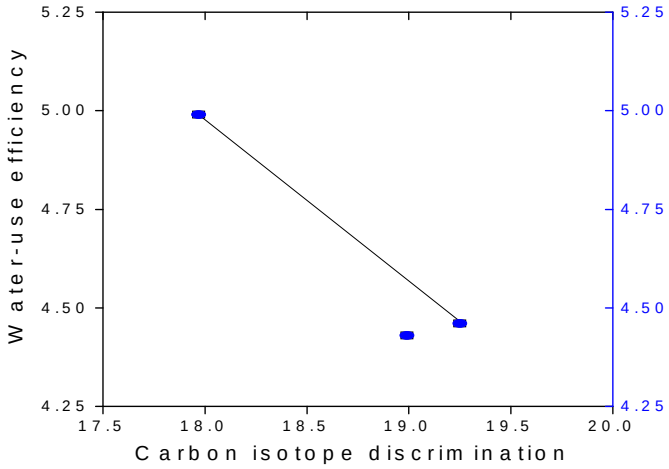

Figure 1. Relationship between carbon isotope discrimination (Δ) and the water use-efficiency (WUE) in the leaves of plants studied

In Fig. 1 there is a negative correlation between Δ and WUE: the smaller is discrimination, the better is water-use efficiency. This fact is in concordance with Farquhar theory [2]: carbon isotope discrimination will be very small in those C3 plants that have the greater water-use efficiency.

This correlation is evident when water is limiting. During plant growth the losses of carbon and water are more complex. For example, a part from water is loosed independent of CO_2 consumption because the stomata during the night are not completely closed and than little quantities of water can attach on stomata.

p_i/p_a ratio is approximately the same for all plant leaves. That means that studied plants have a similar physiology. Also the p_i/p_a ratio reflects the environmental influence of stomata behavior. The p_i values are approximately the same, so the stomatal opening is approximately the same, a little exception being the case of *Juglans regia* and *Castanea sativa*. The p_i/p_a value represents a holistic, integrated measure of the multitude of factors that influence both CO_2 uptake and water loss in plants.

On relationship between Δ, p_i/p_a and WUE, on can say that, at least under water-limiting conditions for plant, the genotypes with smaller Δ have a better WUE and a better yield. The measurements confirm the relationship between Δ and WUE, and can be used in the future to study the yield increase of plant species in stress conditions (dryness) following discrimination Δ and the relation between Δ and WUE.

The results obtained are in good agreement with literature.

Conclusions

This paper presents a method to analyze carbon isotope composition in leaf. This method is based on carbon extraction as CO_2 by dry combustion in an excess of oxygen of the leaves, and on determination of isotopic composition of carbon from CO_2 by mass spectrometry with double collectors. Further, carbon isotope discrimination in plants is use to determine p_i/ p_a (the intercellular partial pressures of CO_2/ ambient partial pressures of CO_2), the water use efficiency (WUE), and to understand photosynthetic process of the plant. Knowledge of parameter WUE is useful to improve the plants genotypes under water-limiting conditions, and to study the yield increase of plant species in stress conditions (dryness).

REFERENCES

1. Brugnoli E. and Farquhar G.D., *Photosynthetic fractionation of carbon isotopes*, in: "Photosynthesis: physiology and metabolism", Leegood RC, Sharkey and S von Caemmerer (eds.), Kluwer Academic Publishers, The Netherlands, 2000, pp. 399-434
2. Farquhar G.D., O'Leary M.H. and Berry J.A., *On the relationship between carbon isotope discrimination and the intercellular carbon dioxide concentration in leaves*, Aust. J. Plant Physiol., 9, 1982, pp. 121-137,
3. Farquhar G.D and Richards R.A., *Isotopic composition of plant carbon correlates with WUE of wheat genotypes*, Aust. J. Plant Physiol., 11, 1984, pp. 539-552
4. Brugnoli E., Scartazza A., Lauteri M., Monteverdi M.C. and Maguas C., *Carbon isotope discrimination in structural and non-structural carbohydrates in relation to productivity and adaptation to unfavorable conditions*, in Stable isotopes integration of biological, ecological and geochemical processes, ed. H. Griffich, Bios Scientific Publishers Limitd, U.K., 1998, pp. 133-144
5. Carbon Isotope Techniques, ed. David C. Coleman and Brian Fry, Academic Press Inc., San Diego, 1991, pp. 187-200
6. Ehleringer J.R, Cerling T.E., *Atmospheric CO_2 and the ratio of intercellular to ambient CO_2 concentration in plants*, Tree Physiology 15, 1995, pp. 105-111
7. Passioura J.B., *Resistance to drought and salinity: avenues for improvement,* Aust. J. Plant Physiol., 13, 1986, pp. 191-201

STUDIA UNIVERSITATIS BABEŞ-BOLYAI, PHYSICA, XLIX, 1, 2004

RAMAN STRUCTURAL INVESTIGATION OF IRON DOPED B_2O_3-K_2O GLASS MATRICES

D. MANIU

Faculty of Physics, Babes-Bolyai University,
Kogalniceanu 1, 3400 Cluj-Napoca, Romania

ABSTRACT. The influence of Fe_2O_3 content on the structure of $3B_2O_3 \cdot K_2O$ glass was investigated using Raman spectroscopy. At low content of iron ions the Raman spectra do not reveal any structural changes. Addition of iron oxide causes the increases of the number of non-bridging oxygen, the glass structure becomes more randomized and "loose" BO_4^- tetrahedra appear. A small number of chain-type metaborate and pyroborate groups are also present in this kind of glass.

Iron ions act as network modifier in these glasses.

Introduction

Raman spectroscopy is an appropriate tool for investigating the structure of glasses. Raman spectra of crystalline borates have been used as a basis for the qualitative identification of glass-forming structural units in alkali borate glasses [1-9]. The introduction of the transition metal in glasses leads to the change of the glass structure, the metal oxide is acting as a modifier [10-14]. A complete understanding of the glasses structure is essential in any search for new materials to be considered for use in the fiber-optics communication fields.

In this article we show and discuss the Raman spectra of $xFe_2O_3 \cdot (1-x)[3B_2O_3 \cdot K_2O]$ glasses with $0 \le x \le 0.2$.

Experimental

The glasses were obtained by mixing H_3BO_3, K_2CO_3 and Fe_2O_3 in suitable proportions and by melting these admixtures in sintered corundum crucibles at T=1150 °C for 30 min. The samples were obtained by pouring the melts in stainless steel forms. These glasses are fairly hygroscope and, thus, special care has to be taken to protect them from hydrolysis. For the Raman spectra the 514.5 nm line of an Ar-ion laser (Spectra-Physics Model 2016) was used. The laser beam was carried through a filter prism (Anaspek) to avoid the plasma lines and then was focused on the sample with an Olympus microscope objective (Olympus ULDW 80, NA 0.75). The back-scattered light was collected by the same objective. After the reflection on a beam-splitter the light was focused with a Fuji camera objective on the entrance slit of the detection system. A Dilor-XY Raman triple monochromator with a Peltier-cooled, intensified diode array with 1024 diodes is employed as the light detection system. The back-scattering configuration, of the micro Raman set-up, allows the observation of the sample surface before light exposure. The laser power was 400 mW. The measurements were carried out at room temperature.

The spectral data are processed using Dilor hardware and specially developed software. The spectra were recorded with a resolution of 2 cm^{-1} and the spectral data were analyzed with XMGR software.

Results

Raman spectra of $xFe_2O_3 \cdot (1-x)[3B_2O_3 \cdot K_2O]$ glasses with various content of iron oxide ($0 \leq x \leq 0.2$) are shown in Fig. 1. The following bands are present in these spectra: 420 cm^{-1}, 475 cm^{-1}, 770 cm^{-1}, 800 cm^{-1}, 930 cm^{-1}, 1230 cm^{-1}, 1330 cm^{-1} and 1450 cm^{-1}.

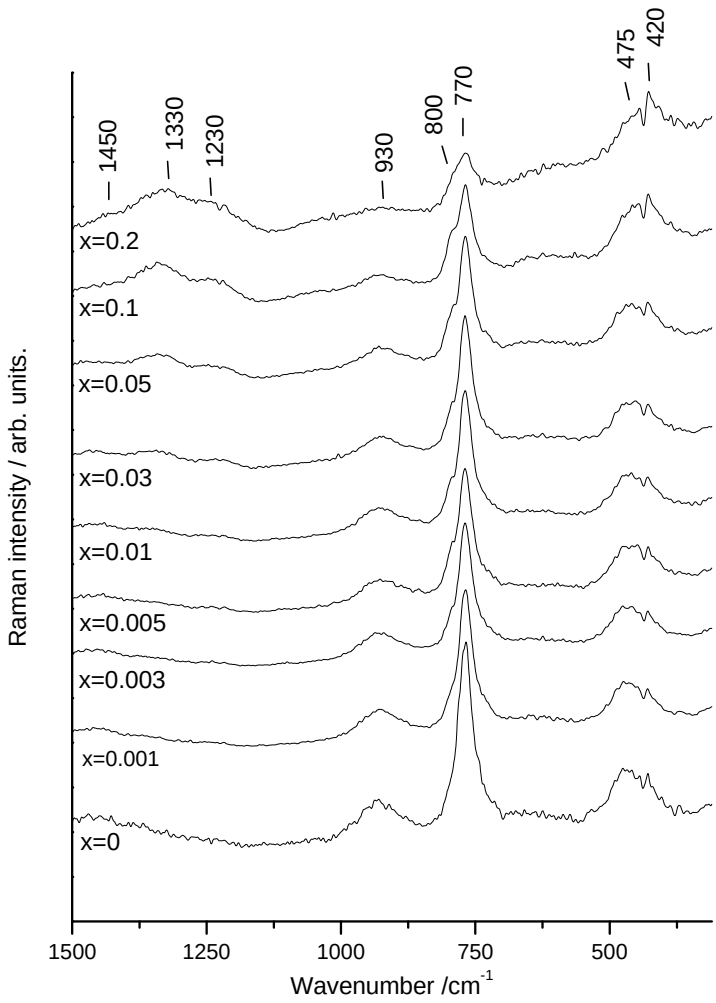

Fig. 1. Raman spectra of $xFe_2O_3 \cdot (1-x)[3B_2O_3 \cdot K_2O]$ glasses with $0 \leq x \leq 0.2$;

For all spectra, the intensity of the 770 cm^{-1} band is higher than that of the 800 cm^{-1} band. The 770 cm^{-1} band is dominant for the glasses with $x \leq 0.1$. High content of iron oxide determines an intensity increase of the bands centered at 420 cm^{-1} and 470 cm^{-1}. For x=0.2 the bands centered at 420 cm^{-1} and 470 cm^{-1} become stronger than that at 770 cm^{-1}.

The Raman bands at 930 cm^{-1}, 1230 cm^{-1} and 1450 cm^{-1} can be observed in all spectra. At high content of iron oxide a peak centered at 1330 cm^{-1} appears.

Discussion

The Raman spectrum of the vitreous B_2O_3 is dominated by an intense and narrow band at ~806 cm^{-1} assigned to the boroxol ring oxygen breathing, involving a very small amount of boron motion (boron atom is three-coordinate) [1]. With the addition of alkali oxide, a strong band at ~770 cm^{-1} appears and the band at ~806 cm^{-1} is shifted to the lower wavenumber at about 800 cm^{-1} [2]. Bril et al. [3] assigned the Raman band at ~770 cm^{-1} to the symmetric breathing vibration of six-member rings with one BO_4 tetrahedron (i.e., triborate, tetraborate or pentaborate) and the band at a lower wavenumber (~755 cm^{-1}) was assigned to the symmetric breathing vibration of six-member rings with two BO_4 tetrahedra (i.e., diborate, ditriborate, or dipentaborate) [3]. Addition of K_2O to vitreous B_2O_3 determines a change of the boron coordinate number from 3 to 4. (In a previous paper [10] we presented a list of borate groups found in borate glasses.)

In all spectra the intensity of the 770 cm^{-1} band is stronger than that at 800 cm^{-1}. As a result of no appearance of the 755 cm^{-1} and a constant spectral position, within the limits of experimental error, of the 770 cm^{-1} band we conclude that in our glasses the six member borate rings contain only one BO_4 thetrahedron.

Crystalline α and β K_2O-$5B_2O_3$, which contain only pentaborate units give Raman bands at ~765 and ~885 cm^{-1}, and at ~785 and ~930 cm^{-1}, respectively [5]. Crystalline Na_2O-$4B_2O_3$ (consisting of tetraborate groups) and crystalline Cs_2O-$3B_2O_3$ (consisting of triborate groups) have only a very weak response in the ~930 cm^{-1} region [5]. Thus, the presence of the band centered at 770 cm^{-1} and the band centered at 930 cm^{-1} can be taken as a clear evidence for the presence of pentaborate groups in the studied glasses.

The iron glasses spectra with $x \leq 0.01$ (Fig. 1) do not reveal any important changes. Therefore, we can say that at very low concentration, iron does not modify the structure of the studied glasses. The increase of iron concentration determines the rise of the 420 cm^{-1} and 475 cm^{-1} intensity bands compared with the intensity of the band centered at 770 cm^{-1}. At x = 0.2 the bands at 420 cm^{-1} and 475 cm^{-1} become dominant. The intensity of the 930 cm^{-1} and 1450 cm^{-1} bands decrease when iron concentration rises, and the shoulder at 1230 cm^{-1} increases. For $x \geq 0.05$ a band centered at 1330 cm^{-1} appears.

The ~475 cm^{-1} band is assigned to a ring angle bending (B-O-B) of borate units [6], which is observed at ~470 cm^{-1} for pure B_2O_3 [7]. The band at ~420 cm^{-1} is assigned to the asymmetric vibration of "loose" BO_4 thetrahedra (i.e. thetrahedra connecting various segments without participating in specific borate arrangements) [8]. The presence of a very large band at ~1450 cm^{-1} in the Raman spectra indicates the presence of chain-type metaborate groups [8]. The anti-symmetric band at

~1230 cm^{-1}, indicates the formation of pyroborate groups $\left(B_2O_5^{4-}\right)$ [5] and the ~1330 cm^{-1} band was assigned by Meera [2] to boron-oxygen stretch which involve non-bridging oxygen ions.

Thus, the addition of iron oxide in studied glasses determines the decreasing of the boroxol and pentaborate groups and the formation of pyroborate groups and "loose" BO_4 thetrahedra. Therefore, the number of non-bridging oxygen ions increases, and the glass structure becomes more randomized.

Conclusions

The increases of iron oxide content in studied glasses determines the decreasing of the boroxol and pentaborate groups and the formation of pyroborate groups and "loose" BO_4 thetrahedra. The number of non-bridging oxygen ions increases while iron concentration rise, and the glass structure becomes more randomized. In studied glasses a small number of chain-type metaborate and pyroborate groups are also present. Therefore, we conclude that, in the studied glasses, the iron ions act as a network modifier at medium and high concentration.

Acknowledgements: D. M. thanks Professor Dr. W. Kiefer for access to the laboratory instrumentation.

REFERENCES

1. B. P. Dwivedi, M. H. Rahman, Y. Kumar and B. N. Knanna, J. Phys. Chem. Solids, **54** (1993), 621.
2. B. N. Meera, A. K. Sood, N. Chandrabhas and J. Ramakrishna, J. Non-Cryst. Solids, **126** (1990), 224.
3. T. W. Bril, Philips Res. Rep. Suppl., **2** (1976), 117.
4. F. L. Galneer, Solid State Commun., **44** (1982), 1037.
5. W. L. Konijnendijk, Philips Res. Rep. Suppl., **1** (1975), 224.
6. W. L. Konijnendijk and J. M. Stevels, Mater. Sci. Res., **12** (1977), 259.
7. J. Krong-Moe, Phys. Chem. Glasses, **61** (1965), 46.
8. E. I. Kamitsos and G. D. Chyssikos, J. Mol. Struct., **247** (1991), 1.
9. E. I. Kamitsos, M. A. Karakassides and G. D. Chyssikos, Phys. Chem. Glasses, **30** (1989), 229.
10. D. Maniu, I. Ardelean and T. Iliescu, Studia Univ Babes-Bolyai, Physica, **2** (1994), 13.
11. T. Iliescu, S. Simon, D. Maniu and I. Ardelean, J. Mol. Struct., **294** (1992), 201.
12. T. Iliescu, I. Ardelean, and S. Simon, *Solid St. Commun.* **90** (1994), 507.
13. D. Maniu, I. Ardelean, T. Iliescu, S. Cinta, V. Nigel and W. Kiefer, J. Mol. Struct., **480-481** (1999), 657.
14. D. Maniu, I. Ardelean, T. Iliescu and C. Pantea, J. Mat. Sci. Lett., **16** (1997), 19.

STUDIA UNIVERSITATIS BABEŞ-BOLYAI, PHYSICA, XLIX, 1, 2004

DISTRIBUTION FUNCTION OF EXTENSIVE PARAMETERS OF A MESOSCOPIC SUBSYSTEM

LÁZÁR I. ZSOLT*, MOLNÁR ETELE **

**Physics Department, Babeş-Bolyai University, Str. M. Kogălniceanu Nr.1, 400084 Cluj-Napoca, Romania (zlazar@phys.ubbcluj.ro)*
***Section for Theoretical Nuclear Physics, Department of Physics, University of Bergen, Allegaten 55, 5007 Bergen, Norway (etelem@fi.uib.no)*

ABSTRACT. Motivated by the need for a thorough theoretical foundation of numerical fluctuating fluid dynamics the distribution of extensive quantities of a subsystem as part of a larger system is studied. The established general expression for the distribution is applied to several special cases giving contour to a method allowing the estimation of high momenta of the distribution in the case of both a finite system and finite subsystem. The implications of the results on numerical fluid dynamics with numerical grid cell as subsystem are discussed.

I. Introduction

There is a growing interest in the study of mesoscopic systems. The number of degrees of freedom in such systems are too small for macroscopic descriptions to be applicable while it is too large for microscopic methods to be feasible. The hot and dense nuclear matter formed in a high energy nuclear collision [1] or the scorching centre of a sonoluminescing bubble [2-4] are examples for mesoscopic systems. The common characteristic in the above mentioned two cases is that fluid dynamics can be succesfully used for describing their evolution. However, considering the low number of degrees of freedom, ignoring fluctuations is an oversimplification of the problem. It is common technique in hydrodynamical description of heavy-ion collisions that the size of numerical grid cells is such that on the average they contain less than a particle. The fluctuating hydrodynamics proposed by Landau and Lifsitz [5] is formulated similarly to the Brownian motion of Langevin turning the usual fluid dynamical equations into stochastic equations of motion by adding an extra fluctuating force density term, $\boldsymbol{f}'$ to the momentum conservation equation.

$$\frac{\partial \boldsymbol{M}}{\partial t} = -\nabla(\boldsymbol{M}\boldsymbol{v}) - \nabla P + \eta\nabla^2\boldsymbol{v} + \left(\zeta + \frac{1}{3}\eta\right)\nabla(\nabla\boldsymbol{v}) + \boldsymbol{f}' \qquad (1)$$

where $\boldsymbol{M} = \rho\boldsymbol{v}$ is the momentum density and η, ζ are the shear viscosity, bulk viscosity respectively. There have been performed fluctuating fluid dynamical calculations [6-10] using (1). Essentially, these methods consist in solving the hidrodynamical equations with an additional Langevin term which accounts for the fluctuating phenomena that accompany the fluid dynamics.

Our goal is to gain a better insight into the fluctuations that occur in a fluid, beyond the commonly used first and second moments of the distributions. We shall try to find a way of determining the actual distribution functions. In order to usefully assist Eulerian numerical methods we need to provide information regarding the events occuring at the level of a numerical cell viewed as a finite sized subsystem of the fluid.

In present work we shall establish the general expressions for the distribution function, $f(A)$, of an extensive quantity, A, such as energy or momentum, characterizing a system embedded into another one.We shall refer to the former as 'subsystem'. The obtained general formulae will be applied for finding the energy, momentum and angular momentum distribution functions of the subsystem for an ideal gas in equilibrium.

II. General Consideration

Let us consider a classical system of N particles in a state described by the manyparticle distribution function $F(\boldsymbol{x}_1,...,\boldsymbol{x}_N)$, where $\boldsymbol{x}_i \equiv (\boldsymbol{r}_i, \boldsymbol{p}_i)$ stands for the position and momentum of the ith particle. The time dependence is implicitly included. The volume of the system is denoted by W, and within this volume we define an arbitrarily shaped region, D, of size V which henceforth will be referred to as 'subsystem'.

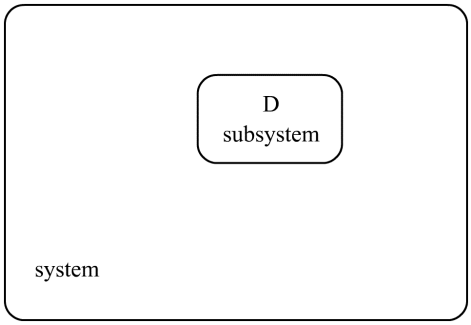

Figure 1.

Each particle carries the amount a_i of a certain extensive parameter, a, which depends on the position and momentum of the particle. Depending on the number of particles in the subsystem and of the quantity carried by these the total amount of this quantity, denoted by A, will fluctuate. In order to find out the value of A for the selected region, D, we will introduce a function, $\mu(\boldsymbol{r})$ characterizing the position of a particle, such that this function is equal to unity or zero depending on whether the particle lies inside or outside the selected region:

$$\mu(r) = \begin{cases} 1 & if \quad r \in D, \\ 0 & if \quad r \notin D. \end{cases}$$

The total value of the extensive quantity in the subsystem is

$$A(\boldsymbol{x}_1,...,\boldsymbol{x}_N)=\sum_{i=1}^{N}\mu(\boldsymbol{r}_i)a_i,$$

which value fluctuates as we take the different microstates of the ensemble characterized by a finite set of macroscopic parameters. Note that the extensive parameter, a, should be a linear functional of $F(\boldsymbol{x}_1,....,\boldsymbol{x}_N)$ such as energy or momentum but not entropy, for instance.The expression for the distribution function for these fluctuations can be written generally as

$$\equiv\left\langle \delta\left(\sum_{i=1}^{N}\mu(\boldsymbol{r}_i)a_i-A\right)\right\rangle, \tag{2}$$

where $d\Gamma\equiv d\boldsymbol{r}_1 d\boldsymbol{p}_1...d\boldsymbol{r}_N d\boldsymbol{p}_N$ is the $6N$ dimensional volume element of the phase space. In compact form eq.(2) expresses the fact that in order to find the probability of the extensive quantity, *a*, lying within some narrow interval around A, is the sum of probabilities of those microstates in the ensemble which satisfy the requirement that the accumulated contributions from each individual particle for the particular extensive parameter, should be within this interval.

Unfortunately, the rhs of (2) cannot be evaluated directly so another approach should be used. We shall rewrite it into a less compact yet more usable form. Let us denote by X the event of finding the studied extensive quantity of the subsystem in the neighborhood of A and the event of having n particles inside the volume of the subsystem by Y_n. The set $\{Y_n\}, n=0,...,N$ is a complete set of events. The probabilities, $P(X)$ and $P(Y_n)$ can be connected via the equation

$$P(X)=\sum_{n=0}^{N}P(X\cdot Y_n)=\sum_{n=0}^{N}P(X|Y_n)P(Y_n), \tag{3}$$

where $X\cdot Y_n$ denotes the logical 'and' operation between two events while $P(X|Y_n)$ represents the conditional probability of event X constrained by the occurrence of Y_n. The physical meaning of decomposition (3) is that the estimation of the searched probability is done by integrating over smaller distinct domains, (Γ_n), of the phase space, (Γ), and adding up all their contributions:

$$(\Gamma)=\bigcup_{n=0}^{N}(\Gamma_n),$$

where (Γ_n) is that region of the phase space where all points correspond to configurations with n particles residing within the subsystem, D. Consequently, our task is to evaluate the two factors on the rhs of (3) knowing that on the lhs

$$P(X) = f(A)dA. \tag{4}$$

The probability of finding n particles in the subsystem is

$$P(Y_n) \equiv P_n = \left\langle C_n(\boldsymbol{r}_1, \boldsymbol{r}_2, ..., \boldsymbol{r}_N) \right\rangle, \tag{5}$$

where the 'counter' function, $C_n(\boldsymbol{r}_1, \boldsymbol{r}_2, ..., \boldsymbol{r}_N)$, is defined as

$$C_n(\boldsymbol{r}_1, \boldsymbol{r}_2, ..., \boldsymbol{r}_N) = \binom{N}{n} \prod_{i=0}^{n} \mu(\boldsymbol{r}_i) \prod_{j=n+1}^{N} [1 - \mu(\boldsymbol{r}_j)].$$

In the subsystem, containing n particles, the probability, $P(X|Y_n)$ of finding the extensive parameter, a, in the interval $(A, A+dA)$ is

$$P(X|Y_n) = \left\langle \delta\left(\sum_{i=1}^{n} a_i - A\right) \right\rangle_n dA, \; n \neq 0 \;, \tag{6}$$

$\langle ... \rangle_n$ denoting averaging over the Γ_n region of the phase space.

For $P(X|Y_0)$ we have

$$P(X|Y_0) = \begin{cases} 1, & \text{if} \quad A \in [0, dA) \\ 0 & \text{otherwise} \end{cases}. \tag{7}$$

Substituting eqs. (4,5,6,7) into eq.(3), dividing the equation by dA and taking the limit $dA \to 0$ we find that the probability distribution is

$$f(A) = \sum_{n=0}^{N} P_n I_n \;, \tag{8}$$

where

$$I_n(A) \equiv \left\langle \delta\left(\sum_{i=1}^{n} a_i - A\right) \right\rangle_n \;, \; I_0 \equiv \delta(A) \,. \tag{9}$$

The main difference between eq. (8) and the original eq. (2) is that the form of the momentum dependent part, representing an n particle distribution function, $I_n(A)$, does not contain the $\mu(\boldsymbol{r})$ function, making the calculation feasible. Being

a distribution function, $I_n(A)$ is normalized, hence the total distribution function $f(A)$ is also normalized. $\mu(\boldsymbol{r})$ appears only in P_n, the average of the counter function in (5). However, this will not constitute a major problem in the cases treated below.

III. Equilibrium Distribution Functions

We can evaluate $I_n(A)$ in (9) by assuming that the gas is monoatomic and in thermal equilibrium with its environment at a given temperature $T = 1/k\beta$. The N-particle distribution function can be decomposed into a momentum and a position dependent part both being normalized to one:

$$F(\boldsymbol{x}_1,...,\boldsymbol{x}_N) = P(\boldsymbol{p}_1,...,\boldsymbol{p}_N)R(\boldsymbol{r}_1,...,\boldsymbol{r}_N)$$

$$= \frac{1}{Z_N^p} e^{-\frac{\beta}{2m}\sum_{i=1}^N \boldsymbol{p}_i^2} \frac{1}{Z_N^r} e^{-\beta V(\boldsymbol{r}_1,...,\boldsymbol{r}_N)},$$

where the $N-$particle momentum partition function is

$$Z_N^p = \left(\frac{\beta}{2\pi m}\right)^{\frac{3N}{2}}$$

If we assume that in eq. (9) $a_i = a_i(\boldsymbol{p}_i)$ is only a function of momentum we canintegrate out the position dependent part. It is convenient to use dimensionless variables therefore we $\boldsymbol{q}_i = \sqrt{\beta/2m}\,\boldsymbol{p}_i$

We also take advantage of the fact that the Dirac function in (9) depends only on particles with index $i = 1, n$ allowing the integration over $N-n$ particle momenta. The distribution function can be written in the dimensionless form

$$f(B) = P_0\delta(B) + \sum_{n=1}^{N} I_n(B)P_n \tag{10}$$

where

$$I_n(B) = \frac{1}{\pi^{3n/2}} \int d\boldsymbol{q}_1 ... d\boldsymbol{q}_n e^{-\sum_{i=1}^n \boldsymbol{q}_i^2} \delta\left(\sum_{i=1}^n b(\boldsymbol{q}_i) - B\right)$$

where both $b(\boldsymbol{q}_i)$ and B are dimensionless quantities.

IV. Energy Distribution

This section is rather a prelude to the calculations in the forthcoming sections which constitute the core of this work. Its main purpose is to verify the validity of expression (8) and to acquire certain dexterity in executing the computations that this formula implies. Applying the recipe given in the previous section we first conclude

that since $a(\boldsymbol{p}_i) = \boldsymbol{p}_i^2 / 2m = \boldsymbol{q}_i^2 / \beta$ we have $b(\boldsymbol{q}_i) = \boldsymbol{q}_i^2$ and $B \equiv \varepsilon = E\beta$. Our task mainly comes down to evaluating

$$I_n(\varepsilon) = \frac{1}{\pi^{3n/2}} \int d\boldsymbol{q}_1 ... d\boldsymbol{q}_n e^{-\sum_{i=1}^n \boldsymbol{q}_i \delta} \left(\sum_{i=1}^n \boldsymbol{q}_i^2 - \varepsilon \right), \tag{11}$$

Noting that the integrand can be reduced to a function of $R = \sum_{i=1}^N \boldsymbol{q}_i^2$, in $3n$ dimensional polar coordinates the integral simplifies to

$$I_n(\varepsilon) = \frac{C_{3n}}{\pi^{3n/2}} \int_0^\infty dR R^{3n-1} e^{-R^2} \delta(R^2 - \varepsilon) \ ,$$

where $C_m = 2\pi^{m/2} / \Gamma(m/2)$ is the total solid angle in the *m* dimensional space. Performing the change of variables $y = R^2$ we get

$$I_n(\varepsilon) = \frac{1}{\Gamma\left(\frac{3n}{2}\right)} \int_0^\infty dy y^{\frac{3n}{2}-1} e^{-y} \delta(y - \varepsilon) \ ,$$

yielding the Euler distribution of order $p = 3n/2$ and parameter $\lambda = 1$ (see Appendix A):

$$I_n(\varepsilon) = \frac{\varepsilon^{\frac{3n}{2}-1} e^{-\varepsilon}}{\Gamma\left(\frac{3n}{2}\right)} \ . \tag{12}$$

One can check whether the expressions for the well known mean values of energy distribution are retained. According to Appendix A the momenta of the *n* particle distribution of the energy are

$$\langle \varepsilon \rangle = \frac{3n}{2}, \quad \langle \varepsilon^2 \rangle = \frac{3n}{2}\left(\frac{3n}{2} + 1\right)$$

The energy of the subsystem will then be characterized by

$$\langle E \rangle = \frac{1}{\beta} \int_0^\infty d\varepsilon f(\varepsilon) \varepsilon = \frac{3}{2\beta} \sum_{n=0}^N n P_n = \frac{3\langle n \rangle}{2\beta} \ , \tag{13}$$

and

$$\langle E^2 \rangle = \frac{1}{\beta^2} \int_0^\infty d\varepsilon f(\varepsilon) \varepsilon^2 = \frac{1}{\beta^2} \left[\frac{9}{4} \langle n^2 \rangle + \frac{3}{2} \langle n \rangle \right]$$

Note that all above was established with the only assumptions that the gas in equilibrium is mono-atomic and the interaction is not momentum dependent. The particularities of the interaction influence exclusively the particle number distribution, P_n, through eq. (5). Obviously, even the simplest interaction can make the exact calculation of P_n hopeless. However, for an ideal gas the task becomes a trivial one.

In this case a consequence of equilibrium is spatial homogeneity entailing a binomial distribution for P_n (see Appendix A) with the probability of finding any given particle inside the subsystem, $p = V/W$. If the system is large, $N >> 1$, this distribution is rather of Poisson type with the parameter $\langle n \rangle = NV/W$ representing the average particle number in the subsystem. If the system is finite, using the properties of the binomial distribution the mean square deviation of the energy of the subsystem in

$$\left\langle \Delta E^2 \right\rangle = \frac{E}{\beta}\left[\frac{5}{3} - \frac{2}{3}\frac{V}{W}\right], \tag{14}$$

V. Momentum Distribution

It is reasonable to assume that all interactions are such that the system is isotropical i.e., there are no external fields or preferred directions of motion and clustering. Thus, the only quantity of interest is $f(P_z)$. Repeating the steps from the previous section we find that in (10) $a(\boldsymbol{p_i}) \equiv p_i^z = \sqrt{2m/\beta}\, q_i^z$. Consequently, $b(\boldsymbol{q_i}) \equiv q_i^z$ and $B \equiv \eta_z \equiv P_z\sqrt{\beta/2m}$. The particle number constrained distribution function takes the form

$$I_n(\eta_z) = \frac{1}{\pi^{3n/2}} \int d\boldsymbol{q}_1 ... d\boldsymbol{q}_n e^{-\sum_{i=1}^{n} q_i^2} \delta\left(\sum_{i=1}^{n} q_i^z - \eta_z\right).$$

We can perform the integrations over the x and y components getting

$$I_n(\eta) = \frac{1}{\pi^{n/2}} \int dq_1 .. dq_n e^{-\sum_{i=1}^{n} q_i^2} \delta\left(\sum_{i=1}^{n} q_i - \eta\right),$$

where the index z is suppressed. Integrating with respect to q_n the Dirac function will produce a bilinear expression in q_i in the exponential:

$$I_n(\eta) = \frac{1}{\pi^{n/2}} \int dq_1 ... dq_{n-1} e^{-\sum_{i=1}^{n-1} q_i^2 - \left(\eta - \sum_{i=1}^{n-1} q_i\right)^2}$$

$$= \frac{e^{-\eta^2}}{\pi^{n/2}} \int dq_1 ... dq_{n-1} e^{-(q|M|q)+(c|q)} ,$$

where

$$|q) = \begin{pmatrix} q_1 \\ q_2 \\ \vdots \\ q_{n-1} \end{pmatrix}, \quad M = \begin{pmatrix} 2 & 1 & \cdots & 1 \\ 1 & 2 & \cdots & 1 \\ \vdots & \vdots & \ddots & \vdots \\ 1 & 1 & \cdots & 2 \end{pmatrix},$$

and

$$(c| = 2\eta(1111...1)$$

From eq. (A1) in Appendix A

$$\int dq_1 ... dq_{n-1} e^{-(q|M|q)+(c|q)} = \sqrt{\frac{\pi^{n-1}}{n}} e^{\eta^2 \frac{n-1}{n}} ,$$

where we have made use of the partial results, $\det(M) = n$ and

$$M^{-1} = \frac{1}{n} \begin{pmatrix} n-1 & -1 & \cdots & -1 \\ -1 & n-1 & \cdots & -1 \\ \vdots & \vdots & \ddots & \vdots \\ -1 & -1 & \cdots & n-1 \end{pmatrix}$$

Finally, the distribution attains the simple Gaussian form

$$I_n(\eta) = \frac{e^{-\eta^2/n}}{\sqrt{n\pi}}$$

Here we note that unlike in the case of energy, the *n* particle distribution of the momentum behaves as in the limit of large numbers. However, since for obtaining the actual momentum distribution function of the subsystem we have to use the weighted sum in (8) by no means we can conclude that this will also show the same properties as the large particle number limit.

VI. The Characteristic Function Method

The characteristic function of a continuous distribution is its Fourier transform

$$f(\omega) = \sum_{n=0}^{N} P_n I_n(\omega) \tag{15}$$

where $I_n(\omega)$ is the Fourier transform of $I_n(B)$. In the case of an ideal gas in equilibrium

$$I_n(\omega) = \frac{1}{\pi^{3n/2}V^n}\int d\boldsymbol{q}_1 d\boldsymbol{r}_1 ... d\boldsymbol{q}_n d\boldsymbol{r}_n e^{-\sum_{i=1}^{n}[\boldsymbol{q}_i^2 - i\omega b(\boldsymbol{r}_i,\boldsymbol{q}_i)]} = I_1^n(\omega),$$

where

$$I_1(\omega) = \frac{1}{\pi^{3n/2}V}\int d\boldsymbol{r} d\boldsymbol{q} e^{-\boldsymbol{q}^2 + i\omega b(\boldsymbol{r},\boldsymbol{q})} \equiv I(\omega) \ , \tag{16}$$

which is unity at $\omega = 0$ as expected from the normalization property of the $I_1(B)$ distribution function. If $b(\boldsymbol{r},\boldsymbol{q}) = b(\boldsymbol{q})$, i.e., the studied quantity is strictly momentum dependent, we have

$$I_1(\omega) = \frac{1}{\pi^{3/2}}\int d\boldsymbol{q} e^{-\boldsymbol{q}^2 + i\omega b(\boldsymbol{q})} \ .$$

In the case of the energy $b(\boldsymbol{q}) = \boldsymbol{q}^2$ therefore

$$I(\omega) = \frac{1}{\pi^{3/2}}\int d\boldsymbol{q} e^{-\boldsymbol{q}^2(1-i\omega)} = (1-i\omega)^{-\frac{3}{2}} \ .$$

In the case of momentum $b(q) = q$ whence

$$I(\omega) = e^{-\frac{\omega^2}{4}} \tag{17}$$

For a homegeneous system P_n represents a Binomial distribution and the characteristic function is expressed by

$$f(\omega) = \left[1 + p(I(\omega) - 1)\right]^N , \tag{18}$$

where *p* = *V*/*W* with *V* and *W* the volume of the subsystem and of the total system, respectively, and *N* is the total number of particles. For an infinite system, $N \to \infty, P_n$ is a Poisson distribution (see Appendix A) whence, by (15),

$$f(\omega) = e^{\langle n\rangle[I(\omega)-1]} \ . \tag{19}$$

The Fourier transform proves to be especially useful in the study of fluctuations in the limit of large numbers. For convenience we Taylor expand $I(\omega)$ up to second order:

$$I_1(\omega) = 1 + i\omega\lambda - \frac{1}{2}\omega^2\gamma^2 + ... \ , \tag{20}$$

where

$$\lambda = \frac{1}{V\pi^{3n/2}} \int d\boldsymbol{r} d\boldsymbol{q} b(\boldsymbol{r}, \boldsymbol{q}) e^{-\boldsymbol{q}^2} \ ,$$

$$\gamma^2 = \frac{1}{V\pi^{3n/2}} \int d\boldsymbol{r} d\boldsymbol{q} b(\boldsymbol{r}, \boldsymbol{q})^2 e^{-\boldsymbol{q}^2} \ ,$$

and we made use of the normalization condition $I(0) = 1$. Since the Fourier transform of a Gaussian,

$$g(x) = \frac{1}{\sqrt{2\pi}\sigma} e^{-(x-\alpha)^2/2\sigma^2} \ ,$$

centred around α and having the width σ is

$$g(\omega) = e^{i\omega\alpha - \omega^2\sigma^2/2} \ ,$$

one obtains from (19) and (20) that

$$\langle B \rangle = \langle n \rangle \lambda \text{ , and } \Delta B^2 \equiv \langle B^2 \rangle - \langle B \rangle^2 = \langle n \rangle \gamma^2 \ .$$

The Taylor coefficients for the energy are

$$\lambda = \frac{3}{2} \text{, and } \gamma^2 = \frac{15}{4}$$

in line with (13) and (14).

More generally, we observe that the higher momenta satisfy the equation

$$\langle B^k \rangle = i^k \, f(\omega)^{(k)} \Big|_{\omega=0} \equiv i^k \, \tilde{f}^{(k)} \ . \tag{21}$$

In order to evaluate (21) on concrete cases we assume the limit of an infinite system and use (19). For the sake of clarity we write out some of the intermediate results:

$$\tilde{f}' = \tilde{I}'$$
$$\tilde{f}'' = \tilde{I}'' + \tilde{I}'^2$$
$$\tilde{f}''' = \tilde{I}''' + 3\tilde{I}'\tilde{I}'' + \tilde{I}'^3$$
$$\tilde{f}^{(4)} = \tilde{I}^{(4)} + 4\tilde{I}'''\tilde{I}' + 6\tilde{I}''\tilde{I}'^2 + 3\tilde{I}''^2 + \tilde{I}'^4$$

The fourth statistical momentum of the dimensionless kinetic momentum can be obtained by using (17) which yields

$$\left\langle p^4 \right\rangle = \frac{3}{4}\langle n \rangle \left(\langle n \rangle + 1 \right).$$

It is of interest to see the dependence of the relative deviation from the large particle number limit provided by the normal distribution on the size of the subsystem. We define this quantity as

$$\Delta x^k \equiv \frac{\left\langle x^k \right\rangle - \left\langle x^k \right\rangle_G}{\left\langle x^k \right\rangle_G}$$

where the subscript *G* denotes averaging by a normal distribution. In the case of momentum

$$\Delta p^2 = 0 \qquad \text{and} \qquad \Delta p^4 = \frac{1}{\langle n \rangle} \qquad (2)$$

As we can see there is no deviation up to the second moment. On the other hand there is a decaying deviation inversely proportional with the subsystem size in the case of the fourth momentum. The above quantitative results are valid in the large system size limit. One expects stronger deviation for finite systems described by (18). We have not considered this case as the derivation of the quantities of interest, even though more involved, are straightforward.

VII. Angular Distribution Function

In order to obtain the distribution of one of the components of the angular momentum, $f(L_z)$, we need to work with the extensive quantity $a = (\boldsymbol{r} \times \boldsymbol{p})_z$ which in cylindrical coordinates is $a = rp\sin(\phi_p - \phi_r)$ with ϕ_r, ϕ_p as the azimuthal angles of position and momentum, respectively. The main difference between present and the previous cases is, that a_i depends on both position and momentum. We assume that the studied domain, D, is a cylinder of radius R and height h standing parallel to the z axis. For an ideal gas the Fourier transform of the one particle distribution function, $I_1(l)$, in dimensionless form and using cylindrical coordinates writes

$$I_1(\omega) = \frac{1}{\pi^2}\int_0^1 du u \int_0^\infty dq q e^{-q^2} \int_0^{2\pi} d\phi_u \int_0^{2\pi} d\phi_q e^{i\omega u q \sin(\phi_q - \phi_u)}$$

where

$$u = \frac{r}{R},\ u_z = \frac{z}{h},\ \boldsymbol{q} = \sqrt{\frac{\beta}{2m}}\boldsymbol{p},\ l = \frac{1}{R}\sqrt{\frac{\beta}{2m}}L_z.$$

which, according to Appendix B, takes the form

$$I_1(\omega) = \frac{4}{\pi}\int_0^1 duu\int_0^\infty dqqe^{-q^2}\int_{-1}^1 dt\frac{\cos(\omega uqt)}{\sqrt{1-t^2}} =$$

$$= 4\int_0^1 duu\int_0^\infty dqqe^{-q^2}J_0(\omega uq) =$$

$$= 2\int_0^1 duue^{-\omega^2u^2/4}$$

where we have used the definition and properties of Bessel functions presented in Appendix A. Finally,

$$I_1(\omega) = \frac{4}{\omega^2}\left[1-e^{-\omega^2/4}\right]$$

Using the tools developed in the previous section in the limit of a large system we find that

$$\left\langle l^2\right\rangle = \frac{\left\langle n\right\rangle}{4},\ \left\langle l^4\right\rangle = \frac{\left\langle n\right\rangle}{4}\left(\mathbf{A}+\frac{3}{4}\left\langle n\right\rangle\right),\ \Delta l^2 = 0,\ \Delta l^4 = \frac{4}{3}\frac{1}{\left\langle n\right\rangle}$$

VIII. Conclusions

We have presented a general expression for the distribution function of an extensive parameter of a classical subsystem. We checked its validity on known ases. Then the expression of the distribution function for the energy and momentum currents have been derived. These quantities are of special mportance as they are directly involved in numerical fluctuating ydrodynamics methods. The general expression was applied for the case of a monoatomic gas in equilibrium. The characteristic function of the distribution proved to be useful in providing a general tool for estimating arbitrarily high moments of the fluctuating quantities. It is shown how these moments can be calculated in the limit of a large system wherein the particle number distribution of the subsystem follows a Poisson distribution function. We concluded that the second moment of the momentum and angular momentum coincide with that in the large particle number limit. However, we found that the relative deviation in the fourth momenta follow an $\left\langle n\right\rangle^{-1}$ decay law. This represents an over unity value for those numerical fluid dynamics calculations describing heavy-ion collisions that use numerical grid cells that contain less then one particle on the average. The same deviations can be calculated including finite size effects arising from the finiteness of the total system by using the same prescription.

Even though the obtained formulae become involved for higher moments they are a straightforward job for software tools equipped with symbolic computation features.

This paper represents a first step on a long and wide road. The provided tools could be used for performing similar calculations in the finite system size limit. It is of great interest to see how the above results change in the presence of non-equilibrium conditions. It is to be clarified to what extent the fluctuations in a gas subjected to flow velocity gradients can be connected to the appearance of turbulences and whether quantitative predictions can be made on the distribution of vortices. In other words, can the presented approach bridge over the gap between the mesoscopic level of the fluctuating fluid elements and the near macroscopic level of turbulent flows? As pointed out in ref. [6] conserved currents across fluid cell boundaries are essential for implementing fluctuating hydrodynamics methods. Therefore it is imperative that this study is followed by another one focusing on the fluctuations of conserved currents.

APPENDIX A:

USED FORMULAE

Binomial distribution

$$P_n = \binom{N}{n} p^n (1-p)^{N-n}, 0 < p < 1, \tag{A1}$$

$$\langle n \rangle = Np, \langle n^2 \rangle = \langle n \rangle^2 + \langle n \rangle (1-p) \ .$$

Poisson distribution:

$$P_n = \frac{\langle n \rangle^n}{n!} e^{-\langle n \rangle} \ ,$$
$$\langle n^2 \rangle = \langle n \rangle^2 + \langle n \rangle \ .$$

Euler's (gamma) distribution of order *p* and parameter λ

$$f_p(\lambda) = \frac{\lambda^p x^{p-1}}{\Gamma(p)} e^{-\lambda x} \ , \ x \geq 0 \ , \ p > 0, \lambda > 0 \ ,$$
$$\langle x^k \rangle = \frac{p(p+1)...(p+k-1)}{\lambda^k} \ .$$

One dimensional normal distribution

$$g(x)=\frac{1}{\sqrt{2\pi}}\exp\left[-\frac{(x-a)^2}{2}\right],$$

$$\left\langle x^k\right\rangle=\sum_{i=0}^{k}\binom{k}{i}a^{k-i}s_i\,,\qquad s_{2i}=(2i-1)!!\,,\ \ s_{2i-1}=0\,,\quad i>0\,,\qquad \text{(A2)}$$

where s_i stands for the *i*th momentum of the standard normal distribution.

Multi-dimensional Gaussian integral

$$\int dx_1...dx_n e^{-(x|M|x)+(c|x)}=\sqrt{\frac{\pi^2}{\det(M)}}e^{\frac{1}{4}(c|M^{-1}|c)}\,,$$

where

$$|x)=\begin{pmatrix}x_1\\x_2\\\vdots\\x_n\end{pmatrix},\quad (x|=(x_1\quad x_2\quad ...\quad x_n)\,,$$

M is a symmetric positive definite $n\times n$ matrix and

$$(c|=(c_1\quad c_2\quad ...\quad c_n)\ .$$

Euler's Γ function:

$$\Gamma(n)=\int_0^\infty dx e^{-x}x^{n-1}\,,\text{ where }\ n>-1\,,$$

Bessel functions

$$J_\nu(z)=\frac{(z/2)^\nu}{\Gamma\left(\frac{1}{2}\right)\Gamma\left(\nu+\frac{1}{2}\right)}\int_{-1}^{1}dt(1-t^2)^{\nu-1/2}\cos zt$$

$$\text{Re}\ \ \nu>-\frac{1}{2}\ ,\ |\arg z|<\pi\ .$$

Weber's integral:

$$\int_0^\infty dx e^{-a^2x^2}J_\nu(bx)x^{\nu+1}=\frac{b^\nu}{(2a^2)^{\nu+1}}e^{-b^2/4a^2}\,,\quad a>0,b>0,\text{Re}\,\nu>-1\ .$$

APPENDIX B:

DERIVATION

$$\int_0^{2\pi} dx \int_0^{2\pi} dy f(\sin(y-x)) = \int_0^{2\pi} dx \int_{-x}^{2\pi-x} dz f(\sin z) = \int_0^{2\pi} dx \int_0^{2\pi} dz f(\sin z) =$$

$$= 2\pi \int_0^{2\pi} dz f(\sin z) = 4\pi \int_0^{\frac{\pi}{2}} dz [f(\sin z) + f(-\sin z)] =$$

$$= 2\pi \int_{-1}^{1} \frac{dt}{\sqrt{1-t^2}} [f(t) + f(-t)].$$

REFERENCES

1. L. P. Csernai, *Introduction to Relativistic Heavy Ion Collisions*, Wiley (1994)
2. L.A. Crum, Phys. Today Sept., 22 (1994)
3. R. Apfel, Nature 398, 378 (1999)
4. S. Putterman, Sci. Am. Feb. 32 (1995)
5. L.D. Landau and E.M. Lifsitz, JETP 5, 512 (1957).
6. L.P. Csernai, Z.I. Lázár, D. Molnár, J. Pipek, and D.D. Strottman, Phys. Rev E61, 237 (2000).
7. M.M. Mansour, A.L. Garcia, G.C. Lie, and E. Clementi, Phys. Rev. Lett. 58, 874 (1987).
8. A.L. Garcia, M.M. Mansour, G.C. Lie, M. Mareschal, and E. Clementi, Phys. Rev. A 366, 4348 (1987)
9. A.L. Garcia, M.M. Mansour, G.C. Lie, and E. Clementi, J. Stat. Phys. 47, 209 (1987).
10. F. Baras, M. Mansour, and A. Garcia, Am. J. Phys. 64, 1488 (1996)
11. N. Lebedev, Special Function and Their applications Prentice-Hall, Englewood Cliffs (1965)

STUDIA UNIVERSITATIS BABEŞ-BOLYAI, PHYSICA, XLIX, 1, 2004

MESUREMENT OF THE CONCENTRATION OF SOME HEAVY METALS IN THE TÂRNĂVENI AREA SOIL

I. SUCIU*, C. COSMA, M. TODICA

Babeş Bolyai University, Faculty of Physics, M. Kogălniceanu no. 1, 400084 Cluj-Napoca, Romania, siioan@hotmail.com

ABSTRACT. The concentration of some heavy metals were measured in the are of some centers of the chemical industry known as centers off pollution. The samples were prlevead from locations where there are not ground sliding and the probability of alluvial deposits is very reduced. The concentration of heavy metals was measured by ICP and NAA methods. Only in some locations the concentration of these methals excedes the admited concentration.

Key words: polution, heavy metals, Târnăveni

Introduction

Monitoring the heavy metals concentration in the soil is of great interest on today, considering the fact that many of these elements have a high toxic potential.

The metals are described as “heavy metals” which, in their standard state, have a specific gravity of more than about 5g/cm^3. There are 60 heavy metals. Only when they are present in greater quantities, can these heavy metals, such as lead, cadmium and mercury, which are already toxic in very low concentrations, cause metabolic anomalies.

The presence of these metals in the soil or in the air has a natural cause but also the result of the human activities. Some of these heavy metals, presents in the soil are assimilated by plants and animals. Not all the traces of heavy metals in plants and animals are the results of human activity. Some appear due to the absorption processes of naturally occurring soil components, as has been shown for cadmium in particular. Purely theoretically, every 1000 kg of ”normal” soil contains 200g chromium, 80g nickel, 16g lead, 0,5g mercury and 0,2g cadmium, [1].

I. The Toxic Heavy-Metals

Elements such as chromium, cadmium, lead is known as causes of many diseases. For example, **chromium** (**Cr)**, especially Cr VI is irritating, allergic and one of the factors which determine the forming of methemoglobin - effect, accompanied by stifling and cyanosis. At the same time chromium causes anemia, pulmonary cancer and, less often, larynx or nose cancer. The same element can cause skin lesions, ulcers, gastroenteritis, severe stomatitis and nitrimia,[2]. More often than not, chromium is present in the soil as chromate ion, Cr VI and rarely, as Cr II.

Lead (Pb)

Lead is a typically cumulative poison. The danger of chronic intoxications is the greater problem. Basically, as a result of their comparatively high affinity for proteins, the lead ions consumed bind with hemoglobin (red blood pigment) and the plasma protein in the blood. This leads to inhibiting the synthesis of red blood cells, thus preventing the vital transport of oxygen. If the binding capacity here is exceeded, lead passes into the bone marrow, liver and kidneys. Such intoxication leads to:

- Encephalopathy in the central nervous system (CNS);
- Disturbances in kidney and liver functions, ending up in necrosis;
- Damages of the reproductive organs;
- Anemia and many metabolic deficiency symptoms.[3,4,6]

Mercury - "quicksilver" (Hg)

Mercury in the form of its methyl compounds is specifically the most toxic of the heavy metals. When consumed orally, it first passes into the liver, the kidneys and the brain. Accumulation only takes place temporarily. A large part is excreted with the faeces. The salts of bivalent mercury, in the cases of chronic consumption, first cause tiredness, loss of appetite and loss of weight. In the end the kidneys fail. Muscular weakness and paralysis are typical,[5,6].

Copper (Cu) is included in the so-called trace elements and it is essential, in very small concentration, to the survival of all forms of life. Nonetheless, it is often forgotten that in certain circumstances, in higher concentrations, these can also be quite toxic, for example when they are present in an organic compound, [1].

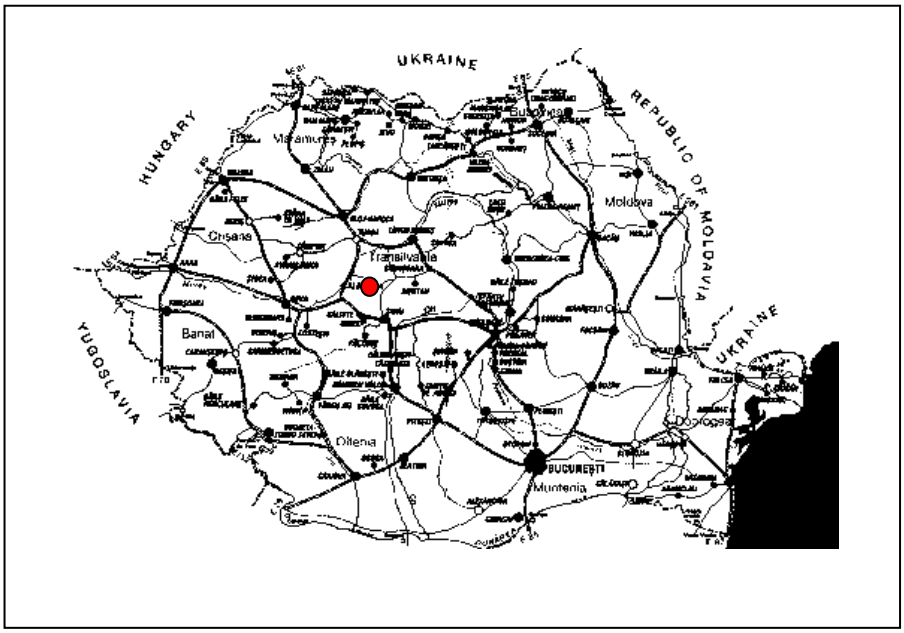

Fig. 1. The position of Târnăveni, in Romania

II. Materials and Methods

Since in the industrial areas where the respective metals are obtained or transformed the presence of these elements is more probable and as in these areas the question whether the concentration falls in the range accepted by the legislation is particularly raised, several such important areas have been spotted.

Samples have been taken from Târnăveni area (Romania), Mureş County.

The city of Târnăveni is situated on the bank of the Târnava Mică River and is acknowledged as an important center of the chemical industry. Even if only carbide and acetylene are produced on the chemical platform at present, previous activities must also be considered.

The first factory in the field was set up in 1916 under the name of NITROGEN S.A. and over the years it processed mercury, gold, bismuth, barium salts, copper sulohate, sodium and potassium dichromate, sulphuric acid etc.

Even if it is acknowledged as an important polluting center, indirectly defiling the Mureş River itself, there are no systematic surveys referring to the pollution generated in the city neighboring area. Unlike other centers such as Zlatna, Baia Mare or Copşa Mică, the investigation of pollution in the Târnăveni area seems to have been neglected.

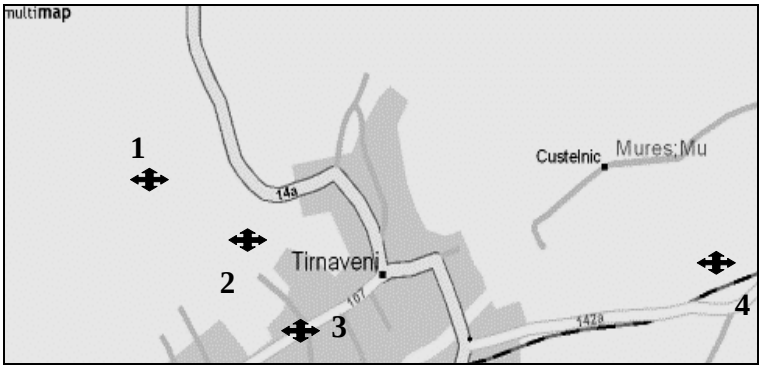

Fig. 2. The position of the 4 locations in Târnăveni area
Legend: 1-Dâmbău, 2 Combinat, 3 Batal(B), 4 Râioasa

The soil structure in the area has also been taken into consideration: brown and black earths, *pseudoredzinic* soils, hayfiled black earth, *regosoils*, clay soils and alluvial soils (the latter areas have been avoided). The fact that the degree of vulnerability of these types of soil to the pollution with heavy metals, is average or reduced, is considered an advantage in obtaining very accurate long-term information concerning the soil pollution.

To draw the samples, there have been chosen locations where neither ground sliding nor the existence of any alluvial sediment has been identified. The established locations have been chosen to ensure information both about the areas situated very close to the industrial platform and at greater distance, usually 2-7 kilometers away from it. Six locations have been established. In each location holes with an area of 40x50 cm have been dug and samples have been taken from depths of 5 cm, 15 cm and 25 cm. The samples have been put in polyethylene containers, which had previously been treated with a molar solution of hydrochloric acid and rinsed with distilled water, [8]. In this way the contamination of samples

was prevented, taking into account the fact that the determinations have been made, in some cases, with up to 1ppb accuracy, [7]. After drying, the samples have been sifted and homogenized, and then they have been labeled and separated, in view of analysis. Portions of samples have been prepared to determine the concentration by NAA at ICN Pitesti and by ICP-OES at EXPROGAZ MEDIAŞ.

The aim of our work is to measure the concentration of the heavy metals in some location within the sensible area Târnăveni, exposed to the pollution, and to compare the results with the maximum value admitted by legislation.

II.1. NAA

Average samples of 70 mg each have been retained. These were irradiated in the pneumatic mail of the TRIGA reactor. There were registered: the flow of the thermal neutrons (E<0,5eV)=$4,7 \cdot 10^{12}$ n/cm^2/s; the cadmium ratio: RCd=1,8; the thermal flow/epithermal flow ratio ≈ 10. The irradiation time was from 1,5 up to 2 hours. The measuring of the activity was made with a γ spectrometer chain of high resolution with an HpGe detector having a relative efficiency of 20%.

The time of measurement ranged within 3000s and 12000s.The measuring started after the cooling of Na^{24}, isotope whose halving time is 15 hours. The determining of the concentration was made by means of the KO method with a Zr monitor; a method whose detection limits varies between 3 and 5 ppm, as follows. The data obtained were processed with the GENIE 2000 soft.

The determining was compared with the measuring on standard samples (SRM).

II.2. ICP-OES

Average samples were collected of 250 mg each, to which were added 3 ml of HNO_3 65% and 3 ml of HF 40%. The mixture obtained was introduced in a microwave oven and disintegrated. After the digestion, it was introduced in a glass bubble and completed with distilled water up to 50 ml. The solution was placed in a plasma jet by means of a peristaltic pump, which has 8 rolls and 3 channels and a maximum speed of 200 rotations/minute, controlled by the computer.

An ultrasonic Cross-flow Babbington IRIS ADVANTAGE nebulisor spectrometer and an Echell-type cross-dispersion spectrograph were used covering a specter interval of 178-800 nm. The system resolution ranged from <0,01nm to <200nm to<0,03 to 600nm. The CID38196mm^2 detector with 262144 grouped individual detectors into a 512x512 matrix, cooled with a two-step heat changer allowed of integration with a random access. The source of plasma rousing with the frequency of 27,12 MHz, controlled by the crystal can supply a power of 750-1750W, in 6 steps, controlled by the computer.

The data obtained were processed in a first stage with the Thermos SPEC/CID soft. The soft contains a library of 20000 lines, all of which are accessible in at least one order/degree of diffraction and it gives the possibility of obtaining the image of the whole specter and of completely identifying the peaks.

The detection limits ranged from1 ppm to1ppb, as follows:

Cu, Co, Hg <1ppb, Hg<10ppb.

III. Results

Co **Table 1**

Reference Value in the Sensitive Areas Rvs (Ppm)	Alert Level in the Sensitive Area Als (Ppm)	Alert Level in the Less Sensitive Area Alls (Ppm)	Reference Value in the Less Sensitive Area Rvls (Ppm)	Area Intervention Threshold Ait (Ppm)
15	30	100	50	250

The first location, situated at 3 km West from the Chemical Platform, represents the only place where there has been identified the presence of Cobalt.

At the same time, in the 4 th location, at 5 km East from the Chemical Platform, only the presence of Chromium has been registered within limits that don't exceed the intervention thresh hold in sensitive areas.

Cr **Table 2**

RVS (PPM)	ALS (PPM)	ALLS (PPM)	RVLS (PPM)	AIT (PPM)
30	100	300	300	600

Hg **Table 3**

RVS (PPM)	ALS(PPM)	ALLS(PPM)	RVLS (PPM)	AIT (PPM)
0,1	1	4	2	10

Most of the elements have been identified in the locations 2 and 3, which are situated near the Chemical Platform. In these locations there have been found concentrations over the intervention level.

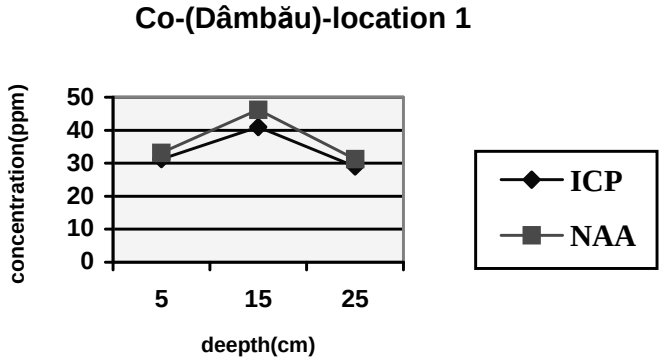

Fig. 3. Concentration of Co in location 1 area

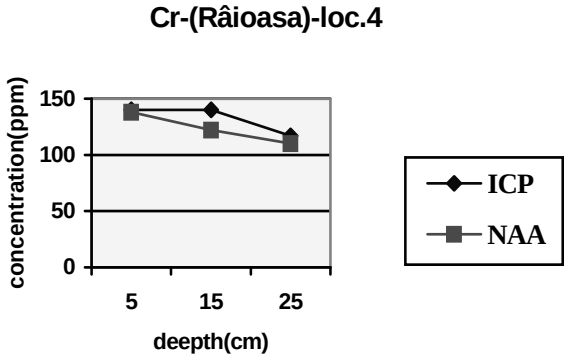

Fig. 4. Concentration of Cr in location 4

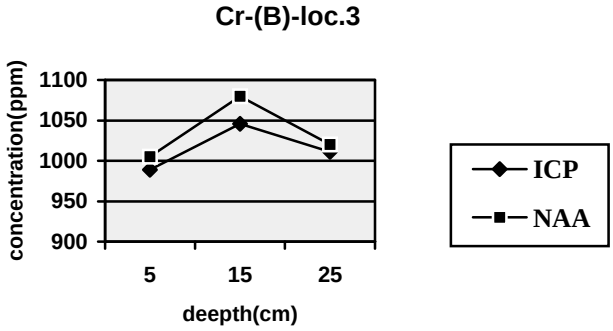

Fig. 5. Concentration of Cr in location 3

Cu **Table 4**

RVS (PPM)	ETS (PPM)	ETLS (PPM)	RVLS (PPM)	AIT (PPM)
20	100	250	200	500

[9]

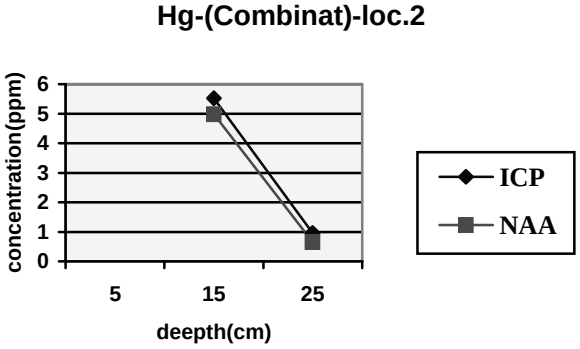

Fig. 6. Concentration of Hg in location 2

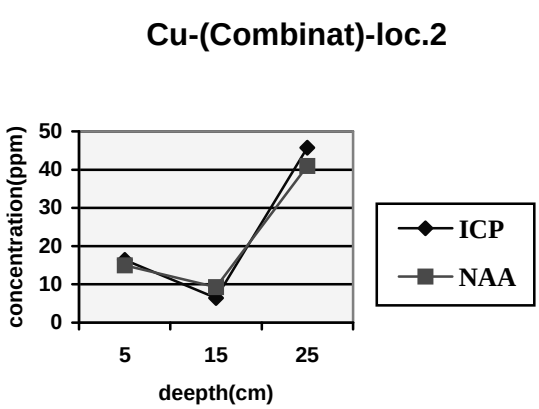

Fig. 7. Concentration of Cu in location 2

These remarks can be explained firstly by the distance between the respective locations and the infection area caused by the Chemical Platform. If we take into account the fact that the research monitories heavy metals, the circulation of the currents of air (from NW to E) is less important.

Conclusions

- In most of the areas, the concentrations of some heavy metals have been determined in locations of the Târnăveni area. At least in the sensitive areas, they exceed the alert level (agricultural areas), Fig.3, 4, and 5.
- The greatest excess was registered for chromium. Its concentration in the areas near the chemical yard of BICAPA company exceeds the intervention threshold, being 3,6 times higher than the reference value in the less sensitive areas, fig.5. Mercury has been identified in the same areas having a concentration, which, at the depth of 25 cm, exceeds 5,5 times the intervention level, fig 6.
- Copper concentration ranges within normal limits, fig.7.
- The differences registered between the two methods can be explained by the existence of several detection limits and by the problems connected to the homogeneity of solid samples.
- Determining of the concentration of several elements, at different depths in the soil, can lead to an image of the historical pollution in the studied area, provided measures are taken with a view to observing the choice of locations. Unlike these measurements, the measurement of concentration in air, in running waters or of the accumulations of chemical elements in lichens, provides data on the situation existing at a certain moment or in a brief period of time.
- Unlike the method studying the accumulations in lichens, the method of direct study of element concentration in soil eliminates the necessity of a reference batch and the corrections are not necessary.

REFERENCES

1. IOCC, CAOBISCO, Heavy metals, April1996
2. Gheorghe Mogoş, Intoxicații acute, p 46,82, Ed.medicală, Bucureşti 1981
3. Gheorghe Mogoş, Intoxicații acute, p 525-529, Ed.medicală, Bucureşti 1981
4. Gazza F., Lead and Cadmium:Sources, Metabolism, Dangers and Presence in Meat and in Meat Products, Ann.della Facolta di Med. Vet. 10, p171-181,1990
5. Gheorghe Mogoş, Intoxicații acute, p 518-524, Ed.medicală, Bucureşti 1981
6. Galas-Gorchev H., Dietary Intake of Pesticide Residues: Cadmium, Mercury and Lead, Food Add. and. Cont.8 p 793-806,1991
7. Standard Test Method for Determining Elements in Waste Streams by Inductively Coupled Plasma AES, American Society for Testing and Materials, nov. 1998
8. Malissa, Fresnius Z., Anal Chem. 319 p 357-363, 1984
9. Monitorul Oficial al României nr. 303 bis/6XII 1997-OM 756/1997

STUDIA UNIVERSITATIS BABEŞ-BOLYAI, PHYSICA, XLIX, 1, 2004

EFFECT OF ANNEALING ON THE PROPERTIES AND STRUCTURE OF THE 2212 SYSTEM

A. SIMON[1*], S. D. ANGHEL[1], I. G. DEAC[1], T. FRENȚIU[2], B. REIZ[2], G. BORODI[3], S. SIMON[1]

[1] *"Babeş-Bolyai" University, Faculty of Physics, 400084 Cluj-Napoca, ROMANIA*
[2] *"Babeş-Bolyai" University, Faculty of Chemistry, 400028 Cluj-Napoca, ROMANIA*
[3] *Institute of Molecular and Isotopic Technologies, Cluj-Napoca, ROMANIA*
∗ *corresponding author, E-mail: asimon@phys.ubbcluj.ro*

ABSTRACT. A superconducting sample with nominal composition $Bi_{2.0}Sr_{2.0}Ca_{1.0}Cu_{2.0}O_{8+x}$ (with x = 0.15-0.20) was investigated. It was annealed in air, at 845 ^{o}C, for 150 hours. The sample was investigated via AC susceptibility measurements and XRD. The elemental content of the sample (concentrations and stoichiometric coefficients) was studied via inductively coupled plasma source atomic emission spectroscopy (ICP-OES). It was established that an annealing, in air at 845^{o}C, for a time interval less or equal with 150 h has no significant influence on the elemental composition, but enhance the superconducting properties of the sample.

1. Introduction

The Bi-based superconducting family consists of three superconducting phases with quite similar crystal structures and general chemical formula: $Bi_{2-x}Pb_xSr_2Ca_{y-1}Cu_yO_{10+\delta}$, where y = 1, 2, 3 corresponds to the 2201 (T_C ~ 20 K), 2212 (T_C ~ 80 K) and 2223 (T_C ~ 110 K) phases respectively. The discovery of the Pb-free 2223 phase (x = 0) [1] was quickly followed by the synthesis of the Pb substituted 2223 [2]. It was found that the incorporation of Pb might speed up the formation of 2223 phase. The practical applications of high T_C superconductors may require samples under various aspects (bulk, tape, wire, and thin or thick films); therefor extra processing is also needed. Among these techniques, annealing is probably the most important and frequent.

The aim of the present paper is to investigate the influence of the annealing time on properties and structure of the basic, Pb free 2212 system via inductively coupled plasma optical emission spectroscopy technique (ICP-OES).

2. Experimental details

The starting sample used for further treatment and investigations was purchased from ALDRICH as fine black powder and has the nominal formula $Bi_{2.0}Sr_{2.0}Ca_{1.0}Cu_{2.0}O_{8+x}$, with x = 0.15-0.20. The powder was pressed at 200 atm in a cylindrical pellet and annealed in air, at a temperature of 845^{o}C, in a CARBOLITE RHF 16/3 owen for 150 hours. The critical temperature of the superconducting phases was determined by the AC susceptibility method, the measurements being performed

with the Oxford Instruments MagLab System 2000 (frequency: 1 kHz, magnetic field: 1 Oe). The superconducting phase formation was investigated via X-ray diffraction (XRD) on a Dron2 system, using the classical powder method with Cu K_α radiation and Ni filter. The composition of the samples was determined by ICP-OES technique using a SPECTROFLAME sequential spectrometer. Details about the sample digestion methods, reagents and the ICP spectrometer are given elsewhere [3, 4].

3. Results and discussion

Fig.1 shows the dependence of the real component of the AC susceptibility (dotted) on temperature for the original (Fig.1a) and annealed sample (Fig.1b). For a better identification of the superconducting phases with different T_C's, the dependence of $d\chi'/dt$ on the temperature was also plotted on the same graphs (continuous lines).

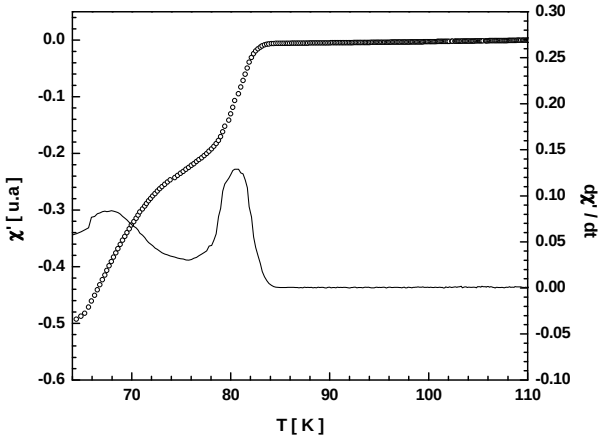

(a) - original sample

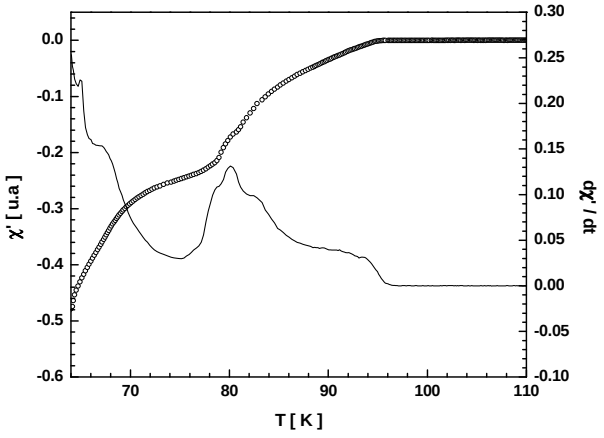

(b) - annealed sample

Fig.1. Temperature dependece of χ' and of $d\chi'/dt$ for the 2212 sample

Analysing these dependences one can say that in the original sample we have two high T_C phases, one with $T_C \sim 81$ K and an other one with $T_C \sim 68$ K, and the T_C^{onset} is 84 K.

Due to annealing in air for 150 h at 845^{o}C, beside those two phases, an other superconducting phase with $T_C \sim 92$ K appeared in our sample. A survey of the literature [5] suggests that this value of the critical temperature corresponds to the 2212 phase: with excess of Bi and Sr and deficit of Ca ($Bi_{2.18}Sr_{2.20}Ca_{0.80}Cu_{2.00}O_x$) or with deficit of Bi ($Bi_{1.90}Sr_{2.00}Ca_{1.00}Cu_{2.00}O_x$) or its appearance is due to changes in the oxygen stoichiometry or it is connected somehow to the intercalation of Pb (forming of PbBi2212 phase) [6–8]. This later situation could not be an explanation in our particular case. The annealing also caused an improvement in the onset of the superconductivity (up to 95 K) and in the intergranular behaviour of the sample.

Fig.2 shows the results of XRD analysis (Fig.2a – original sample, Fig.2b – annealed sample).

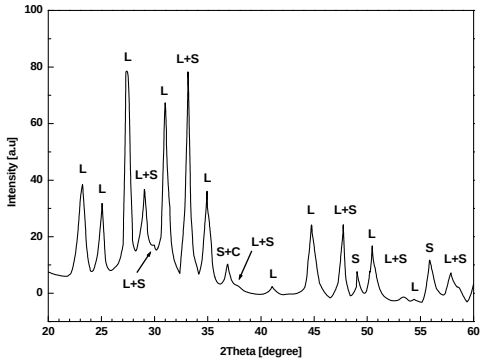

(a) - original sample

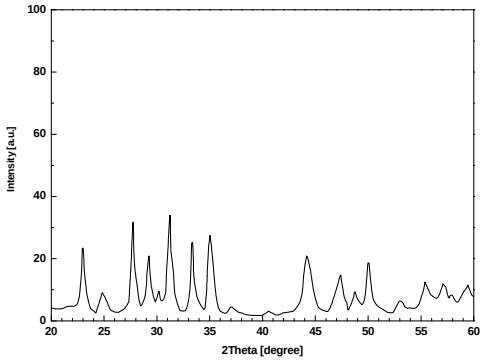

(b) - annealed sample

Fig.2. XRD patterns for $Bi_{2.0}Sr_{2.0}Ca_{1.0}Cu_{2.0}O_{8+x}$ samples

Analysing these XRD patterns one can say:

(i) the original sample has two of the three characteristic phases of the Bi family (2201 – "S", 2212 – "L") and there is a small amount of non – superconducting type impurity (CuO – "C"). Due to the fact that the most proeminent lines of the characteristic Bi families are overlaped, any estimation of the volumic fractions of the phases could lead to erroneous conclusions.

(ii) after annealing the original sample for 150 hours there is a change in the relative intensity ratios of the lines (possibly due to a rearrangement of the atoms in the structure of the sample) and the contribution of the small T_C and impurity phases was diminished. Due to the fact that the most proeminent lines of the characteristic Bi families are overlaped the T_C ~ 92 K phase could not be identified.

The elemental composition and the stoichiometry of the original sample, determined via ICP – OES technique, are presented in Table 1 and Table 2.

Table 1.

Elemental composition of the original (ALDRICH certified) 2212 sample

Elemental composition (%, m/m)	**Bi**	**Sr**	**Ca**	**Cu**
as certified	41	20	4.3	13
as determined *	41.8 ± 2.0	20.1 ± 0.5	4.2 ± 0.2	13.4 ± 0.3

* average concentration of 3 parallel measurements ± standard deviation

Table 2.

Stoichiometry of the original (ALDRICH) 2212 sample
(calculus based on data from Table 1)

theoretical	$Bi_2Sr_2Ca_1Cu_2O_{8+x}$ (x = 0.15 – 0.20)
as certified	$Bi_{1.87 \pm 0.12}Sr_{2.17 \pm 0.14}Ca_{1.02 \pm 0.07}Cu_{1.95 \pm 0.13}$
as determined	$Bi_{1.89 \pm 0.11}Sr_{1.99 \pm 0.12}Ca_{0.99 \pm 0.06}Cu_{1.99 \pm 0.11}$

The statistical validation of the results was performed in accordance with Miller and Miller [9] and was described extensively elsewhere [3]. It proved that there are no significant or systematic errors between the data obtained by us via ICP-OES technique on one hand and the certified or the theoretical results obtained by the same technique and given by the supplier [10, 11].

The elemental composition and the stoichiometry of the annealed sample determined via ICP – OES technique are presented in Table 3 and Table 4.

Table 3.

Elemental composition of the annealed 2212 sample

Elemental composition (%, m/m)	**Bi**	**Sr**	**Ca**	**Cu**
as determined *	41.5 ± 1.0	20.0 ± 0.3	4.2 ± 0.3	13.3 ± 0.3

* average concentration of 3 parallel measurements ± standard deviation

Table 4.

Stoichiometry of the annealed 2212 sample
(calculus based on data from Table 3)

as determined	$Bi_{1.88 \pm 0.11} Sr_{2.16 \pm 0.12} Ca_{0.99 \pm 0.06} Cu_{1.98 \pm 0.11}$

The influence of the annealing on the elemental composition and stoichiometry was investigated by means of statistical validation [3,9]. It was found that there is no significant differences between the results for the annealed sample and the certified results for the original 2212 sample. Thus, the annealing have not influenced the chemical composition of our 2212 sample.

4. Conclusions

In this paper results on the influence of annealing time on properties and structure of the starting system $Bi_{2.0}Sr_{2.0}Ca_{1.0}Cu_{2.0}O_{8+x}$, with x = 0.15-0.20 has been presented. AC susceptibility measurements and XRD analysis demonstrate the existence of superconducting phases 2201 and 2212 in the original sample. Due to annealing a superconducting phase with T_C ~ 92 K was appeared. Due to the fact that the most proeminent lines of the characteristic Bi families are overlaped, any estimation of the volumic fractions of the phases could lead to erroneous conclusions and the T_C ~ 92 K phase could not be identified. Therefor other techniques most be used in order to do that. The inductively coupled plasma optical emission spectroscopy analysis shows that the annealing have not influenced the chemical composition of our 2212 sample.

Acknowledgements

The experimental measurements presented in this paper were performed partially at the Research Institute for Analytical Instrumentation Cluj-Napoca (ICIA). The authors are thanful to Prof.dr. Emil A. Cordos, Head of ICIA for supporting their work.

REFERENCES

1. H. Maeda, Y. Tanaka, M. Fukutomi, T. Asano: Jpn. J. Appl. Phys. **27** (1988) L209
2. M. Takano, J. Takada, K. Oda, H. Kitaguchi, Y. Miura, Y. Ikeda, Y. Tomii, H. Mazaki: Jpn. J. Appl. Phys. **27** (1988) L1401
3. A. Simon: *PhD Thesis*, Babes-Bolyai University, Faculty of Physics, 2002.
4. A. Simon, S. D. Anghel, T. Frentiu, M. Ponta, M. M. Pop and S. Simon: Studia seria Physica, **XLVIII**, nr. 1, 25, 2003
5. P. Majewski: J.Mater.Res. **15** (2000) 854
6. K. Konstantinov, S. Karbanov, A. Souleva, D. Kovacheva: Supercond. Sci.Technol. **3** (1990) 309

7. A. K. Sarkar, B. Kumar, I. Maartense and T. L. Peterson: J. Appl. Phys. **65**, 2392, 1989
8. Jeremie, K. Alami-Yadri, J. C. Grivel and R. Flukiger: Supercond.Sci.Technol. **6** (1993) 730
9. J. C. Miller and J. N. Miller: "Statistics for Analytical Chemistry", Ellis Horwood Ltd, 1988
10. ALDRICH Product Description DataSheet
11. ALDRICH Product Certificate of Analysis

STUDIA UNIVERSITATIS BABEŞ-BOLYAI, PHYSICA, XLIX, 1, 2004

EPR LINE SHAPE AS A CRITERION IN PROVENANCE STUDIES OF LIMESTONES AND MARBLES

O.G. DULIU[a], M. VELTER-STEFANESCU[b],I. URSU[a]

[a]*University of Bucharest, Department of Atomic and Nuclear Physics, Magurele, P.O. Box MG-11, RO-077125 Bucharest, Romania*
[b]*National Institute of Materials Physics, Magurele, P.O. Box MG-7, RO-077125 Bucharest, Romania.*

ABSTRACT. Cluster analyses and numeric taxonomy have been applied to the analysis of the EPR spectra of Mn^{2+} ions in marble and limestone samples collected from 12 Greek historical quarries. In this way, it was possible to classify all samples in concordance with their mineralogical structure. At the same time, it has been shown that the Perason's correlation coefficient is most suitable to discriminate samples having different mineralogical composition while Euclidean and power distances showed to be more adequate in differentiating samples belonging to the same petrologic group.

Key words: EPR, Mn^{2+}, marble, limestone, provenance, cluster analyses, tree diagram

1. Introduction

Limestone and its metamorphic form, marble, have been intensively used as an excellent material for monumental art [1]. In the Mediterranean basin, the Greco-Roman civilization gave to these materials the ultimate expression of artistically perfection. For more than 2500 years, about 50 [2] quarries located both in Greece and Italy have constantly supplied high quality marble and limestone that has been used to create an impressive number of wok of art. At the same time, a flourishing trade has spread these objects far beyond the geographical limits of Mediterranean world.

With the development of modern archaeology, the question of the real origin of marble and limestone used in ancient architecture and sculpture becomes more and more actual, as this could give significant information concerning cultural interconnections or trade routes. At the same time, such studies are very useful in establishing the authenticity of various object of art carved in limestone or marble.

From geological point of view, marbles are composed of granular dolomite or limestone of organic nature (fossil coral skeletons, mollusks shells, and their debris) that have been recrystallized by the action of external agents such as pressure, heat or the presence of aqueous solutions. Marbles could be composed mainly of pure dolomite, pure calcite or a mixture of these components in various proportions. Different minerals such as quartz, mica, graphite, iron oxides, etc. seldom could be found in marbles. If present in a substantial proportion, these minerals could alter the original white color of marbles, by creating very attractive and colored patterns.

Despite some commune traits resulting from the mineralogical structure, there are a great number of particularities that make marbles extremely diverse. As a result, a large number of characteristic, can be used in provenance studies to discriminate or to bring together different kind of marbles or limstones. Several physico-chemical parameters such as trace elements or Rare Earth Elements concentrations [3-5], $\delta^{13}C$ and $\delta^{18}C$ isotopic ratio [6], intensity of specific thermoluminescence glow curve peaks [7], Mn^{2+} ions [8-17] or other free radicals [7,11-13] Electron Paramagnetic Resonance (EPR) spectra parameters have been used to solve this problem. Due to the fact that all these techniques finally furnish numerical values, different classification procedures based on multivariate statistical analysis [3,8,18-20] have been extensively used in the past decades.

It must be pointed out that, due to its ability to evidence various kind of paramagnetic centers, EPR has been frequently used, in provenance studies [21-23]. At the same time, as manganese is a ubiquitous element in the calcium carbonates of organic origin, the EPR spectrum of Mn^{2+} has been extensively investigated in marble and limestone, [7-17].

As the main aim of any provenance studies is to quantify, by using some numerical criteria, both similitude and difference between different samples for a better identification of considered samples, in this paper we propose a new discrimination criterion based on the analysis of Mn^{2+} EPR spectrum.

2. Materials and Methods

2.1 Samples

12 samples of marbles and limestone, collected from historical Greek quarries located over entire Greece, and belonging to different geotectonic zones [3,24]. From the investigated samples, only 9 specimens could be considered as pure marble, other 3 were unmetamorphosed limestone (see Table 1). From each sample, about 0.5 g aliquots have been taken crushed, finely ground in an agate mortal and homogenized.

Table1

Petrologic description of the investigated samples (after ref. [3], modified).

Place	Geo-tectonic zone	Type	Composition
Kerkira	Ionian	intraclastic limestone	calcite, traces of dolomite
Nauplio	Pindos	precipitation limestone	calcite
Drama	Rhodope	dolomitic marble	dolomite, traces of calcite
Kavalla	Rhodope	calcitic marble	calcite, traces of quartz
Thasos	Rhodope	dolomitic marble	dolomite, traces of calcite and magnesite
Didimon	Parnasian	dolomitic marble	calcite, small amount of dolomite
Trizina	Parnasian	sparry calcite	calcite + iron oxides
Dionysos	Subpelagonian	crystalline limestone	calcite
Aliveri	Pelagonian	calcitic marble	calcite, traces of dolomite
Gramatiko	Pelagonian	calcitic marble	calcite, traces of dolomite
Kozani	Pelagonian	calcitic marble	calcite
Naxos	Pelagonian	calcitic marble	calcite

2.2 EPR Measurements

Each EPR measurement has been performed at room temperature, by using an X-band JEOL JES ME 3X spectrometer provided with a cylindrical TE_{011} resonant cavity and a 100 kHz modulation. In order to make possible any further processing of experimental spectra, all of them have been digitally recorded by using the same modulation, *i.e.* 0.032 mT for a microwave power of 0.6 mW. DPPH and CaO:Mn^{2+} standard samples have been used for field calibration. As the sampling ratio of the magnetic field was the same (0.05 mT), each spectrum have been thus decomposed in the same number of points, that make possible any numerical intercomparison of the discrete numerical set of data that described all EPR spectra.

3. Results and Discussion

All investigated samples presented typical EPR spectra of Mn^{2+} ions for a local rhombic symmetry. In concordance with the mineralogical composition, we have observed mainly three types of Mn^{2+} EPR spectra, *i.e.* Mn^{2+} in calcite, Mn^{2+} in dolomite and Mn^{2+} in mixed samples consisting of a combination of calcite and dolomite (Fig.1).

The spectra of the first kind consist of six principal lines corresponding to the "allowed $\Delta m_I = 0$", transitions between superfine sublevels within ± ½ Kramers doublet [21,22]. Between the allowed transitions there are five groups of two lines due to the "forbidden $\Delta m_I = \pm 1$" transitions. (Fig. 1, Kozani). In calcite, $CaCO_3$, manganese ions, as a rule, substitute for calcium atoms in the calcium carbonate lattice generating the characteristic spectrum described above.

The second kind of spectra (Fig. 1, Drama) was identified by us in the dolomite rich samples. In dolomite $CaMg(CO_3)_2$, the divalent manganese substitute for both calcium or magnesium atoms, thus generating an intricate EPR spectrum consisting of a superposition of two kind of spectra: Mn^{2+} ions in the Ca^{2+} sites and Mn^{2+} ions in the Mg^{2+} sites.

The third kind of spectra was observed in calcite rich samples that contain small amounts of dolomite (Fig. 1, Gramatiko). It represents a superposition of the "calcite type" and "dolomite type" spectra that give a specific shape close to Mn^{2+} spectrum in calcite. More details concerning Mn^{2+} EPR spectra in calcite and dolomite can be found in Ref. [25-27].

In order to perform a further comparison, each EPR spectrum has been numerically integrated, so we obtained the true absorption lines. This procedure is very helpful not only in identifying the number of components of the EPR spectrum, but also in establishing similarities between different samples.

Due to the fact that all observed EPR spectra correspond to the same kind of ions in the same local rhombic symmetry, each allowed resonance line has an intricate structure that differs by the number of components as well as by the line-width, this parameter being in a positive correlation with the ions concentrations. For that reason, two resonance lines having the same position in spectrum, but belonging to two different samples, could be compared by using several criteria, currently applied in numerical taxonomy.

In our case, we found that Euclidean and power distances as well as the Pearson's correlation coefficient are among the most suitable criteria to classify marbles samples by using the Mn^{2+} EPR spectra.

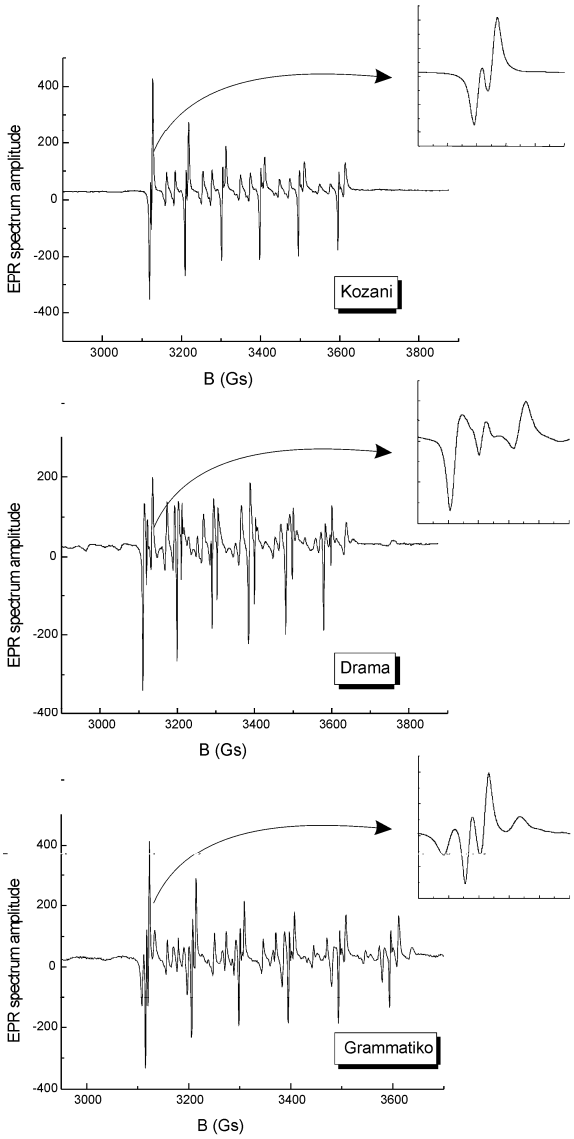

Fig. 1 - Typical EPR spectra of calcitic marble from Kozani, dolomitic marble from Drama, and calcito-dolomitic marble from Gramatiko. In the insets are reproduced, at a larger scale, the low field Mn^{2+} EPR lines used in this study.

Euclidian distance between two equal sets of *i* numerical values, p_i and q_i is defined by the equation:

$$d_E = \sqrt{\sum_i (p_i - q_i)^2} \quad (1)$$

In some cases, if it necessary to increase or decrease the progressive weight that is placed on the number of values within a set or on the difference between values, instead of Euclidian distance a power distance can be computed:

$$d_P = \sqrt[n]{\sum_i (p_i - q_i)^k} \quad (2)$$

where *n* and *k* are user-defined parameters.

It must be mentioned that the *k* parameter controls the progressive weight that is placed on differences on individual dimensions while the *n* parameter controls the progressive weight that is placed on larger differences between objects. If *k* and *n* are equal to 2, then this distance is equal to the Euclidean distance.

In our case, we have used all three methods to classify the investigated samples by the means of numerical values corresponding to the low magnetic field (m_I = 5/2) allowed transition of Mn^{2+} resonance lines. This kind of analysis was possible without introducing significant errors because of all EPR spectra have been recorded in the same experimental conditions (excepting the spectrometer gain, but this one does not influence the shape of resonance line).

The numerical values of both Euclidian and power distances as well as the correlation coefficients have been further used derive three tree diagrams that allowed establishing, in a quantitative manner, similarities and differences between all 12 samples (Fig. 2).

One main characteristics, common to all diagrams, consist of the fact that irrespective of the selection criterion, all samples are divided into two main clusters, one containing only dolomitic marbles and other one consisting of calcitic and calcito-dolomitic specimens. This peculiarity reflects in fact the great difference between the EPR spactra of Mn^{2+} in calcite and dolomite. The fact that the calcito-dolomitic samples are classified, in all three diagrams, among calcitic samples can be explained by the low amount of dolomite present in these samples, and consequently to a more resemblance of the EPR spectra to calcitic than to dolomitic type.

Also it is interesting to mention that between Euclidean and power distance tree diagrams, the differences consists more in the linkage distance, and less in the distribution of sample within calcitic cluster. At the same time, within this cluster, Kerkira and Nauplio, both limestones, form a subcluster, while in Perason's tree diagram, all limestone samples, *i.e.* Kerkira, Nauplio and Dyonisos are linked together.

It seems in this way, that the correlation coefficient tree diagrams are more sensitive to the difference marble-limestone than the distances ones.

Looking at the linkage distance, which quantifies de degree of similarity, it is obvious that the correlation coefficient diagrams are characterized by longer linkage distances than de the other ones that signifies the difference between calcitic type and dolomitic type Mn^{2+} EPR spectra are better evidenced on the first category of diagrams. At the same time, within each main cluster, Euclidean distances or even better the power distances seems to be more adequate to be used as a discriminating factor between different spectra.

These considerations concerning the use of numeric taxonomy have showed that the cluster analysis represent a useful and, for the time being insufficiently used tools for provenance study.

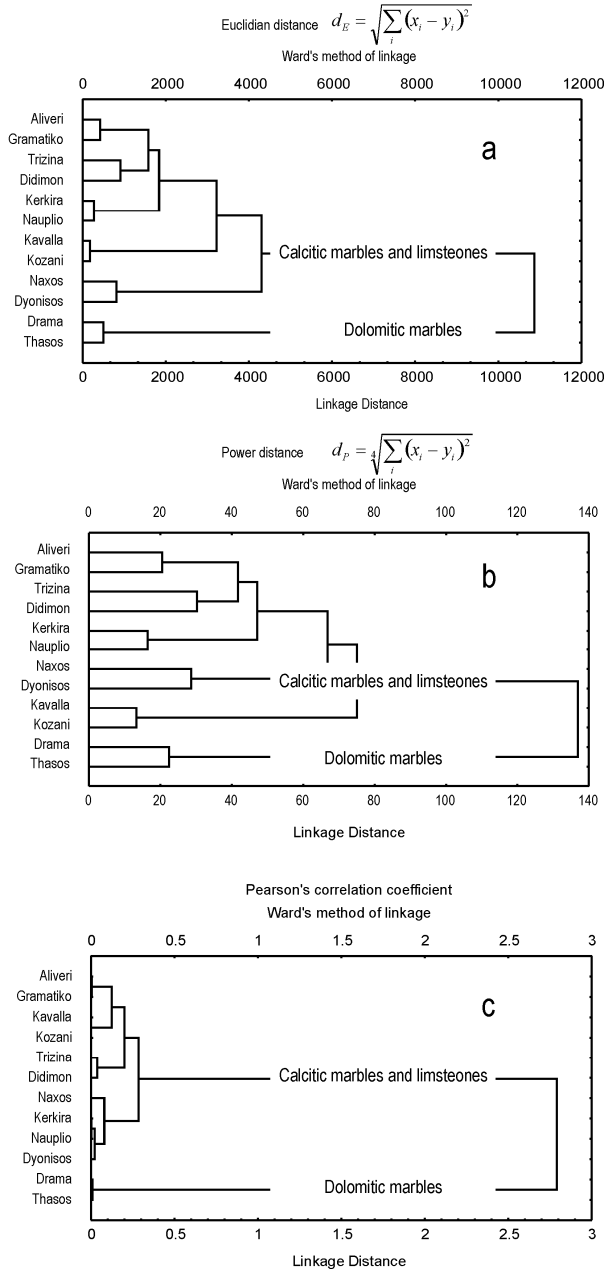

Fig. 2. - Tree diagrams of the investigated samples based on the Euclidian distance (a), generalized Euclidian distance (b) and correlation (c) between the low field Mn^{2+} EPR lines. In spite of some discrepancies, all diagrams reflect predominantly the mineralogical composition of considered specimens. It must be pointed out that the best discrimination between main clusters is provided by the Pearson's correlation coefficient.

4. Concluding Remarks

By applying the methods of cluster analysis and numeric taxonomy to the analysis of the EPR spectra of Mn^{2+} ions in marble and limestone samples collected from 12 Greek historical quarries, it was possible to classify all samples in concordance with their mineralogical structure. At the same time, it has been shown that the Perason's correlation coefficient is most suitable to discriminate samples having different mineralogical composition while Euclidean and power distances showed to be more adequate in differentiating samples belonging to the same petrologic group.

REFERENCES

1. M. Waelkens, P. de Paepe, L. Moens, L. Quarries and the marble trade in antiquity. In Classical Marble: Geochemistry, Technology, Trade NATO ASI E: Applied Sciences-153, Herz, N., Waelkens, M. Eds. Kluwer Academic: Dordrecht, (1988).
2. G. Ed. Borghini, Marmi Antichi. Edizioni De Luca, Roma, 1983, (in Italian).
3. O.G. Duliu, L.C. Dinescu, D. Skliros, J. Trace Microprob. Tech. 17, 165, (1999).
4. K.J. Matthews, Archaeometry, 39, 321, (1997)
5. A.P Grimanis, M. Vassilaki-Grimani, Provenance Studies of Greek Marbles by Instrumental Neutron Activation Analysis. In Classical Marble: Geochemistry, Technology, Trade NATO ASI E: Applied Sciences-153, Herz, N., Waelkens, M. Eds. Kluwer Academic: Dordrecht, (1988).
6. N. Hertz,. Archaeometry, 29, 35, (1987).
7. V. Baïetto, G. Villeneuve, P. Guilbert, M. Schvoerer, Appl. Rad. Isot. 52, 229, (2000).
8. D. Cordischi, D. Monna, A.L. Segre, Archaeometry, 23, 68, (1983).
9. R.V. Lloyd, P.W. Smith, H. Haskell, Archaeometry, 27, 108, (1985).
10. G. Armiento, D. Attanasio, R.Platania, Archaeometry, 39, 309, (1997).
11. V. Baïetto, G. Villeneuve, M. Schvoerer, F.Bechtel, Archaeometry, 41, 253, (1999).
12. D. Attanasio, G. Armiento, M. Brilli, M.C Emanuele, R. Platania, B Turi, Archaeometry, 42, 3, (2000).
13. D. Attanasio, R. Platania, J. Mag. Res. 144, 322, (2001).
14. V.A. Mandi, Determination of the provenance of marble used in ancient monuments with the techniques of electron paramagnetic resonance and neutron activation analysis. Ph.D. Thesis. University of Athena, Athena, (1993), (in Greek with abstract in English).
15. Maniatis, Y. Mandi, V. Electron Paramagnetic Resonance Signals and Effects in Marbles Induced by Working. J. Appl. Phys. 1992, 71, 4859-4867.
16. V. Mandi, Y. Maniatis, Y. Bassiakos, V. Kilikoglu, Provenance Investigation of Marbles with ESR Spectroscopy: Further Developments. In Ancient Stones: Quarring, Trade and Provenance Acta Archaeologica Lovaniensia, Monograpiae 4, Waelkens, M., Herz, N., L. Moens Eds. Leuven Universiyty , (1992).
17. K. Polikreti, Y. Maniatis, Archaeometry, 44, 1, (2002).

18. C. Punyadeera, A.E. Pillay, L. Jacobson, G. Whitelaw, J. Trace Microprob. Tech. 17, 63 (1999).
19. A. Von Bohlen, J. Trace Microprob. Tech., 17, 177, (1999).
20. E.H. Bakraji, I. Othman, A. Sarhil, N. Al-Somel, J. Trace Microprob. Tech. 20, 57, (2002).
21. A Abragam, B. Bleany, Electron Paramagnetic Resonance of Transition Ions. Clarendon Press, Oxford, (1970).
22. M. Ikeya, New Applications of Electron Spin Resonance, Dating, Dosimetry and Microscopy. Word Scientific Publishing Co., Singapore, (1993).
23. J.A. Weil, J.R. Bolton, J.E. Wertz, Electron Paramagnetic Resonance – Elementary Theory and Practical Applications. J. Wiley & Sons, New York. (1994).
24. J. Aubouin, J.H.Brunn, R. Celet, J. Dercourt, J. Godfriaux, J. Mercier, O. Kokek, M. Walter, Geo-tectonic Map of Greece, p. 48, Greek Geological Survey, Athens, (1985).
25. C. Kikuchi, L.M. Matarrese, J. Chem. Phys. 33, 601, (1960).
26. R.A. Shepherd, W.R.M. Graham, J. Chem. Phys. 81, 6080, (1984).
27. D.G. Quirk, J.B. Raynor, Chem. Geol. 95, 299, (1992).

STUDIA UNIVERSITATIS BABEŞ-BOLYAI, PHYSICA, XLIX, 1, 2004

SOME CONSIDERATIONS CONCERNING THE RELAXATION OF THE RADIATION FREE RADICALS IN POLYMERS

M. VELTER-STEFANESCU[a], O.G. DULIU[b], N. PREDA[a], I. URSU[b]

[a]National Institute of Materials Physics, Magurele, P.O. Box MG-7, RO-077125 Bucharest, Romania
[b]University of Bucharest, Department of Atomic and Nuclear Physics, Magurele, P.O. Box MG-11, RO-077125 Bucharest, Romania

ABSTRACT. Relaxation measurements performed below 77 K in X and Q bands on electrons irradiated polymers (polyethylene, polycarbonate and polymethylmethacrylate) show that the spin-lattice relaxation time of radiation free radicals varies inverse proportionally with the square of absolute temperature and free radicals concentration but does not depend on the magnetic field. All these characteristics has been explained by taking into account that below 77 K there is a considerable amount of stable radical-pairs that mediate the relaxation process of single radicals. Accordingly, within this hypothesis, an analytical equation that quantitatively describes all these particularities has been deduced.

Key words: EPR, spin-lattice relaxation, free radicals, polymers, irradiation

1. Introduction

Polymers represent a class of natural or synthetic long-chain molecules, or macromolecules, composed by the addition of great number simple chemical units: monomers. Natural organic polymers for instance proteins, cellulose, nucleic acids or inorganic ones such as quartz, feldspar or diamond together with man-mad materials as glass, paper, plastic or rubber play a tremendous role in nature and human life.

For this reason, the investigation of polymers molecules together with the synthesis of new ones is continuously developing.

Among the methods currently used to investigate the polymers structure, Electron Paramagnetic Resonance (EPR), due to its ability to evidence only the paramagnetic free radicals plays a significant role. In polymers, free radicals are generated by breaking the macromolecules into more fragments, as so as the electrons that form chemical bonds are distributed among them. Polymers molecules can be split up by a variety of factors such as mechanical grinding, action of various chemical agents or irradiation with ionizing radiation. Investigation of the free radicals generated in this way is very useful in understanding the polymers aging, macromolecules structure, resistance to irradiation or to other chemical agents.

Predominantly, the free radicals are characterized by a gyromagnetic factor closed to 2, denoting a weak spin-orbit interaction. At the same time, frequently, the EPR spectra of free radials present well resolved hyperfine or superhyperfine structures that reflect their chemical structure.

EPR investigation can be performed by using continuous wave or pulse techniques. In the last case, it is possible to investigate in a more direct manner the spin-lattice, as well as, spin-spin interactions, which could provide significant information concerning polymers lattice.

In an older paper, Bowman and Kevan [1] have shown that the low temperatures spin-lattice relaxation of the free radicals formed by irradiation in ethanol glasses consists of the modulation of the Electron Nuclear Dipolar (END) interaction with the units (free radicals), which tunnelate between the minima of a double-well asymmetrical potential. Within this mechanism, considered to be dominant in the glassy material, the spin-lattice relaxation time T_1 obeys, for a wide temperature range, to the law:

$$T_1^{-1} \sim B^{-2}T \tag{1}$$

where *B* represents the magnetic field, while *T* stands for the absolute temperature.

Due to their chemical structure, polymers, even the highly ordered ones, are not "*stricto senso*" crystalline solids, but have some characteristics close to glassy state [2]. Consequently, in order to check the validity of this mechanism we have investigated the spin-lattice processes in three different types of high amorphous polymers, i.e. high pressure polyethylene (PE), polycarbonate (PC) and poly(methylmethacrylate) (PMMA).

2. Materials and Methods

The investigated samples were irradiated at 77 K with 3 MeV and 10 MeV electrons, at various integral doses ranging between 30 kGy and 3 MGy, respectively. The irradiations have been performed by using the Linear Accelerator Irradiation Facilities of the Institute of Atomic Physics, Bucharest. At the same integral doses, no significant differences in the ESR spectra of the samples irradiated with 3 MeV and 10 MeV electrons were noticed. The relaxation measurements were carried-out in the Q and X bands, in the temperature ranges: 1.2-4.2 K and respectively, 2-12 K, using an original pulsed-saturation method [3]. This method consists of a long microwave pulse that saturate the spins, followed by a train of short equidistant microwave pulses, which monitor the recovery of the magnetization towards the thermal equilibrium value.

It must be pointed out that, for all samples, the relaxation curves have shown the presence of a cross-relaxation process (biexponential curves). Consequently, in order to avoid the complications introduced by the cross-relaxation between the singular radicals and the pairs, the calculations of T_1 from the recovery curves were done only when the spin systems were close to thermal equilibrium.

The concentration of free radicals has been determined from 77 K EPR spectra by using an organic carbon reference sample containing 1.6 10^{16} centres cm^{-3}.

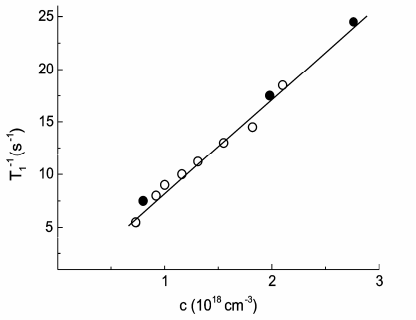

Fig. 1. Dependence of the electrons spin-lattice relaxation rate by respect to free radicals concentration for irradiated PMMA samples. Hollow symbol - X band; solid symbol - Q band. Similar dependencies have been noted for the other two irradiated polymers.

3. Results and Discussion

By analyzing both concentration and temperature dependences of the free radicals spin-lattice relaxation time T_1 in all three polymers, we have noticed the following peculiarities:

i in the region where the free radical concentration increases as irradiation time is increased, the experimental data exhibit a linear dependence of the relaxation rate on the radical concentration: $T_1^{-1} \sim c$ (Figure 1). As for each kind of polymers the experimental points corresponding both to X and Q bands are disposed on the same line, it results that T_1 is magnetic-field independent.

ii the temperature dependence of the inverse of the relaxation time T_1^{-1} is well described by a power type low: $T_1^{-1} \sim T^{2\pm0.2}$ (Figure 2).

At the same time, it is worth to mention that the free radicals formed in all investigated polymers differ by the number of CH_3 groups. In PMMA all free radicals contain CH_3 groups while in PE and PC their number is very low. The CH_3 groups exhibit rotational motion by tunneling even at liquid helium temperature [4], which can modulate the END-interaction (or another interaction) generating relaxation transition [5]. Considering such a mechanism as dominant, the relaxation rates of the three types of polymers under study would be very different, obeying to a law described by eq. (1). In contrast, our experimental results exhibit an entire different behavior, better expressed by the equation:

$$T_1^{-1} \sim c\, B^0\, T^{2\pm0.2} \tag{2}$$

By supposing that the spin-lattice relaxation process can take part also via paired radicals found on the triplet state, it results that between the single radicals relaxation time T_1 and the radical pairs relaxation time T_{1p} there is the following relation:

$$T_1^{-1} \sim \frac{c_p}{c} T_{1p}^{-1} \tag{3}$$

where c and c_p represent the concentration of single and, respectively, paired radicals.

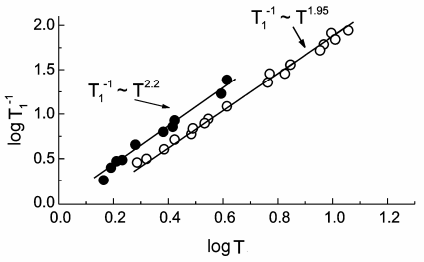

Fig. 2. Temperature dependence of T_1 spin-lattice relaxation time for irradiated PMMA. Hollow symbol - X band; solid symbol - Q band. Analogous behavior has been observed for the other two irradiated polymers.

This assertion is sustained by the existence of a significant cross-relaxation process between single and paired radicals, as it results from the significant overlapping of the EPR resonance lines of both categories of radicals (Fig. 3).

At the same time, the relaxation of the paired radicals is determined, most probable, by an “inverse” Orbach process. By taking into account the fact that the structure of the polymer macromolecules is linear, and thus, by considering a one-dimension lattice, it follows that:

$$T_{1p}^{-1} \sim J\left(exp\frac{J}{kT}-1\right)^{-1} \tag{4}$$

where J stands for the exchange integral.

The exchange integral J covers a wide range of values, as the inter-radical distance is not precisely defined ($r_{ij} \cong 5 \div 10$Å). In this way, for a uniform distribution of J-the exchange interaction within a pair, the relaxation rate of the paired radicals becomes:

$$T_{1p}^{-1} \sim \int_0^{k\theta} J\left(exp\frac{J}{kT}-1\right)^{-1} P(J)dJ \approx B^0T^2 \tag{5}$$

where: θ represents the Debye temperature; the B^0 factor was introduced to emphasize that the Orbach-Aminov process is magnetic-field independent.

As the pairs are formed by the random overlapping single radicals, it follows that between pair-radicals concentration c_p and single radicals concentration c there is the relation:

$$c_P \sim c^2 \tag{6}$$

Finally, by combining equations (2-6) it results:

$$T_1^{-1} \sim cB^0T^2 \tag{7}$$

in excellent agreement with the experimental data.

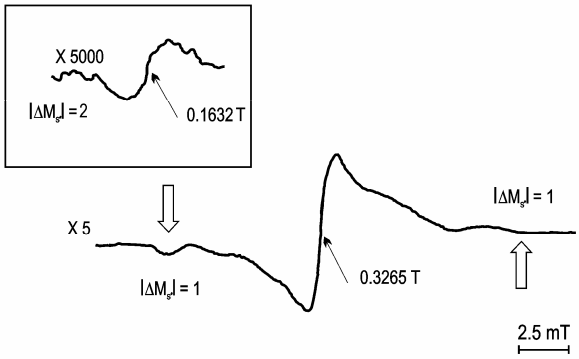

Fig. 3. The experimental EPR spectra of electron irradiated PMMA. The central line is due to single radicals while the lateral ones are due to radical pairs. The inset shows the low field ($\Delta M_{S'} = 2$) EPR line of radical pairs. All measurements were performed at 77 K in X band (9.209 GHz) for 10 mW microwave power. Free radicals concentration was of 1.3 10^{18} centers cm^{-3}. Similar spectra have been observed for the other irradiated polymer.

4. Concluding Remarks

Relaxation measurements performed both in X and Q bands on electrons irradiated polyethylene, polycarbonate and polymethylmethacrylate have shown that the spin-lattice relaxation time of these radicals varies inverse proportionally with the square of absolute temperature and free radicals concentration but does not depend on the magnetic field. All these characteristics could be very well explained by taking into account that below 77 K there is a considerable amount of stable radical-pairs that mediate the relaxation process of single radicals. Accordingly, an analytical equation that quantitatively describes all these particularities has been deduced by following this model.

REFERENCES

1. M. K. Bowman and L. Kevan, J. Chem. Phys. 81, 456 (1977)
2. W. A. Phillips (ed) “Amorphous Solids-Low temperature Properties, Springer-Verlag, Berlin (1981)
3. M. Velter-Stefanescu, B. Ianculovici, Rev. Roum. Phys. 19, 431, (1974)
4. R. Grosescu, Proc. 16th Congress AMPERE, ed. I. Ursu, Bucharest, (1970), pg. 561
5. M. K. Bowman and L. Kevan, in “ Time Domain Electron Spin Resonance” ed L Kevan and R. N. Schwartz, John Wiley and Sons(1979), pg. 67.

STUDIA UNIVERSITATIS BABEŞ-BOLYAI, PHYSICA, XLVIII, 1, 2004

STUDY BY MAGNETICALLY MODULATED MICROWAVE ABSORPTION OF $Bi_{1.7}Pb_{0.4}Sr_{1.5}Ca_{2.5}Cu_{3.6}O_x/(LiF)_y$ SUPERCONDUCTING SYSTEM

M. VELTER-STEFANESCU[a], O.G. DULIU[b], V. MIHALACHE[a], I. URSU[b]

[a]National Institute of Materials Physics, Magurele, P.O. Box MG-7, RO-077125 Bucharest, Romania
[b]University of Bucharest, Department of Atomic and Nuclear Physics, Magurele, P.O. Box MG-11, RO-077125 Bucharest, Romania

ABSTRACT. High temperature superconducting system $Bi_{1.7}Pb_{0.4}Sr_{1.5}Ca_{2.5}Cu_{3.6}O_x/(LiF)_y$ was investigated by magnetically modulated microwave absorption (MAMMA), evidencing the effect of LiF content on 2223 phase critical state. The experimental results show a significant growth (about three time) of the 2223 superconducting phase content and a slightly increase (around 2 %) of the critical temperature for y ~ 0.07. Moreover, for y between 0.05 and 0.12, we have noticed that the ratio $\_\frac{\Delta T_c^{mw}}{\Delta B}$ is practically constant and equal to (18.5 ± 1.5) KT^{-1}, typical value for 2223 superconducting phase.

Key words: Magnetically modulated microwave absorption, High temperature superconductivity, Critical state, Critical current density

1. Introduction

One of the most significant parameters for potential applications of the high-temperature superconductor (HTS) is the critical current. As it is well known, above 77 K the flux - pinning effect is weak. From this reason, the engineering of pinning centers, which includes and the doping with various atoms, is of great importance, leading to the increase of the critical current density J_c. By Li substitution, or the LiF addition in $Bi_2Sr_2CaCu_2O_{8+\delta}$ (denoted by Bi-2212) superconducting system, the critical current density was enhanced, respectively, has led to the increasing of the Bi-2212 superconducting phase content [1,2]. The Li doping of bulk $Bi_2Sr_2Ca_2Cu_3O_{10+\delta}$ (denoted by Bi-2223) ceramics and tapes has enhanced the critical current density, too [3,4]. In the case of the (Bi,Pb)-Sr-Ca-Cu-O (BiPSCCO), the F-doping results in the enhancement of the flux pinning effect and the remarkable improving of the superconducting properties of the Bi-2223 phase [5].

Recently, batches of $Bi_{1.7}Pb_{0.4}Sr_{1.5}Ca_{2.5}Cu_{3.6}O_x/(LiF)_y$ superconducting system (*y* varying between 0.02 and 0.3) were prepared by using the standard solid state reaction method, and were investigated by resistive, AC complex susceptibility and DC magnetization measurements [6,7].

Due to the fact that the synthesis procedure led to critical temperatures of the B_i-2212 phase lower then 77 K [7], it is obvious there is no response from this phase.

In this paper we present the results of the critical state study by an alternative method, Magnetically Modulated Microwave Absorption (MAMMA) [8,9] carried out on a such batch of $Bi_{1.7}Pb_{0.4}Sr_{1.5}Ca_{2.5}Cu_{3.6}O_x/(LiF)_y$ system, with *y* between 0.02 and 0.15. The application of this method is of primary importance because whereas resistance measurements record the onset of the first superconducting path in the sample, microwave absorption technique provides a measure of the sample state, in the sense that all regions of the sample contribute to the observed response. As a result, the T_c determined by resistance measurement can be higher than the average critical temperature defined as the MAMMA peak position (T_c^{mw}), which characterizes all sample.

Furthermore, the features attributed to the Josephson Junctions (JJs) formed at interfaces between superconducting grains and clusters are observed T_c^{mw} as a rising baseline.

2. Materials and Methods

Samples with nominal $Bi_{1.7}Pb_{0.4}Sr_{1.5}Ca_{2.5}Cu_{3.6}O_x/(LiF)_y$ composition have been prepared from high-purity Bi_2O_3, PbO, $SrCO_3$, $CaCO_3$ and CuO powders, carefully ground in an agate mortar and calcinated in air for 20 h in an alumina crucible at 800 – 820 ^oC.

Small quantities of final calcinated compound were ground again, sieved through a 40 μm mesh and thoroughly mixed with various amount of LiF and pressed in 3 x 3 x 10 mm^3 pellets at 0.75 GPa. The resulting pellets were sintered in air at 832 ± 2 ^oC for 320 h. SEM images have showed that all investigated samples consisted of small grains of about 30 x 30 x 0.5 μm [6].

The MAMMA investigations were carried out in the X-band (9 GHz) at an incident microwave power of 3 mW. MAMMA responses were registered in 3, 6, 12, 25, 50 and 100 mT DC magnetic fields, superimposed over a 0.1 mT AC magnetic field (100 kHz) by slowly increasing the sample temperature (~ 1 K min^{-1}) from 77 K up to 110 K. The sample temperatures were measured with a precision of ± 0.2 K, and all other experimental errors were about ± 5 %.

Selected sub-samples (~ 30 mg), cut from the initial pellets, were placed in the center of a TE_{011} resonant cavity, *i.e.* in the maximum of the microwave magnetic component.

Both DC and AC magnetic fields were in the horizontal plane and perpendicular to the microwave one. As the microwave electric field vanishes at the sample, the primary source of losses is due to the eddy currents induced by the microwave magnetic field.

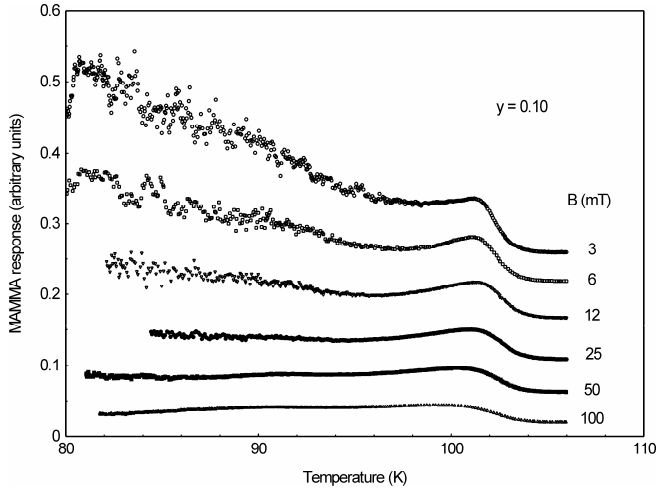

Fig.1 – MAMMA responses in different DC magnetic fields of the $Bi_{1.7}Pb_{0.4}Sr_{1.5}Ca_{2.5}Cu_{3.6}O_x/ (LiF)_y$ for y =0.1.

3. Results and Discussion

The MAMMA responses, corresponding to different DC magnetic field, for the y =0.1 sample are shown in Fig. 1. All intensities are reported for the same amplification and sample weight. As it can be seen from this figure, the baseline below T_c^{mw} monotonously goes down by increasing the DC magnetic field, signifying the decoupling of the superconducting grains. For 100 mT magnetic field, all grains are decoupled; this thing being testified by a total absence of the noise-like signal. At the same time, the positions of MAMMA peak are slowly shifted towards lower temperatures. All the other samples presented resembling responses.

The experimental MAMMA parameters: average critical temperature T_c^{mw}, MAMMA peak amplitude I_{max}, as well as $-\frac{\Delta T_c^{mw}}{\Delta B}$ ratio for the all investigated samples are reproduced in Table 1.

Based on the analysis of these data, we can make the following remarks:

i.- The amplitudes of MAMMA peaks for all investigated samples depend on the DC magnetic field in a similar manner (Fig. 2). The observed peculiarity is sustained by the existence of a significant positive correlation ($r > 0.96$, $p < 0.005$) between the numerical amplitude values versus magnetic field corresponding to each sample (Table 2).

We interpret this result as a structural identity of the 2223 superconducting phase in all samples.

At the same time, the amount of this phase reaches a maximum at a LiF concentration around 7 at. %.

ii. – By increasing the LiF concentration, the critical temperature increases, reaching a maxim for *y* around 0.07, too. This growth is more significant for low DC magnetic fields.

Table 1

Experimental values of the MAMMA parameters of investigated samples

	Sample											
	y = 0.02		y = 0.05		y = 0.07		y=0.10		y=0.12		y=0.15	
B (mT)	T_c^{mw} (K)	*I* (a.u.)	T_c^{mw} (K)	*I* (a.u.)	T_c^{mw} (K)	*I* (a.u.)	T_c^{mw} (K)	*I* (a.u.)	T_c^{mw} (K)	*I* (a.u.)	T_c^{mw} (K)	*I* (a.u.)
3	--	6.05	100.6	5.37	101.6	11.22	101.2	7.70	100.6	4.34	99.5	1.29
6	99.7	5.79	100.4	4.91	101.4	9.27	101.1	6.17	100.6	3.48	99.5	1.00
12	99.6	4.55	100.3	3.86	101.2	7.41	101.1	5.00	100.4	2.82	99.5	0.86
25	99.6	3.58	99.9	3.13	101.2	5.61	100.9	4.08	100.1	2.30	99.4	0.73
50	99.2	3.01	99.6	2.48	100.6	4.39	100.3	3.33	99.7	1.88	99.0	0.59
100	99.2	2.18	98.7	1.78	99.8	3.02	99.3	2.48	99.0	1.40	99.1	0.47
$-\frac{\Delta T_c^{mw}}{\Delta B}$	-		18.5 ± 1.5 (K T^{-1})								-	

a.u. stands for arbitrary units

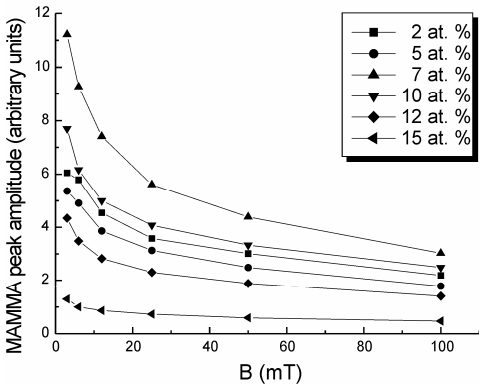

Fig. 2 – MAMMA peak amplitude vs. DC magnetic field for all investigated samples.

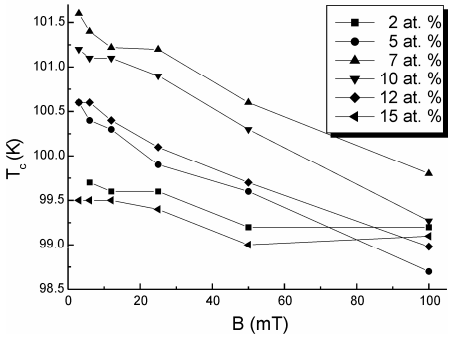

Fig. 3 – Critical temperatures of the all investigated samples vs. DC magnetic field

Table 2

Matrix of the correlation coefficients of the MAMMA peak amplitude versus magnetic field for all investigated samples. All correlations are significant for p <0.005

2 %	2%					
5 %	0.9980	5%				
7 %	0.9885	0.9946	7%			
10 %	0.9777	0.9872	0.9978	10%		
12 %	0.9778	0.9872	0.9978	1	12%	
15 %	0.9639	0.9771	0.9927	0.9977	0.99768	15%

4. Concluding Remarks

High temperature superconducting system $Bi_{1.7}Pb_{0.4}Sr_{1.5}Ca_{2.5}Cu_{3.6}O_x/ (LiF)_y$ was investigated by magnetically modulated microwave absorption (MAMMA), evidencing the effect of LiF content on 2223 phase critical state. The experimental results show a significant growth (about three time) of the 2223 superconducting phase content and a slightly increase (around 2 %) of the critical temperature for y ~ 0.07. Moreover, for y between 0.05 and 0.12, we have noticed that the ratio $-\frac{\Delta T_c^{mw}}{\Delta B}$ is practically constant and equal to (18.5 ± 1.5) KT^{-1}, typical value for 2223 superconducting phase.

Acknowledgment. This work was supported by the Ministry of Education and Research, Romania, under CERES program. One of authors (V-S. M.) wishes to express his thanks to Dr. G.V. Aldica for useful discussion.

REFERENCES

1. I. Matsubara, H. Tanigawa, T. Ogura, H. Yamashita, M. Kinoshita, T. Kawai, Physica C, 167, 503, (1990).
2. E.D. Politova, I.V. Ol'chovik, G.M. Kaleva, Yu.N. Venevtsev, Ferroelectrics, 167, 305, (1995).
3. S. Kambe, Y.G. Gou, S.X. Dou, H.K. Liu, Y. Wakahara, H. Maeda, K. Kakimoto, M. Yavuz, Supercond. Sci. Technol. 11, 1061, (1998).
4. S. Kambe, Y.G. Gou, S.X. Dou, H.K. Liu, Y. Wakahara, Proc. IPMM'97, Watson ferguson & Co, Braisbane 2, 1445, (1996).
5. X.-H. Gao, X.-G. Wang, S.-F. Jang, J. Li, S. Gao, G.-D. Zheng, Phys. Rev. B 50, 1237, (1994).
6. V. Mihalache, G. Aldica, C. Giusca, L. Miu, J. Supercond.: Incorporating Novel Magn. 14, 575, (2001).
7. V. Mihalache, G. Aldica, S. Popa, A. Crisan, Physica C, 384, 451, (2003).
8. K Moorjani, J.Boahandy, F.J.Adrian, B.F.Kim, Phys. Rev. B 36, 4036, (1987).
9. D. Shaltiel, H. Bill, A. Grayevsky, A. Junod, D. Lovy, W. Sadowski, E.Walker, Phys. Rev. 43, 13594, (1991).